Università degli Studi di Palermo

AREA QUALITÀ, PROGRAMMAZIONE E SUPPORTO STRATEGICO
SETTORE STRATEGIA PER LA RICERCA
U. O. DOTTORATI

Dottorato Scienze Fisiche e Chimiche

Dipartimento di Fisica e Chimica-Emilio Segrè

FIS/03-FIS/07

Common mechanisms underlying membrane modifications induced by protein interactions

IL DOTTORE

Sara Anselmo

IL COORDINATORE

Giuseppe Lazzara

IL TUTOR

Gioacchino Massimo Palma

CO TUTOR

Valeria Vetri

CICLO XXXIV

ANNO CONSEGUIMENTO TITOLO 2022

Preface

The PhD thesis entitled *Common mechanisms underlying membrane modifications induced by protein interactions* was submitted to the Department of Physics and Chemistry-Emilio Segrè at the University of Palermo to obtain the PhD degree in Physics and Chemistry. The project was carried out in the Molecular Biophysics Laboratory, Department of Physic and Chemistry-Emilio Segrè at the University of Palermo, under the supervision of the Associate Professor Valeria Vetri.

This thesis contains the following research papers:

S. Anselmo, G. Sancataldo, H. Mørck Nielsen, V. Foderà, and V. Vetri "**Peptide–Membrane Interactions Monitored by Fluorescence Lifetime Imaging: A Study Case of Transportan 10**" *Langmuir* (**2021**) 37, 44, 13148–13159 https://doi.org/10.1021/acs.langmuir.1c02392

S. Anselmo, G. Sancataldo, V. Foderà and V. Vetri "**α-casein micelles-membranes interaction: flower-like lipid protein coaggregates formation**" *Biochimica and Biophysica ACTA-General subjects* (**2022**) 1866,10,130196 https://doi.org/10.1016/j.bbagen.2022.130196

S. Anselmo, G. Sancataldo, and V. Vetri "**Trasportan 10 induced perturbation and pores formation in Giant Plasma Membrane Vesicles**"- In preparation

The following research papers are additional outcomes that were not included in the PhD thesis but which were extremely helpful for a deeper understanding of the experimental approaches and techniques reported in the thesis.

G. Sancataldo, S. Anselmo and V. Vetri "**Phasor-FLIM analysis of Thioflavin T self-quenching in Concanavalin amyloid fibrils**", *Microscopy Research Technique* (**2020**) 83, 7, 811-816 https://doi.org/10.1002/jemt.23472

S. Savoca, K. Matanović ,G. D'Angelo, V. Vetri, S. Anselmo, T. Bottari, M. Mancuso, S. Kužir, N. Spanò, G. Capillo , D. Di Paola , D. Valić and E. Gjurčević "**Ingestion of plastic and non-plastic microfibers by**

farmed gilthead sea bream (Sparus aurata) and common carp (Cyprinus carpio) at different life stages" *Science of The Total Environment* (**2021**) 782,146851
https://doi.org/10.1016/j.scitotenv.2021.146851

P. Picone, F.S. Palumbo, S. Federico, G. Pitarresi, G. Adamo, A. Bongiovanni, A. Chaves, P. Cancemi, V. Muccilli, V. Gibli, V. Vetri, S. Anselmo, G. Sancataldo, V. Di Liberto and D. Nuzzo "**Nano-structured myelin: new nanovesicles for targeted delivery to white matter and microglia, from brain-to-brain**" *Materials today bio* (**2021**) 12, 100146 https://doi.org/10.1016/j.mtbio.2021.100146

S. Anselmo, S. Cataldo, T. Avola, G. Sancataldo, M.C. D'Oca, T. Fiore, N. Muratore, M. Scopelliti, A. Pettignano and V. Vetri, "**Lead (II) Ions adsorption onto Amyloid particulates: an in depth study**" *Journal of colloids and interface science* (**2021**) 610, 347-358
https://doi.org/10.1016/j.jcis.2021.11.184

S. Anselmo, G. De Luca, V. Ferrara, B. Pignataro G. Sancataldo and V. Vetri "**Insight into mechanisms of creatinine optical sensing using fluorescein-gold complex**" *Methods and Applications in Fluorescence* (2022) 10(4) https://pubmed.ncbi.nlm.nih.gov/35901805/

S. Anselmo, T. Avola, V. Foderà, K. Kalouta, A.Pettignano, G. Sancataldo and V. Vetri, "**Efficient removal of Lead (II) from water using Soy Protein Micronsponges**" – in preparation

Acknowledgements

My first and foremost thanks goes to my supervisor Prof. Massimo Palma and my co-supervisor Prof. Valeria Vetri for giving me the unique opportunity to carry out this project under their admirable and fundamental guidance. Prof. Valeria Vetri, with her great scientific background and extreme humanity, welcomed me in her laboratory and she has always supported, taught and encouraged me to do my best during these years, made also more difficult by pandemic. She gave me the great chance to discover the "biophysics world", that I thought was so far from my background in pharmaceutical chemistry, but instead perfectly fits, opening new horizons and making me discover new passions. For this reason, she deserves all my gratitude.

My next thanks goes to Prof. Cristina D'oca who made me discover this reality and encouraged me to take this path and to Prof. Maurizio Leone who has always been available to assist and teach me. Additionally, I would like to thank Prof. Vito Foderà who allowed me the fruitful collaboration with the Department of Pharmacy at the University of Copenhagen, also providing me with some of the resources necessary to carry out the research. Special thanks also goes to Prof. Giuseppe Pizzolanti and Dr. Concetta Baiamonte who offered their essential biological knowledge and tools for the development of my project. Also thanks to Prof. Alberto Pettignano and Dr. Salvatore Cataldo for the pleasant and fruitful collaboration. I am very grateful to all of them also for the friendly and positive approach towards me.

Thanks to all the members of the Biophysics Group, Dr. Giuseppe Sancataldo, Dr. Vittorio Ferrara, Dr. Giuseppe De Luca, Dr. Kleopatra Kalouta, Dr. Giorgia Puleo and Dr. Daniele Gulli for their collaboration, for the useful discussions and for the carefree moments we shared during the laboratory activities. We have managed to create a wonderful and harmonious environment; they are certainly more friends than colleagues.

Additionally, I would like to thank my brave mum for her daily and continuous support. She sustains me with love in all possible ways, always being confident in my capabilities and positive about my future prospects, giving me the just and necessary serenity. I would also like to thank my brothers, my family and friends who encouraged me over the years.

Finally, a special thanks goes to my guardian angel, my dad, who always believed in me and that I always feel close to me during the important choices of my life. I am sure he would be proud of the progress I have made so far.

Abbreviations

α-Syn	α-synuclein
AMP	Antimicrobial peptides
ANS	1-anilinonaphthalene-8-sulfonate
Arg	Arginine
CD	Circular dichroism
CF	Carboxyfluorescein
Chol	Cholesterol
CMC	Critical micelle concentration
CPP	Cell penetrating peptide
D	Diffusion coefficient
FLIM	Fluorescence lifetime imaging microscopy
GP	Generalized Polarization
GPMVs	Giant plasma membrane vesicles
GVs	Giant vesicles
H-c	Heated casein
Lys	Lysin
MAV	Moving Average
N-c	Native casein
NR	Nile Red
POPC	2-Oleoyl-1-palmitoyl-sn-glycero-3 phosphocholine
POPG	2-Oleoyl-1-palmitoyl-sn-glycero-3-phospho-rac-(1-glycerol) sodium salt
RICS	Raster image correlation spectroscopy
TP10	Transportan 10
Trp	Tryptophan

Abstract

Peptide–membrane interactions are implicated in a broad range of biological processes such as protein trafficking, cellular signalling, and ion channel formation, which are fundamental for the development of cellular functions but they are also involved in pathogenic events. Such interactions are highly dynamic and spatially heterogeneous and involve multiple complex mechanisms, which are strongly dependent on both the membrane lipid composition and structural details of the bioactive peptide chains, and may furthermore change depending on environmental conditions. All this makes the investigation of the phenomena associated with them highly complex.

This PhD thesis focuses on the use of suitable model systems to analyse complex events involved in such peptide-membrane interaction. This allowing systematic studies as membrane composition can be easily tailored, adding complexity to the system one step at the time, e.g., by adding different lipids and/or protein to the membrane composition. The aim of the work is to highlight the driving forces involved in the protein-membrane interaction (hydrophobic, electrostatic, van der Waals interactions) and induced modifications both in protein structures and lipid bilayer physical state.

The action on model membranes of protein and peptides with highly different features in terms of exposed charges, hydrophobicity, size and structural complexity was analysed by means of classical spectroscopy methods and quantitative microscopy techniques such as Raster Image Correlation Spectroscopy (RICS) and Fluorescence Lifetime Imaging Microscopy (FLIM). Modifications in protein structures and aggregation states were assessed in parallel with membrane modifications.

A new experimental protocol is provided that combines the use of multiple dyes and the phasor approach to analyse fluorescence lifetime imaging microscopy (FLIM) measurements, as a method to highlight membrane modifications in real time and in a non-invasive mode also revealing sub-resolution details on membrane changes at different depths.

Contents

Chapter 1

This chapter provides a brief general introduction on the basics concepts useful to underlie the scientific issues and the experimental choice in this thesis. Protein folding and aggregation in the energy landscape perspective are briefly described, highlighting the dominant interactions involved that are also common to protein-membrane interactions. Useful properties of proteins, membranes and peptides in relation with their function are provided along with the fundamentals of model membranes as relevant tools for revealing "Common mechanisms underlying membrane modifications induced by protein interactions".

1.1. Protein folding, misfolding and aggregation

A living organism is a highly evolved system consisting of a large number of molecular networks. In such networks a key role is played by proteins, large biomolecules that play many critical roles in the body and are required for the structure, function and regulation of the tissues and organs[1]. Proteins are constituted by a precise sequence of amino acids linked together by peptide bonds. Short chains, containing less than 20–30 residues, are commonly called peptides.

Amino acids, the building blocks of the proteins, are small organic molecules that consist of an alpha (central) carbon atom linked to an amino group, a carboxyl group, a hydrogen atom, and a variable component called side chain with different chemical characteristics. Side chains can be non-polar, positive or negative charged and polar but uncharged [2,3]. Their chemistry is critical to protein structure because it can modulate intramolecular specific interactions between single residues of the aminoacidic chains bringing to a functional structure that is at the basis of the correct functionality of the living systems. Such process, referred as folding, has been subjected of a large number of studies since the 70's, and involves molecular interactions as electrostatic, hydrophobic, hydrogen bonding and Van der Waals that induce the protein to assume a certain shape or conformation[4].

Electrostatic interactions may be long range, directionless, columbic interactions, or short range and well oriented (like salt bridges), Van der Waals attractions are weak, short-range interactions among fixed or induced dipoles and hydrogen bonds occur when a hydrogen atom is shared between generally two electronegative atoms [4].

A dominant driving force for protein folding is the hydrophobic effect, which arises from the fact that water molecules seek to form hydrogen bonds with each

other or with other polar molecules, hindering the exposure of hydrophobic surfaces to the solvent [4,5]. To minimize the free energy, the non-polar groups of the protein cluster reducing the number of the "ordered" water molecules surrounding it. Hydrophobic effect is not due to the interactions between side chains of hydrophobic amino acids per se (mainly van der Waals), but rather to the increase in entropy, gained by the removal of hydrophobic surfaces from ordered solvating water [6,7].

To understand how these forces play together to induce a protein to its native three-dimensional structure, typically a "folded conformation", it is necessary to briefly explain the four levels of protein structure: primary, secondary, tertiary, and quaternary [2,3].

The linear sequence of amino acids in a polypeptide chain is considered the primary structure of the protein and can drive the folding of the amino acid chain into certain patterns known as alpha helices and beta sheets kept together by hydrogen bonds. These folding patterns make up the secondary structure of a protein. The spatial relationship of the secondary structures to one another generates the overall three-dimensional structure of a protein, called tertiary structure, stabilized by hydrophobic interactions, but also through salt bridges, hydrogen bonds and disulphide bonds (S-S). The latter occur between the side chains of cysteine by oxidation of two thiol groups (S-H). In addition, there are proteins, that are made up of multiple polypeptide chains, also known as subunits that when they join together give the protein its quaternary structure.

Each protein has its own unique native shape that almost always correspond to the structure that is most thermodynamically stable under physiological conditions.

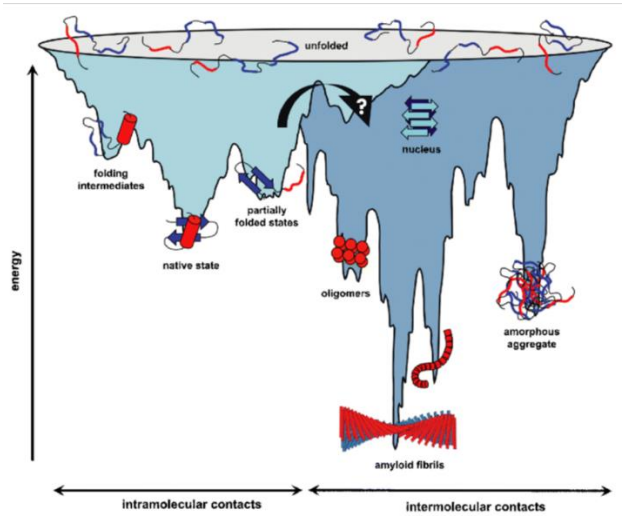

Figure 1.1. A schematic energy landscape for protein folding and aggregation. The surface shows the multitude of conformations 'funneling' towards the native state via intramolecular contact formation, or

towards the formation of amyloid fibrils and amorphous aggregates via intermolecular interactions. Figure and caption are adapted from the original paper[8].

Both protein folding and aggregation involve inter-residue interactions of essentially identical character; for this reason, it is now accepted that they are controlled by general physical principles. The interplay between long- and short-range electrostatic forces, hydrophobic interactions and short-range protein–protein interactions as H-bonding regulates the onset and the evolution of aggregation processes and the nature of the final aggregate structure. The stability, the folding and the aggregation pathway of proteins can be described by using a free energy landscape with multiple minima[8,9] (Fig. 1.1). Each point on the energy landscape describes a specific conformation of the protein characterised by intra and intermolecular contacts[8,10]. The shape of the energy landscape is affected by the contribution of enthalpic terms due to interactions between aminoacids and to both enthalpic and entropic terms due to the interaction with the environment. The minima represent stable states for the protein molecules[8–10].

In specific conditions, it is accepted that a protein chain can spontaneously fold using only the information contained in the primary amino acid sequence; clearly, details of the folding depend on the particular environment in which the process takes place[9,11]. The energy landscape surface allows the protein to fold into native state through any of a large number of pathways and intermediates; the more the funnel surface is smooth, the more the folding process is rapid. Depending on environmental conditions fluctuations in the unfolded or partially folded states may drive the reactions toward native as well as non-native contacts. In these cases when the protein loses its native structure, a population of unfolded or not correctly folded states starts increasing and it is said that the protein is denatured[10]. These states are characterized by a not so packed structure and such open arrangements of the protein molecules enhance the tendency to interact each other forming disordered aggregates often referred as amorphous aggregates, or highly ordered protein aggregates named amyloid fibrils. These are long (in the μm range), narrow (most often 5−10 nm in width), unbranched assemblies typically resulting from intertwined protofilaments, each consisting of a double β-sheet that runs along the fibril axis, where each monomeric unit provides a number of parallel or antiparallel β strands (the “cross-β” structure)[12,13]. Although amyloid fibrils represent the most stable state for a protein[14,15], by changing solution conditions, and so the equilibria between hydrophobic, electrostatic and hydrogen bonding interactions, it is possible to induce structural modifications in protein molecules or in aggregates[16–18]. For example, changes of the pH,

which regulate protein net charge, modify the electrostatic interactions between single proteins and therefore the supramolecular assembly kinetics and the resulting aggregate morphology[17–19]. Assembly and disassembly of aggregates can be then regulated by environmental conditions[18,19]. In Chapter 4 of this thesis the effect of pH and temperature on the aggregation states of α-casein will be discussed.

The complexity of protein life resulting from a coupling of chemistry and "movement" on different time and space scale gives proteins the extraordinary capabilities to interact also with other molecules such as other proteins, metals, lipids etc. underling the dynamic processes in living cells fundamental for life[20–22].

1.2. Membrane composition

Biological membranes consist of two layers of lipid molecules that form a bilayer, which is intercalated with proteins, carbohydrates, and their complexes[23,24]. These bilayers separate cell from the external environment or create intracellular compartments, constituting selective permeability barriers[23]. The main components of the bilayer are usually the amphiphilic phospholipids constituted by a hydrophilic phosphate head and a hydrophobic tail consisting of two fatty acid chains. The polar head group can be either charged or neutral (zwitterion). When phospholipids are exposed to water, the polar head groups of lipids like to stay in water while the hydrophobic hydrocarbons tails try to avoid it. Therefore, phospholipids self-assemble spontaneously and rapidly into a two-layered sheet with the hydrophobic tails pointing toward the center of the sheet. The driving forces are the hydrophobic and the van der Waals interactions between tails[23]. Membranes thus form non-covalent cooperative structures. Physico-chemical interactions due to charged and polar groups, ion pairs, hydrogen bonding, and other less specific electrostatic interactions, impart important properties both to membranes. The nature of the phospholipids present in the membranes significantly influences the charge, thickness, phase and fluidity of bilayers[24–26]. Membrane fluidity, inversely proportional to membrane viscosity, is a complex parameter, influenced both through some biophysical (temperature, electrical charges, pH) and biochemical factors (protein/phospholipids ratio, phospholipids/cholesterol ratio, degree of fatty acids unsaturation). Fluidity determines how easily solvent molecules, lipids and proteins can diffuse laterally in the plane of the membrane[27]. It is also related to water accessibility of the bilayer[28,29]. In model, this property can be tailored combining lipids with different melting temperatures (T_m), which depend on some properties such as chain length, degree of unsaturation

and head group shape[27]. Above T_m, lipids are in a fluid liquid crystalline phase and so more accessible to water molecules, while below this in a more solid gel phase. In addition to phospholipids, also the other molecules included in the bilayer such as sterols, carbohydrates and integral (enzymes, transporters, receptors) and peripheral proteins, in variable proportions, can influence membrane fluidity. Changes of membrane fluidity have also been found connected with pathologies such as Huntington disease [30]. In particular, it has been discovered that a perturbation in biosynthesis of fatty acid or disruption of transport mechanisms of lipid, involved in this disease, induces an increased membrane fluidity and shift toward liquid disordered phase [30]. In apoptotic cells membrane fluidity was observed to decrease due to the increase of water accessibility of the membrane[31–33].

Lipid order can be sensed either through monitoring the local viscosity by molecular rotors [34] or lipid packing by mechanosensitive dyes [35] as well as through local polarity using solvatochromic dyes. Solvatochromic dyes generally detect ordered lipid phases as less polar environments because their tight packing excludes polar water molecules and freezes dipolar relaxation processes [36,37].

Furthermore, differences in terms of phospholipid and sterol composition are at the basis of the different properties that characterize organisms such as bacteria and mammals. In particular, the cell membranes of bacteria are rich in acidic phospholipids, such as phosphatidylglycerol, cardiolipin and phosphatidylserin that are responsible for their overall negative charge. Other components, such as the lipopolysaccharides in Gram-negative and teichoic or teichuronic acids in Gram-positive bacteria, present in the cell wall confer an additional negative charge to the surfaces of these organisms [20].

In mammalian cells, acidic phospholipids are usually only present in the inner leaflets of plasma membranes, while the outer leaflets are mainly composed of zwitterionic phospholipids such as phosphatidylethanolamine, phosphatidylcholine, and sphingomyelin that provide a membrane with a neutral net charge[38]. Mammalian cell membranes, unlike those of bacteria, have a high content of cholesterol that stabilizes the phospholipid bilayer and decrease its permeability to solutes[38,39]. Since membranes form the boundaries between-biological systems, their permeability for various molecules is crucial for function and control.

The differences in bilayers composition in term of exposed permeability, charges, fluidity etc. can have different effects in protein interaction, insertion and action.

1.3. Protein/peptide-membrane interaction

Protein-membrane interactions are implicated in a broad range of biological processes, such as protein trafficking, cellular signaling, ion channel formation that are fundamental for the development of cellular functions[20]. Beside peripheral and integral membrane proteins, mentioned above, there is a class of proteins, known as amphitropic, which reversibly interacts with lipid and membranes during their biological activity [40].

Examples are vinculin and α-actin that transiently interact with the hydrophobic part of membranes, regulating the interaction between membrane and cytoskeleton[40,41]. Other are the Protein kinase C and cytildylyltrasferase that, binding the membrane lipids, regulate in the protein's catalytic functions or the Phospholipases implicated in cellular communication. Also the α-lactalbumin and α-casein belongs to this family [42,43]. They are biosynthesized in the rough endoplasmic reticulum (ER) of the mammary gland cells during the lactogenesis and need to bind the lipid membranes of the ER microsomes to be transferred to Golgi apparatus during their secretory pathway. These organelles of the secretory and endocytic pathways are distinguished by their luminal acidity that varies from pH 8 to pH 4.7[44]. As explained before, these wide pH modifications may induce changes in both key residues or in global charge of the proteins that produce protein conformational changes altering the protein ability to interact with targets or to exploit specific functions. pH variations of similar extent will be used, in the Chapter 4, to mimic such charge changes on α-casein, which consequently modify protein-membranes interactions.

However, whether membranes or intracellular organelles are the targets of proteins, the interaction with membranes is the key factor in carrying out the activity. During the interaction, both the protein and the membrane may experience a series of structural changes[45]. Due to common nature of the involved stabilizing interactions, proteins can affect the configuration of the membrane surface, increasing or not the surface curvature, the fluidity of the lipid structures[46–48]. At the same way, lipids can induce structural transitions of proteins[49,50] favoring or not the exposure of reactive non-polar group or regions and/or charged groups buried inside the native structure of the proteins, necessary for the binding and/or to drive the stabilization or dissolution of aggregates. This is what occurs, for example, to α-lactalbumin and apocytochrome c, which are relatively unstructured and/or flexible in solution but become partly α-helical upon interacting with anionic lipids [51].

Many researchers had provided strong evidence that the forces involved in the protein-membrane interactions are especially the ionic and the hydrophobic ones [52,53]. Ionic bonds, strong interactions that occur between ionic species of the opposite charges, can occur between the positively (Arg, Lys, His) or negatively (Asp, Glu) charged residues of proteins and the anionic or cationic head groups

of the lipids in the membranes, respectively. In the other hand, hydrophobic interactions could involve the hydrophobic segments of the proteins and the hydrocarbon chains of the membranes, driving the insertion of a hydrophobic protein segment into the lipid bilayer.

Therefore, these interactions strongly depend on both the membrane lipid composition[54,55] and structural details (e.g. charge, hydrophobicity, steric hindrance) of the bioactive peptide chains, and may furthermore change depending on environmental conditions (temperature, pH, presence of co-solvents). For example, the temperature influences the fluidity of phospholipid bilayer and consequently its permeability to the molecules but it also effects on the conformation and the aggregation state of the proteins. By modifying temperature, as well pH, it is in fact possible to denature the protein and induce the exposure of buried portions fundamental for the bond with the membranes. An example is provided by the α-lactalbumin that binds the negatively charged lipid membranes at mild acidic conditions (pH<4.5) since it requires protonation of key acidic residues on protein and a loosening of the tertiary structure. The binding does not occur at pH 6-7 [42,56].

1.4. Protein -membrane interaction: toxicity

It is well established that proteins that are 'misfolded', i.e. that are not in their functionally relevant conformation, are devoid of normal biological activity [57]. Many diseases, often known as misfolding or conformational diseases, ultimately result from the presence in a living system of protein molecules with structures that are 'incorrect', i.e. that differ from those in normally functioning organisms. Such diseases include conditions in which a specific protein, or protein complex, fails to fold correctly (e.g. cystic fibrosis, Marfan syndrome, amyotonic lateral sclerosis) or is not sufficiently stable to perform its normal function (e.g. many forms of cancer)[57]. They also include conditions in which aberrant folding behavior results in the failure of a protein to be correctly trafficked (e.g. familial hypercholesterolemia, α1-antitrypsin deficiency, and some forms of retinitis pigmentosa) [57]. In addition, they often aggregate and/or interact inappropriately with other cellular components leading to impairment of cell viability and eventually to cell death.

Considerable attention is presently focused on a group of protein folding diseases known as amyloidosis [58–61]. The formation of amyloid structures is generally believed to be involved in pathologies such as Alzheimer's and Parkinson's diseases, as well as non-neuropathic conditions such as type II diabetes and systemic amyloidosis[13,62]. Both mature amyloid *fibrils* and transient *oligomeric* species [63,64] formed during protein aggregation or released by mature fibrils[65] were found

to be cytotoxic through different mechanisms, which often involve membrane destabilization [66–68]. Specific molecular structural characteristics of prefibrillar *oligomers* that include the small size, exposure of hydrophobic surfaces, and unsaturated edge-strands enhance their ability to induce neurotoxicity [62,69,70]. For example, the severity of cognitive impairment in Alzheimer has been shown to better correlate with low-molecular weight and soluble Aβ aggregates[70]. In the same way, the use of rifampicin to prevent human IAPP (hIAPP) fibril formation (linked with type II diabetes), but not the oligomerization, was proven to be insufficient in protecting beta-cells from apoptosis[69].

Amyloid *oligomers* can interact with biological membranes, with affinities that, as mentioned above, can be modulated by several factors including the properties of the membrane and the lipid composition. The latter can generate a wide range of different surface environments in terms of hydrophilicity/hydrophobicity, electrostatic charge, polarity, fluidity, curvature, and lateral pressure that can influence profoundly protein conformational changes and folding. In this way membranes may act as conformational catalysts and active surfaces that can favor their misfolding and aggregation prone conformations, by direct interaction with protein hydrophobic or charged groups or for the accumulation of proteins in a crowded environment at liquid/lipid interface or by favouring nucleation mechanisms[33,58]. For example, an important lipid player affecting membrane efficiency to recruit and unfold proteins/peptides and to nucleate amyloid growth is cholesterol although its action is controversial. Some data suggest that cholesterol, clustered with ganglioside lipids and sphingomyelin to form rigid microdomains known as lipid rafts, anchors the amyloidogenic proteins to membranes and influences their fibrillization rates[71]. This is the example of the Aβ peptide whose toxicity is associated with the formation of oligomeric-Aβ/cholesterol domain complexes[72,73] in the cell membrane. Otherwise, several pieces of evidence support a protective role of increased cholesterol against amyloid growth. It has been observed that a reduction of the cholesterol content results in increased ganglioside GM1, the most abundant negatively charged lipid found in the outer leaflet of the neuronal cell membranes, expression. GM1 can bound by Aβ peptide and act as a seed for Aβ aggregation accelerating amyloid fibril formation[74].

In turn, the aggregation may induce disruptive structural alterations in cell membranes trough a number of mechanisms including specific membrane pores formation, membrane destabilization or thinning or breakage due to induced growth of lipid bilayer rigidity. In some cases, it was also observed that amyloid growth into or amyloid adsorption to lipid bilayers can heavily damage membranes by extracting membrane lipids and modifying profoundly membrane stability and

order, lipid packing, and hydration at the interfacial region, as was shown in the case of β2-microglobulin [75] and lysozyme[76]. Another molecular mechanism proposed is based on the lipid-chaperone hypothesis[77,78] . According to the latter, free lipids in the aqueous phase could interact with amyloidogenic proteins in the water phase, giving rise to a lipid-protein complex, globally possessing a higher hydrophobicity and, in turn, a higher affinity to the membrane compared to the bare protein. A detailed understanding of the relation between aggregation and membrane disruption requires the characterisation of the interactions involved in the binding to membranes of amyloidogenic proteins in fibrillar, oligomeric or in native state and of the membrane bound peptide conformation in a given aggregation state [58].

Another example of protein whose structure and consequent fibril formation is influenced by lipid membrane is the alpha-synuclein (α-Syn), a 140-residue natively unfolded protein abundantly expressed in neurons, especially presynaptic terminals. It is included in the family of the amphitropic proteins[79] and directly involved in Parkinson disease.

Several studies have demonstrated that α-Syn is able to interact only with phospholipid vesicles containing acidic phospholipids such as phosphatidylserine and phosphatidylinositol, while it has been shown that membranes constituted by neutral phospholipids such as phosphatidylcholine and phosphatidylethanolamine do not bind the protein. It was suggested that the amphipathic N-terminal region of α-Syn, rich in positively charged lysines, is directly involved in the binding to negatively charged lipid membranes demonstrating that electrostatic forces play an important role in the binding, even if different studies have also shown that they are not the sole driving force. After binding, it adopts an extended helical conformation, while C-terminal region of the protein remains unbound and available for potential interactions with other proteins. As α-Syn, also Aβ peptide[80,81], β-2 microglobulin and hIAPP peptide[82] have all been shown to shift to an α-helical structure upon negative charged membranes binding. However, there are also evidences that some brain lipids are able to resolubilize mature β-amyloid fibrils into oligomeric toxic species[83]. Some works have also demonstrated that elements of the basement membrane, such as laminin, collagen IV and entactin inhibit the formation of beta-amyloid protein fibrils. This discovery may provide a new therapeutic way for Alzheimer's disease[84,85].

1.5. Proteins and peptides as anticancer- antimicrobial agents

Epidemiological studies have shown that some proteins and peptides have also the ability to protect against cancer and infections and that a lot of them are effective to both types of treatment[86,87].

Among them, bacterial proteins are a promising group of bioactive compounds and potential anticancer and/or anti-infection drugs. They include enzymes (arginine deiminase, L-asparaginase), bacteriocins (pediocin, colicin), toxins (botulinum toxin A, exotoxin A) etc [86]. Although they often act on intracellular targets, the interaction with membranes is necessary to arrive to cytoplasm[88–90]. There are also proteins naturally produced by mammals, like human and bovine α-lactalbumin that have demonstrated to induce death of tumor cells, acting on nucleus, but they have also demonstrated to have antimicrobial effects against Gram positive bacteria [42,91]. Other proteins, with antibacterial activity, are lysozyme, phospholipase A2 and lactoferrin that are part of the innate immune system in most mammals. Lysozyme, for example, naturally found in bodily secretions such as tears, saliva, has shown antibacterial activity by cleaving the peptidoglycan component of bacterial cell walls, leading to cell death [92].

Also peptides that can be produced by prokaryotes (nisin, gramicidin from Lactococcus lactis, Bacillus subtilis, and Bacillus brevis), by humans (cathelicidins and defensins) [93] or generated by the proteolysis of α-lactalbumin, β-lactoglobulin and lactoferrin have shown the ability to kill pathogenic microorganisms, including Gram-positive and Gram-negative bacteria, viruses, protozoa, and fungi [94].

In higher organisms, they constitute important components of the innate immunity, protecting the host against infections; in contrast, bacteria produce peptides in order to kill other bacteria competing for the same ecological niche. All these peptides belong to the family of the "antimicrobial peptides" (AMPs).

Growing evidence supports also an anticancer activity of some AMPs. For example, LL-37, the only cathelicidin in humans, has been shown to inhibit tumor growth in colon cancer and gastric cancer [95,96].

However, it has also been discovered that LL-37 is able to interact with extracellular DNA and to mediate uptake and nuclear transfer of functional plasmid DNA in mammalian cells[97]. In fact, it is not excluded that some of AMPs can also act as cell penetrating peptides (CCPs). Peptides belonging to this family are able to pass through the cell membrane and to act as vectors for the delivery of chemically conjugated biomolecules such as peptides, oligonucleotides, and chemotherapeutics [98]. It is not clear if there is an evidence difference between AMPs and CPPs because some AMPs are able to cross membrane bilayers and some CPPs show antimicrobial activities and thus, a clue to their different activities is derived from their interactions with the lipid bilayer [20]. Anyway, the nature of the primary sequence appears to be of great significance for the activity, as a high content of

cationic amino acids is a prerequisite for their initial association with negatively charged membrane components. In addition, the ratio between the cationic lysine (Lys) and arginine (Arg) residues influences membrane selectivity since the guanidino functionality of Arg promotes a more efficient interaction with eukaryotic membranes as compared to Lys. This is, however, most often at the expense of increased cytotoxicity. In opposite, a high Lys content has been correlated with selectivity towards bacterial cells over eukaryotic cells.[99]

An example of peptide, known to be both a charrier for drugs and also an antibacterial and anticancer agent, is the Trasportan 10 peptide. Chapter 3 of the thesis will be focus on the study of the behavior of this peptide in presence of lipid membranes, different both for membrane and internal composition, with the aim to understand the forces driving or hindering the peptide-membrane interaction and the effects induced both on peptide conformation and on physical-chemical properties and integrity of the membranes.

1.5.1. Antimicrobial peptides

Today, the interest toward AMPs, results from the rapidly increasing resistance toward conventional antibiotics, from the side effects of chemotherapy and drug resistance of some cancer types, which are forcing scientists to identify new and non-conventional anti-infective therapies[100].

AMPs are relatively short peptide, commonly consisting of 10-50 amino acids, and their secondary structures include α-helix, β-sheet and loops. They display an overall positive charge ranging from + 2 to + 11 (often due to the Lys and Arg residues), and contain a substantial proportion (typically 50%) of hydrophobic residues such as tryptophan and phenylalanine [38,100,101]. The combination of charged and hydrophobic domains plays a key role in the interaction with natural membranes; the charged moieties are involved in the initial interaction with the bilayer while the hydrophobic domain is crucial for insertion [20,93]. The selectivity of these peptides toward microbial cells and/or cancer cells is connected to the differences in membrane composition between microbial, cancer and mammal cells [87,102]. The propensity of these peptides to adsorb, fold, and form functional structures or aggregates at the membrane surface, even at low peptide/lipid ratios, suggests that an attractive force operates between them. The negative charged surface of bacteria is determinant for the interaction driven by electrostatic forces with cationic AMPs while the presence of zwitterionic phospholipids in mammal's membranes hinder the action of AMPs. Furthermore, compared with normal cells, the anionic composition of cancer cells' membrane surface confers the targeting specificity of AMPs [93]. Although the AMPs share many characteristics with amyloid-forming proteins,

such as the affinity for negatively charged membrane surfaces and the conversion from random-coil structures to α-helixes upon initial contact with membrane surfaces, the presence of cholesterol, present in mammal's membranes, hinders the binding of AMPs[102].However, there is a limit beyond which increasing positive charge and/or hydrophobicity no longer confers increased activity[38]. For the magainins for example, a net charge of 6 to 7 led to an increased hemolytic propensity and a loss of antimicrobial activity. This decrease in antimicrobial activity may result in part from excessively strong peptide interactions with phospholipid head groups, thereby preventing translocation of the peptide into the cell interior.

About hydrophobicity, although it is required for effective membrane permeabilization, increasing levels of hydrophobicity are strongly correlated with mammalian cell toxicity and loss of antimicrobial specificity [38]. Therefore, it is important that antimicrobial peptides are moderately hydrophobic and positively charged, such that they optimize activity against negative microbial cell membranes.

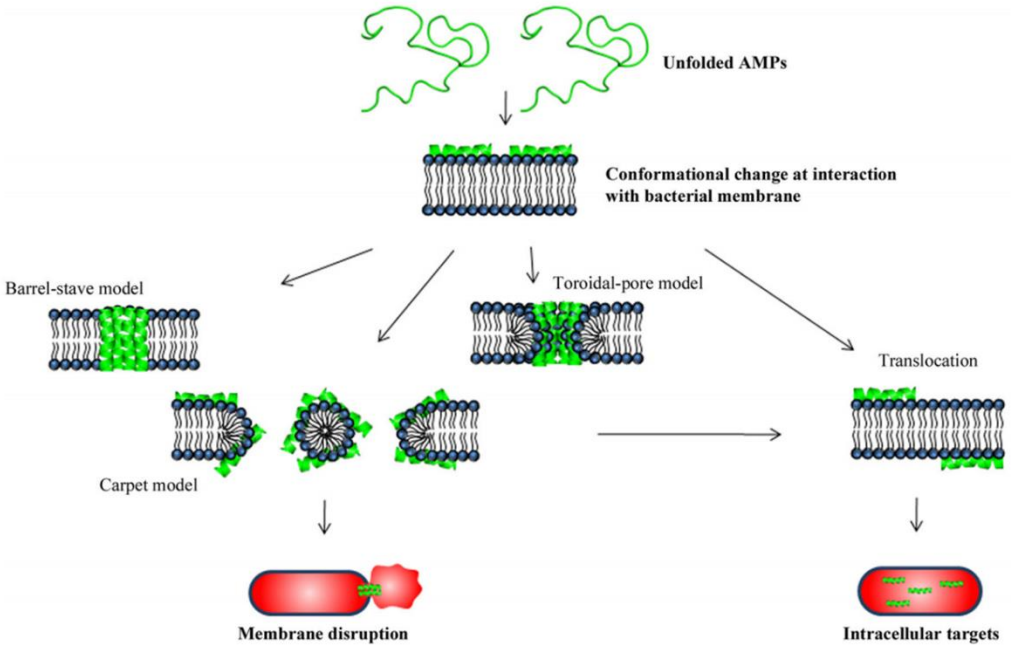

Figure 1.2. Schematic illustration of bacterial killing mechanisms by AMPs. Figure and caption are adapted from the original paper [87].

A simply classification of AMPs is based on mechanism of action (Fig. 1.2) [87]. Several models, including "toroidal pore", "barrel-stave" and "carpet" models, have been proposed describing the events occurring at the bacterial cytoplasmatic membrane [87,103] and which ultimately can lead to its permeabilization and/or disruption, leading to cell death. AMPs can in fact act on membranes by

modifying their physical integrity by inducing the formation of pores, thinning or breakage of the membrane [38,87].

The main differences between these models lie in the lipid structure around the pores and the pore stability. In the *barrel-stave model*, the lipids maintain a lamellar organization and the peptides form well-defined and stable bundles, which, when they are of a sufficient diameter, can serve as a pore. In the case of the *toroidal-pore model*, the lipids create a toroidal-shaped opening covered with the peptides in different orientations and the pores are generally less stable or transient. In the *carpet model*, peptides accumulate on the membrane surface and destroy the cell membrane in a 'detergent'-like manner inducing the formation of micelles. In contrast, some AMPs penetrate the membrane without significantly disrupting it to interact with intra-cellular targets leading to cell death.

1.6. Model cell membranes to study protein/membrane interaction

Model cell membranes are systems in which the lipid organization mimics the arrangement of lipids in natural cell membranes. Given the structural complexity of membranes, for the presence of many interconnected variables, the understanding of lipid–protein interaction is a complex biophysical problem and the use of models is useful [104]. As explained above, the cell membrane consists in fact of two layers with an asymmetric lipid composition and contains proteins with high specialization, such as specific ion-channels and receptors and it is organized in micro domains, termed rafts, essential for the biological function of membrane proteins. For this reason, it is preferable to study and to understand the properties of model systems whose composition can be easily tailored. This approach allows to analyze single, specific features of protein-membrane interaction and add complexity to the system one step at the time, e.g., by adding different lipids and/or protein to the membrane composition.

1.6.1. Liposomes: simple artificial model lipid membranes

Liposomes are frequently used as simplified models for cellular membranes in basic studies and are self-closing spherical particles consisting of lipid bilayers that encapsulate an internal aqueous environment so that, depending on the size they can be assimilated to certain types of organelles membrane [105]. Additionally, because of their ability to compartmentalize their internal aqueous environment from the external environment, they can be used in drug delivery and membrane integrity assays. The procedure for making liposomes is relatively simple and relies on hydrophobic interactions between lipid molecules and an aqueous solution [101].

As shown in Fig. 1.3, they can be prepared as multilamellar vesicles (MLVs), which are concentric multi-bilayer vesicles having an onion-like structure with an average diameter ranging between 1 µm and 5 µm or can be formed into large (LUVs, > 100–250 nm to 1 µm in diameter), small (SUVs, 20 to 100 nm diameter) or giant (GUVs, > 5 µm diameter) unilamellar vesicles [106,107].

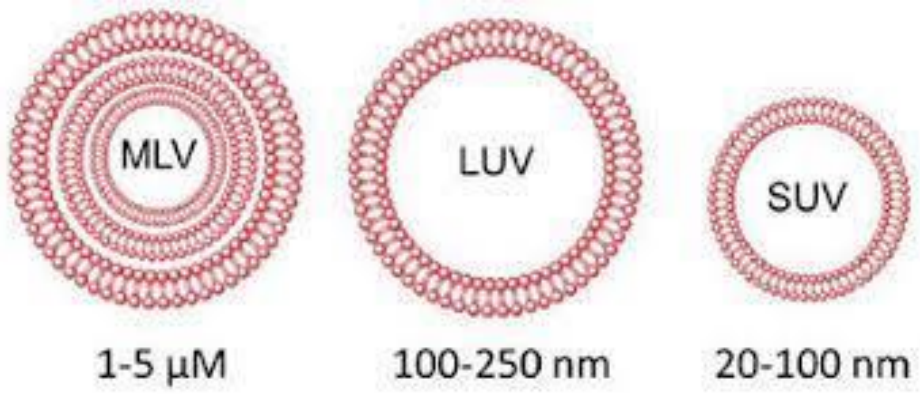

Figure 1.3. Classification of liposomes based on their lamellarity and size.

The size of the liposome produced affects the curvature of the bilayer and as a consequence it affects lipid packing, this in turn may modulate the ability of some proteins to bind.

The bilayer of GUVs is thought to possess more similar physical properties to the bilayer [101]of cells and has shown a great advantage over smaller liposomes such as LUVs and SUVs in investigating the physical properties and structural changes of liposomes [19,46,47,108]. So far, almost all studies of liposomes have been carried out on a suspension of many small liposomes such as LUVs and SUVs using light scattering, fluorescence spectroscopy, electron spin resonance, and X-ray scattering. In these studies, the average values of the physical parameters of liposomes have been obtained from large numbers of liposomes, and thereby much information has been lost. In contrast, studies of single GUVs provide information on the structure and physical properties of single GUVs as a function of time and spatial coordinates (the single GUV method) [55,108–110]. In this way, the single GUV method provides a great deal of new information on the structure and function of bio membranes and lipid membranes, which cannot be obtained by the studies on the suspension of LUVs and SUVs. For example, the single GUV method has been successfully used to study shape change of vesicles, membrane fusion and vesicle fission in real time by microscopy [107]. In addition to unilamellar giant vesicles, some studies have also used giant multilamellar vesicles (GVs) because it has been found that higher degree of lamellarity can induce greater stability [111]. These systems have been used to study the effect of α-Syn and α- lactalbumin on lipid bilayers, with different lipidic composition, trough spectroscopy and advanced fluorescence microscopy techniques [47,48,112].

However, although the lipidic GVs represent the simplest bio mimicking model compartment that allow, in the first phases, the investigation of biological processes (permeability, fluidity and dynamic behavior of cell membranes), they present a significantly lower level of complexity of membranes of living cells. GVs can in fact only approach living cells to a certain degree due to the lack of a cytoplasmic medium and simultaneous presence of more than one type of membrane protein inside their membrane.

1.6.2. Giant Plasma Membrane Vesicles as model membranes

The problems connected with synthetic vesicles have brought the scientists to the development of a method to produce cell-mimicking compartments giant plasma membrane vesicles (GPMVs), directly from living cells [113]. These systems are an interesting alternative to synthetic vesicles as an experimental model system for use in a wide range of assays.

These systems present a high stability and provide experimental tractability similar to synthetic membranes. Importantly, the membrane and internal composition directly mirror the composition of the cells from which they originated, except for larger cellular organelles and intracellular structures (e.g., nuclei, Golgi apparatus, vesicles). This combination has allowed investigation of GPMVs composition, physical properties, dynamics, and potentially signaling and transport in isolation from the complexity of living cells.

Widely used common cell lines like HepG2, HeLa, Caco-2 have already been used for the production of GPMVs and pretty simple protocols have been developed. In particular, their formation can be induced in short time (1-2 hours) by using of a "vesiculation buffer" [113,114]. Chemically induced plasma membrane vesiculation was first observed in the 1970s [115]. Basically, the simple preparation protocol is sketched in Fig. 1.4.

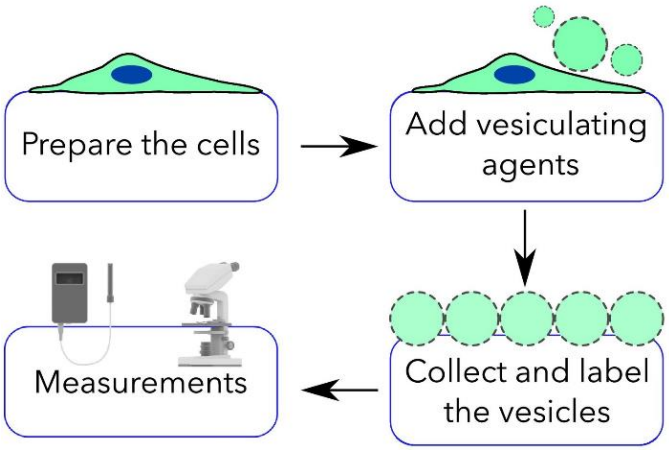

Figure 1.4. Overview of GPMVs preparation protocol. Figure and caption are adapted from the original paper [116].

Once formed, the vesicles present a perfectly spherical shape, with a diameter of about 10 μm. GPMVs can be visualized by bright-field microscopy because of the refractive index difference between the cytoplasm inside the GPMVs and the buffer outside (Fig. 1.5). Alternatively, GPMVs can be imaged using fluorescence microscopy by labeling cellular plasma membranes with fluorescent markers before vesiculation, or direct labeling of isolated vesicles.

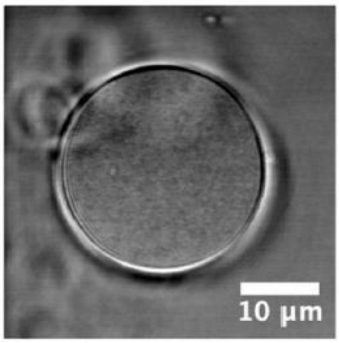

Figure 1.5. Example of GPMV isolated from HepG2 cells. Figure adapted from the original paper [117].

Because of the main experimental advantages, and despite of the fact that they still present several important differences with live cell membranes, GPMVs constitute a widely used tool in recent membrane biophysics studies as they provide the possibility of having large experimental repeatability.

Moreover, GPMVs are excellent models in biophysical studies for the analysis of molecular interactions, which are difficult to measure in live cells due to the complex reaction due to functional activity which may hinder repeatability. These structures provide a clean system free from artifacts that can be caused by endo- and exocytosis processes and disturbances from intracellular dynamics. GPMVs have been used in several experimental settings including membrane phase separation, membrane dynamics, membrane composition, drug delivery, and lipid-protein interactions [116]. In addition, in the recent years the complexity of GPMVs has been increased encapsulating within them nanocompartments, containing enzymes, which act as artificial organelles. This, in order to mimic the architecture and functionality of eukaryotic cells.

Chapter 2

Experimental approach

In this chapter the fundamentals of the experimental techniques used in this thesis will be shortly described together with summary of the methods used in the performed experiments.
Main aim of this chapter is to highlight the rationale of combining bulk spectroscopic information with quantitative microscopy to analyse such complex multiplayer, spatially heterogeneous phenomena as protein-membrane interactions. The presented approach allows to monitor the time evolution of the involved events, since the early stages, providing information from the different point of view of both protein molecules and membranes.
Bulk experiments, such as circular dichroism (CD) and steady state fluorescence in cuvette, give the possibility to systematically investigate the occurring reactions, providing averaged information on the behavior of an ensemble of molecules. Quantitative fluorescence microscopy methods are used to follow dynamic events, in real time without sample manipulation, providing information on the occurring events with molecular details. In this way, protein fate can be simultaneously evaluated with membrane changes giving, as an output, quantification and localization of spatially heterogeneous events.

Techniques

2.1. Fluorescence

Fluorescence is a really powerful parameter useful for studying biological systems and the dynamic processes occurring between them. In fluorescence, light absorption promotes an electron to an excited state, resulting in light emission when the excited electron returns to the ground state undergoing a radiative transition [118]. The processes, which occur between the absorption and emission of light, are usually illustrated by the Jablonski diagram (Fig. 2.1). In particular, excitation by absorption of light lifts electrons of the molecules within femtoseconds from the ground state S_0 to higher singlet excited states. Then, the electrons undergo vibrational relaxation to the lowest vibrational level of the excited state (denoted as S_1) by non-radiative processes called internal

conversions. Once the dye molecules have reached the lowest vibrational level of S_1, they can relax to the ground state S_0 by a radiative or non-radiative process.

Fluorescence is a radiative process in which the molecules (fluorophores) decay from the S_1 to the ground state by emitting detectable photons (on the timescale of 10^{-9} s).

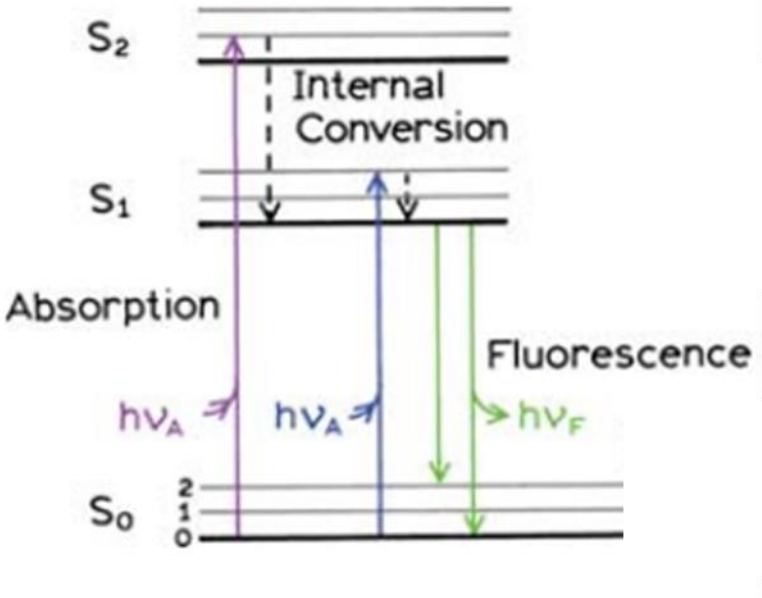

Figure 2.1. Jablonski diagram. The figure is adapted from first chapter of [118].

The energy loss in vibrational relaxations and internal conversions to reach the level S_1 results in a shift to longer wavelengths (red shift) of fluorescence emission with respect to absorption (Stokes shift).

The efficiency of the emission is defined by the quantum yield (Φ), which is the ratio of the photons emitted over the total photons absorbed [119,120] . Furthermore, it can be shown that Φ is the ratio of the rate of the radiative transition (k_r) to the sum of rates of all transitions ($k_r + k_{nr}$), in which the excited state is involved. Therefore, any molecular mechanism leading to a non-radiative depopulation of the excited state reduces the quantum yield:

$$\Phi = k_r / k_r + k_{nr} \quad (1)$$

The other important characteristic feature of fluorescence is its time response [121]. In particular, the population of the excited molecules generated at the moment of excitation, t = 0, starts to decrease exponentially through the radiative (k_r) and non-radiative (k_{nr}) transitions to the ground state. The characteristic time of this process, τ, is called the fluorescence lifetime:

$$\tau = 1/ k_r + k_{nr} \quad (2)$$

Both fluorescence spectroscopy and fluorescence microscopic techniques were used to analyse the fate of proteins, their aggregation/disaggregation processes as well as their absorption and/or insertion into membranes. At the same time, these methods allowed to study and quantify morphological and physical modifications occurring in the membranes. The parallel analysis of intrinsic (tryptophan) and extrinsic dyes (Nile Red, ANS, Pyrene, Laurdan and di-4-Aneppdhq) was essential for a comprehensive understanding of the processes.

2.2. Steady state fluorescence spectroscopy in bulk

Fluorescence spectroscopy measurements provide *bulk* information about the sample and the events occurring within it.

2.3. Fluorescence microscopy

In order to visualize and to follow in real time, in a non-invasive way and at sub-cellular level aggregation processes, protein-membrane interactions, and consequential possible morphological vesicles modifications, fluorescence spectroscopy was coupled with fluorescence microscopy such as confocal and two-photons microscopy. Both methods give information on the events dynamics and chemical interactions at resolution down to about 200 nm where the spatial resolution of an instrument is its capability to resolve details in a specimen[122,123]. In particular, it can be quantified as the minimum distance that can be measured between two objects in an image still allowing distinguishing them as separates. The resolution limit can be described by the Abbe's following law:

$$\Delta x = \lambda/2NA \quad (3)$$

where Δx is the minimum distance between two points in the image, λ is the wavelength and NA is the numerical aperture and is defined as:

$$NA = n*\sin \alpha \quad (4)$$

with n being the refractive index of the surrounding medium and α half of the angle of the aperture of the objective.

2.3.1. Confocal laser scanning fluorescence microscopy (CLSM)

Confocal laser scanning microscopy (CLSM) is a widely used technique that enables the three-dimensional imaging of biological samples by selectively accessing the fluorescence signals from different planes inside the sample and assembling the planar images to generate three-dimensional images.

CLSM aims to overcome some limitations of traditional wide-field fluorescence microscopes[122]. In a conventional (i.e., wide-field) fluorescence microscope, the entire specimen is flooded evenly in light from a light source: all parts of the sample can be excited at the same time and the resulting fluorescence is detected by the microscope's photodetector or camera including a large unfocused background part. In contrast, using CLSM the images are created by sequentially measuring all the pixels in an image. This is accomplished by scanning a focused laser beam across the sample and measuring the intensities at each position. CLMS fundamental element is a pinhole that blocks the fluorescence generated from the regions out from the focal point, to eliminate out-of-focus signal. As only light produced by fluorescence very close to the focal plane can be detected, the image's optical resolution, particularly in the sample depth direction, is much better than that of wide-field microscopes. However, as much of the light from sample fluorescence is blocked at the pinhole, this increased resolution is at the cost of decreased signal intensity and to offset this drop in signal after the pinhole, the light intensity is detected by a sensitive detector. Measured fluorescence signal comes from molecules localized in a tiny region at the focus. As the focus position moves in the x-y plane, light is delivered to sequential points of the sample and the emission signal reconstructs the distribution of fluorescent objects with high resolution providing optical sections of the sample.

2.3.2. Two-photon microscopy

Unlike the one-photon excitation, which typically requires photons with energies in the ultraviolet or visible spectral range, to generate fluorescence by means a two-photon process, two different photons with energies in the infrared range must be absorbed simultaneously by the same fluorophore[122]. The sum of the energy of the photons required in a two-photon absorption event must be equal to the energy needed for the single-photon absorption. This phenomenon may also occur with multiple photon absorption e.g. three-photon excitation needs the absorption of three photons and so on. The comparison between one-photon and a two-photon excitation process is

schematically illustrated in Fig. 2.2, where the transition to the excited state induced by two photons is of lower energy with respect to the energy gap between the two electronic levels. The near infrared excitation has the advantage of reducing photo-damages of samples along the excitation beam trajectory permitting minimally invasive experimental measurements also for long acquisition time. In addition, in two photons microscopy, the excitation is limited in a single point with the sample, so that in other parts of the specimen, two-photon absorption generally does not occur minimising the out-of-focus background signal. The near infrared excitation enhances the ability to image deeper (to millimeter scale) in the samples as the contribution of light scattering effects is reduced. This because scattering intensity can be considered inversely proportional to the fourth power of wavelength of incident light on a sample; then it is critically reduced if the excitation wavelengths are doubled.

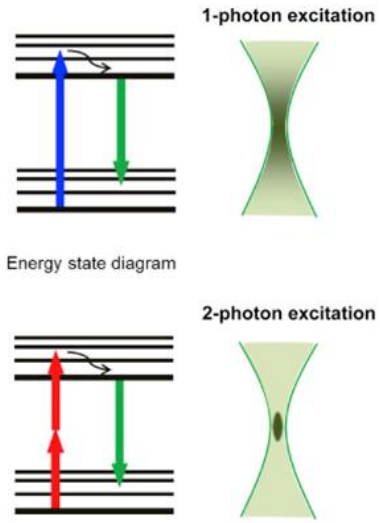

Fig. 2.2. Jablonski diagram and schematic representation of the localization of one-photon and two-photon excitation. In the first case, all the molecules in the illuminated volume pass to the excited state by the absorption of a single photon, while in the second case only molecules at the focal point are excited by the absorption of two photons and emit fluorescence.

In this thesis, two-photon excitation is used for Laurdan measurements, as it enables UV light excitation of the dye avoiding photo-bleaching phenomena that would occur otherwise. The use of pulsed laser also allows FLIM measurements.

2.4. Fluorescence lifetime imaging microscopy (FLIM)

FLIM is a fluorescence imaging technique where the contrast is based on the fluorescent lifetime of chromophores in the sample. FLIM measurements present several advantages when dealing with biological samples which are dynamical and highly heterogeneous [124].

A feature that limits the quantitative interpretation of intensity-based fluorescence images is the lack of knowledge of fluorophore concentration at different locations. A fluorescent dye, for instance, can inhomogeneously accumulate in different regions of a cell due to the intrinsic heterogeneous physicochemical features of the environment. As the measured fluorescence intensity linearly depends both on the quantum yield and on the number of molecules, it is not always easy to separate the two effects. The most important advantage of FLIM over fluorescence intensity imaging is that fluorescence lifetimes are independent of fluorophore concentration and laser excitation intensity [118]. These advantages clearly overcome the apparent difficulty in data analysis and interpretation that data traditionally required specific expertise, complex fitting procedures and the need of sophisticate hardware.

Analysis of FLIM data can be simplified by using the phasor approach that avoids some of the problems of the exponential analysis and provides a graphical global view of the processes affecting the fluorescence decay occurring at each pixel transforming the histogram of time delays into a point in a two-dimensional space termed the phasor plot [125]. The s and g coordinates in the phasor plot are the normalized Fourier sine and cosine transforms and are defined by the following relations:

$$g_{i,j}(\omega) = \int_0^\infty I(t)\cos(n\omega t)dt \Big/ \int_0^\infty I(t)dt \quad (5)$$

$$s_{i,j}(\omega) = \int_0^\infty I(t)\sin(n\omega t)dt \Big/ \int_0^\infty I(t)dt \quad (6)$$

where ω is the laser repetition angular frequency, and the indexes i and j identify a pixel of the image. Since these quantities are normalized to the total number of photon counts, they are independent of the intensity and carry information only on the shape and position of such a curve. Single exponential lifetimes lie on the so-called “universal circle”; long lifetimes are located near the origin (0 on the x axis), while short lifetimes are shifted on the circumference toward the bottom right intersection with the x axis (1 on the x axis). Phasors follow the vector addition rule so that a double exponential decay would lie within the universal circle and along a straight line connecting the phasors of the two isolated components. The distance between each point of the cloud in the phasor plot and the single exponential phasors on the universal circle represents the fraction of each component.

In real measurements, data in the phasor plot appear as clouds of points representing the fluorescence lifetime distributions that can be selected using colored cursors in order to obtain that the corresponding pixels are mapped back with the selected color to the image pixels.

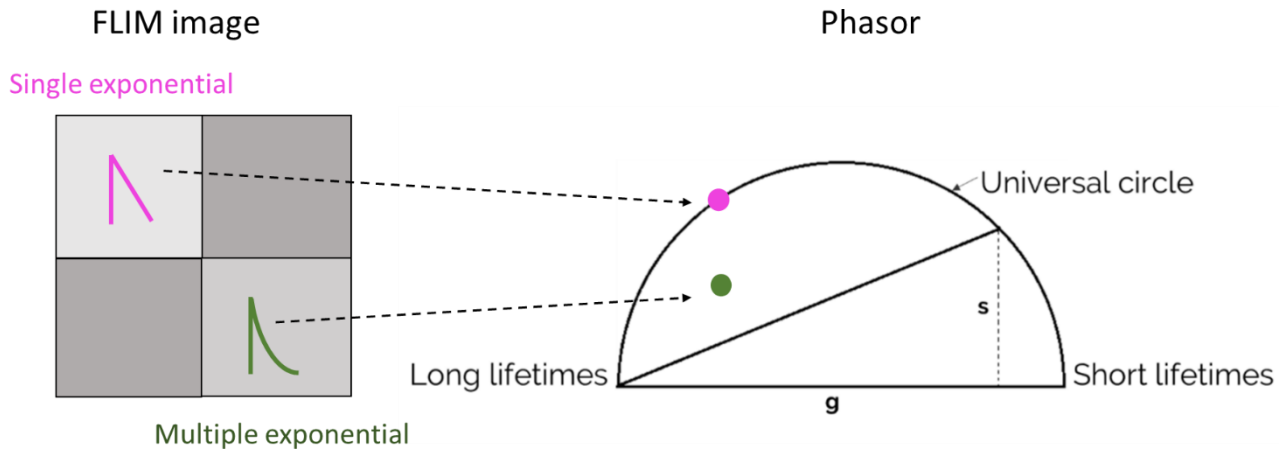

Fig. 2.3. Schematic showing the relationship between the FLIM image and phasor plot with the "universal circle" illustrated. Each intensity pixel value in the image has a corresponding point (pink and green) in the phasor plot. Single exponential lifetime (pink) lies on the universal circle line, while multi-exponential lifetime inside the universal circle. The horizontal (g) and vertical (s) components for an arbitrary lifetime measurement are also shown. The figure is adapted from the original paper [126].

FLIM images reported in this thesis were collected in the time domain using the Leica TCS SP5 microscope coupled with a PicoHarp 300 TCSPC Module (PicoQuant, Berlin, Germany) and the phasor transformation and data analysis are performed using the SimFCS software available at the www.lfd.uci.edu.3.

2.5. Raster Image Correlation Spectroscopy (RICS)

Fluorescence microscopy gives also the opportunity to measure the diffusion properties of single fluorescent particles and characterize their interactions. This can be due using RICS, which is a technique that quantifies the molecular dynamics of fluorescent or fluorescently labelled molecules by measuring fluorescence intensity fluctuations in images taken on confocal microscopes. RICS analysis provides an average value of the diffusion coefficient (D) within selected areas in an image [127,128]. In the hypothesis of free diffusing molecules, D depends on molecular size, shape, and properties of the surrounding fluid. For a spherical particle, the diffusion coefficient is given by the Stokes-Einstein relation:

$$D=\frac{kT}{6\pi\eta R} \tag{7}$$

where k is the Boltzmann constant, T is the temperature (room temperature in our case - 298 K), η is the viscosity of the media (water solution in our case -1.16 cP), and R is the radius of the diffusing molecule. So that larger diffusion coefficient D reveals smaller size of the diffusing particles and changes of its value can provide information on association/aggregation and/or binding processes of molecules.

RICS images are acquired through raster scanning (Fig 2.4 (a)). The 'raster' in RICS refers to the order in which these pixels are collected to generate an image [127]. The top left pixel is measured first. Thereafter, the top row of pixels is collected from left to right. The laser then travels back to the left of the image without collecting any pixels and begins a second row. Rows are collected in this manner from top to bottom until an entire image is obtained. At the end, the obtained images contain information on the microsecond time scale for pixels along the horizontal scanning axis, millisecond time scale along the vertical scanning axis or between scan lines, and on the sub-second to second or longer time scale between successive images. Basing on it during a raster scan, a fast-moving fluorescent particle will be observed across more pixels (Fig. 2.4 (b)) compared to a slower particle (Fig. 2.4 (e)) [127,129]. This can be quantified, calculating from the image the spatiotemporal correlation of fluorescence intensity fluctuations (Fig. 2.4 (d) and (g)).

Image autocorrelation is calculated on each image using the following equation [128]:

$$G(\xi,\psi)=\frac{\langle I(x,y)I(x+\xi,y+\psi)\rangle}{\langle I(x,y)\rangle\langle I(x,y)\rangle}-1 \tag{8}$$

where i(x,y) is the intensity at each pixel of the image, ξ and ψ are the x and y spatial correlation shifts, and $\delta(i)= i - \langle i \rangle$ and the brackets <&> represent averaging over all coordinates of one image.

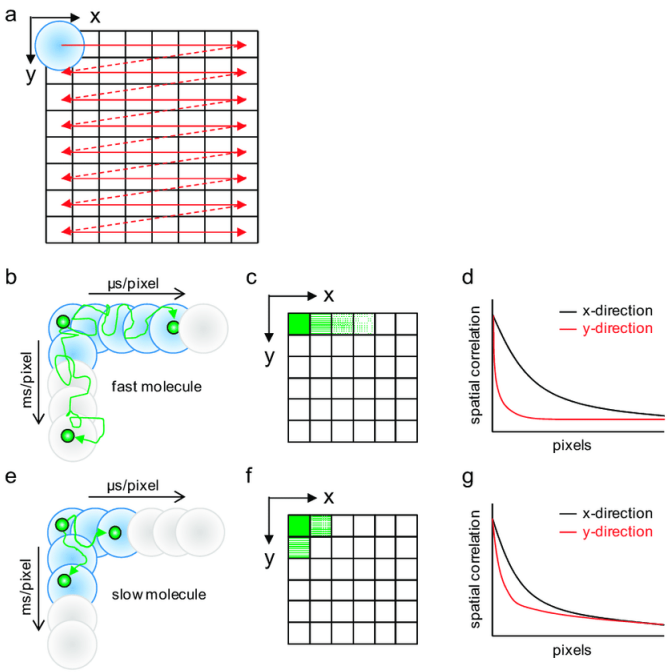

Figure 2.4. The principle of laser scanning microscopy imaging for raster image correlation spectroscopy (RICS) analysis. (a) images consist of pixels from line-by-line scanning. The detectable fluorescent signal (blue circles) and undetectable cases (grey circle) of: (b) fast; and (e) slow moving molecules (green circles) from scans result in the image ((c, f), respectively). The spatial correlation of: (d) fast; and (g) slow moving molecules. Black and red lines represent the correlations calculated from the x-and y-direction pixels, respectively. Figure and caption are adapted from the original paper[130].

The output of measurements are spatial autocorrelation functions, calculated using SimFCS software, like those reported in the Fig. 2.5 (b) and (e). The autocorrelation functions can be fitted using the equation (8), giving as results D and $G_{(0)}$ values; the latter is inversely proportional to the concentration of the fluorophore [128]. The fits of the autocorrelation functions are reported in panels (c) and (f).

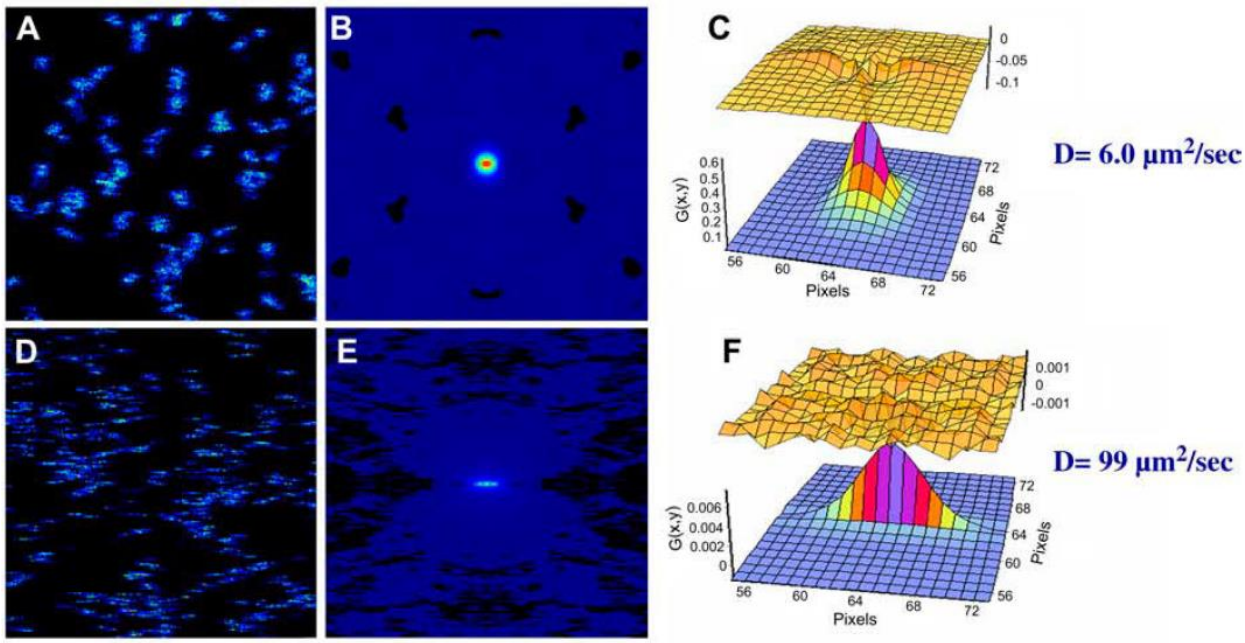

Figure 2.5. (a) and (b) 256x256 images of representative examples of slow and fast molecules, respectively. (b) and (e) the two-dimensional spatial correlation functions of images (a) and (d). (c) and (f) are the fit of the autocorrelation functions (b) and (e). The figures and caption are adapted from the original paper [131].

2.6. Intrinsic fluorescence

Proteins display intrinsic fluorescence that is provided by aromatic amino acids, mainly tryptophan, considering that phenylalanine has a very low quantum yield, and emission by tyrosine in native proteins is often quenched[118].

Tryptophan (Trp) fluorescence is highly sensitive to the environment polarity. For example, the decrease in fluorescence intensity with a shift of the emission spectrum toward higher wavelength (red shift) is due to the exposure of Trp residues to polar environment. In opposite the shift of the emission spectrum towards lower wavelengths (blue shift) indicates an increase in hydrophobicity or compactness around Trp residues. Changes in emission spectra from Trp can occur in response to protein conformational transitions, aggregation processes, binding to other molecules, or denaturation. All these processes can affect the environment surrounding the indole ring and this reflects in spectra changes.

2.7. Extrinsic fluorescence for protein characterization

The use of various extrinsic fluorescent dyes offers additional possibilities for protein characterization. Extrinsic dyes can be covalently attached to proteins (e.g., via the ε-amino group of lysine, the α-amino group of the N-terminus, or the thiol group of cysteine) or can interact non-

covalently with them, e.g. via hydrophobic or electrostatic interactions [132]. Interactions between dye molecules and proteins can lead to changes of fluorescence emission by a change of the preferred relaxation pathway and for this reason have been used for numerous applications in protein sample characterization such as to monitor refolding and unfolding processes, to assess surface hydrophobicity, to probe active sites of enzymes, to characterize aggregation and fibrillation and to monitor conformational changes induced by chemical degradation [132].

An example of fluorescent dye covalently attached to peptide, reported in this thesis, is the **Carboxyfluorescein**. It, linked to the N-terminus of the peptide Trasportan10 (TP10), was used to localize the peptide and analyse peptide behaviour in presence of model membranes with different lipidic composition. Changes of its fluorescence properties (fluorescence intensity, maximum wavelength, lifetime) reflect modifications in the environment surrounding the fluorophore. In particular, fluorescein-based dyes are often used to monitor environmental properties as they are critically sensitive to the pH or the hydrogen-bond character of the environment [133,134]. Changes in the spectral properties of these molecules have also been noted when fluorescein is conjugated to biomolecules, when it is associated with micelles and membranes, when it is incorporated into cells [133]. Therefore, the analysis of Carboxyfluorescein fluorescence changes gave information on eventual TP10 aggregation and/or absorption/internalization in lipid bilayers. In opposite, examples of dyes non-covalently attached, used in the thesis for protein characterization, are the 1-anilinonaphthalene-8-sulfonate (**ANS**) and Pyrene [135]. ANS is a hydrophobic, negatively charged dye whose fluorescence is sensitive to the environment with respect to polarity and viscosity. It is typically used to analyse surface hydrophobicity of proteins and unfolding/folding aggregation conformation. Its interaction with proteins, via hydrophobic and electrostatic interactions between the negatively charged sulfonate groups of ANS and positively charged amino acids (e.g. histidine, lysine and arginine) can result in changes of polarity and viscosity of the surrounding environment and consequential changes in its emission spectrum. In particular, the exposure to a more hydrophobic environment induces a strong fluorescence and a blue shift of its spectrum.

Pyrene is a hydrophobic, uncharged dye frequently used to the evaluation of the critical micelle concentration (CMC) [136,137]. Some proteins, thanks to their amphiphilic structure, are in fact able to assemble together in micellar structures constituted by a hydrophobic core and a hydrophilic shell. In presence of micelles, Pyrene, for its hydrophobic nature, prefers to enter into the micellar structures and this induces changes in its fluorescence spectrum. In particular, the ratio of the

intensities between the third and the first vibronic components of the Pyrene emission spectrum (bands I at 373 nm and III at 383 nm) is a measure of the local polarity and gives information on CMCs of numerous surfactants and micelle stability to environmental changes. In this thesis, ANS and Pyrene were used to evaluate the ability of the amphiphilic α-casein to form micelles at different environmental conditions (pH, temperature), to evaluate their hydrophobicity and their stability to pH variations.

2.8. Extrinsic fluorescence for membrane properties characterization

As reported in previous section membrane fluidity is one of the main determinants of the molecular mobility in the phospholipid bilayer and for this reason essential for numerous cell functions including cell growth, solute transport, signal transduction [138,139]. At the same time, it can be influenced by changes of environmental parameters such as pH, temperature, ionic straight and by the presence of biomolecules that can temporary or permanently interact with them. Therefore, since fluidity regulates cell bioactivity and membrane integrity and even slight changes of it may cause aberrant function and pathological processes, studying this property is fundamental [30].

Fluorescent dyes are frequently used to distinguish the liquid order phase and liquid disorder phase of biological membranes that differ for the concentration and molecular dynamics of water molecules inside them. Examples of dyes used are **Laurdan** and **di-4-ANEPPDHQ** whose structures and the emission spectra in different lipid environments [140,141] are reported in Fig. 2.6. The spectral properties of Laurdan and di-4-ANEPPDHQ alter in response to lipid packing and a blue shift of around 50 nm in the emission peak for both dyes is observed for membranes in liquid ordered (l_o) phase (highly packed phospholipids-few water molecules in the bilayer) relative to membranes in liquid disordered (l_d) phase (more water molecules in the bilayer) [140]. In fact, when the dyes are in membranes characterized by liquid disordered phase, the energy required for solvent reorientation is higher and decreases the excited state energy of the probes. This is reflected in a red shift of the probe's emission spectrum, which can be quantified by the Generalized Polarization (GP) [142]function defined as

$$\mathrm{GP} = \frac{(\mathbf{I_{400-460} - I_{470-530}})}{(\mathbf{I_{400-460} + I_{470-530}})} \quad \text{and} \quad \mathrm{GP} = \frac{(\mathbf{I_{500-580} - I_{620-750}})}{(\mathbf{I_{500-580} + I_{620-750}})} \tag{9}$$

for Laurdan and di-4-ANEPPDHQ, respectively [143].

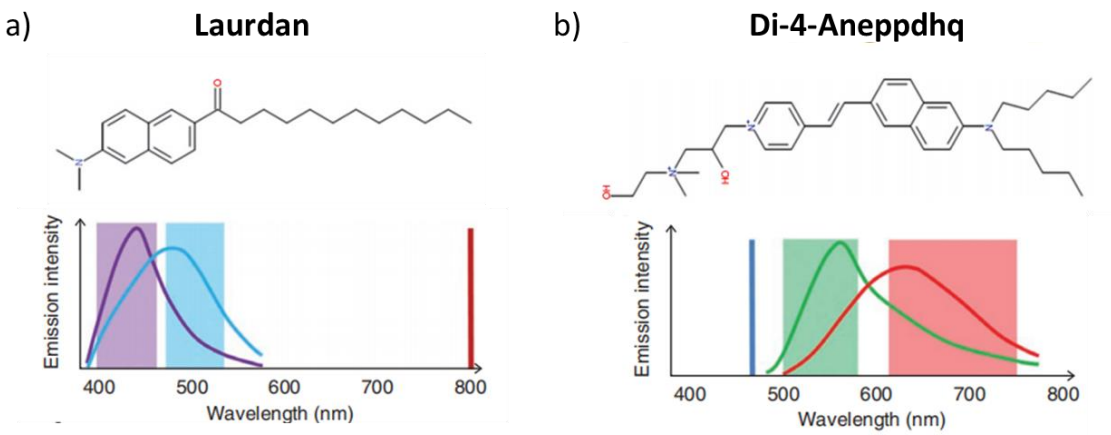

Figure 2.6. Schematic molecular structures and emission spectra in different lipid environments of (a) Laurdan and (b) Di-4-aneppdhq. The spectral ranges where spectral variation used to calculate GP is usually measured are highlighted with colored bands. The figure is adapted from original paper [143].

However, although these two dyes operate by the same mechanism, they report at different depths in the phospholipid bilayers: the fluorescent naphthalene moiety of Laurdan probes the interphase region between the lipid head groups and the first C-atoms of the hydrophobic acyl chains, whereas the chromophore of di-4-ANEPPDHQ aligns with the acyl groups deeper in the hydrophobic core [141]. Based on this, the complementary use of Laurdan and di-4-ANEPPDHQ can be advantageous to analyse, at different depths, how membrane order regulates protein interaction and/or insertion and to detect changes in bilayer's hydration induced by protein presence.

Differences in the lipid phase organization, surrounding the dyes, reflect in different lifetime values. When the lipids are in a disorder phase and the water molecules easily move into the bilayer, the lifetime of the dyes is characterized by shorter values than when the dyes are inserted in ordered lipid phase bilayers with less amount of water molecules inside. This is illustrated in Fig. 2.7 for Laurdan molecule; di-4-ANEPPDHQ has been shown to follow analogous behaviour. Detailed explanation of the interpretation of lifetime distribution position in the phasor plot will be given in Chapter 3- section 3.2.3.

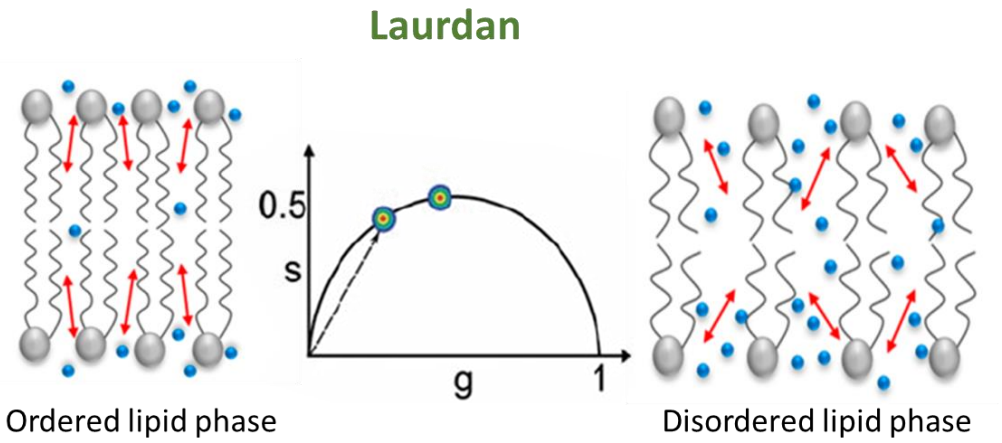

Figure 2.7. Schematic representations of membranes in ordered and disordered lipid phases. Red arrows represent Laurdan inserted in the membrane, and blue spheres represent the water molecules. The colored spots in the phasor plot represent the lifetime distribution of the dye in the different conditions. The figure is adapted from original paper [144].

In order to obtain information on membrane polarity, **Nile Red** (NR) was used in this thesis as lipid stain. It is an uncharged, hydrophobic dye that has been used for monitoring organization, fluctuation, and heterogeneity in membranes. Its absorption, fluorescence lifetime and fluorescence quantum yields depend on the solvent polarity [145]. It is characterised by negligible fluorescence when in water environment that significantly increases in apolar solvents or when the dye bounds to hydrophobic materials, such as phospholipid membranes. A more hydrophobic environment also induces a blue shift of the emission spectrum of the dye as well as an increase of its lifetime [146]. The phasor plot, showing how the fluorescence decay of NR shifts towards higher values decreasing solvents polarity, is reported in Fig. 2.8.

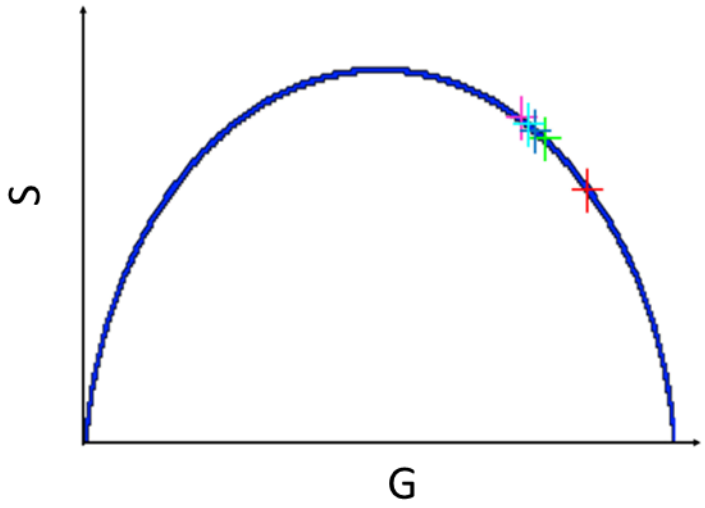

Figure 2.8. Phasor plot showing the lifetime distributions of NR in methanol (red), ethanol (green), propanol (blue), butanol (magenta), and hexanol (cyan). Figure and caption are adapted from the original paper[146].

2.9. UV-vis absorbance

Accurate determination of protein concentration is essential for quantitative biochemical, biophysical, molecular, and structural biology studies. The absorbance of ultraviolet-visible (UV-vis) radiations by intrinsic chromophores, is one commonly used method to measures samples concentration[147].

Monochromatic light is sent to a sample with an incident intensity (I_0). If a part of this light is absorbed by the sample, the intensity of the light output (I) will be lower and the absorbance can be expressed by

$$A = \log I_0/I \quad (10)$$

For each molecule, only those photons with a certain energy level can be absorbed as defined by the difference in energy between the orbital of the unexcited electron and a higher energy orbital. Particularly useful to calculate protein concentration is the absorbance at 280 nm (A_{280}), which offers high specificity, as it arises strictly from the rings of aromatic amino acids such as tryptophan (Trp), phenylalanine (Phe) and tyrosine (Tyr) residues, even if tryptophan is the main contributor. The correlation between absorbance and concentration is expressed by the Beer-Lambert law,

$$A = C\, d\, \varepsilon \quad (11)$$

where A is the absorbance, C the protein concentration (M), d the path length of the cuvette (cm^{-1}) and ε is the molar extinction coefficient ($M^{-1}cm^{-1}$).

2.10. Circular dichroism

Circular dichroism (CD) spectroscopy is an analytical technique used to analyse optically active (chiral) materials and measure the difference in the absorption of left and right circularly polarized light. In the far –UV, this technique presents a remarkable sensitivity to the backbone conformation of proteins [148,149]. At these wavelengths the chromophore is the peptide bond and the signal arises when it is located in a regular, folded environment.

As reported in Fig. 2.9 the alpha helix motif displays large CD bands with negative ellipticity at 222 and 208 nm, and positive ellipticity at 193 nm. Beta-sheets exhibit a broad negative band near 218

nm and a large positive band near 195 nm, while disordered extended chains have a weak broad positive CD ban near 217 nm and a large negative band near 200 nm. It can be considered that the spectrum of a protein is basically the sum of the spectra of its conformational elements. Based on this, CD spectroscopy is a powerful method in structural biology used to examine proteins, polypeptides, and peptide structures and to monitor any structural alterations that might result from changes in environmental conditions, such as pH, temperature and ionic strength and/or interaction with other molecules.

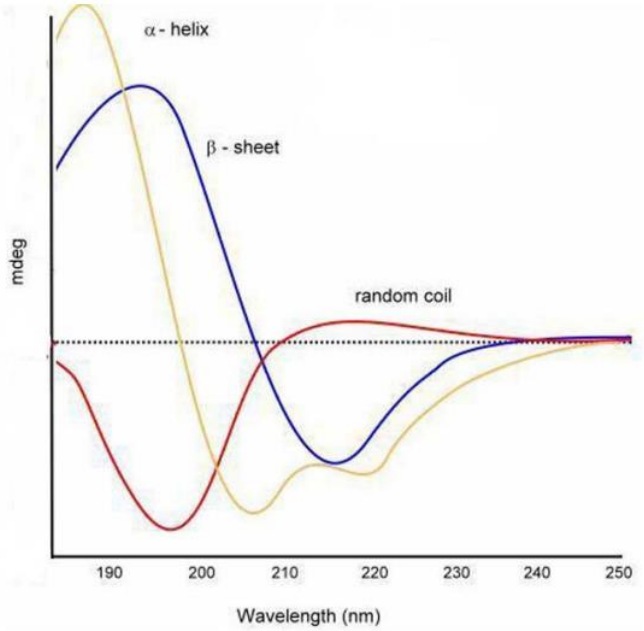

Figure 2.9. Different secondary structures of proteins by CD measurements. Figure taken by the original paper [150].

Chapter 3

Peptide-membrane interactions monitored by fluorescence lifetime imaging: a study case of Transportan 10

3.1. Introduction and purposes

In this section, the interaction between the amphipathic peptide Transportan 10 (TP10) with synthetic POPC-POPG giant vesicles (GVs) and giant plasma membrane vesicles (GPMVs) derived by HepG2 cells was explored by means time resolved quantitative fluorescence microscopy methods, described in previous sections.

TP10 is a 21 residues peptide that belongs to the family of the antimicrobial and cytolytic or cytotoxic amphipathic peptides. It contains a high proportion of positively charged amino acids (four lysines), no negative charges and the N-terminus that impart it a formal +5 charge at neutral pH (Fig. 3.1) [151].

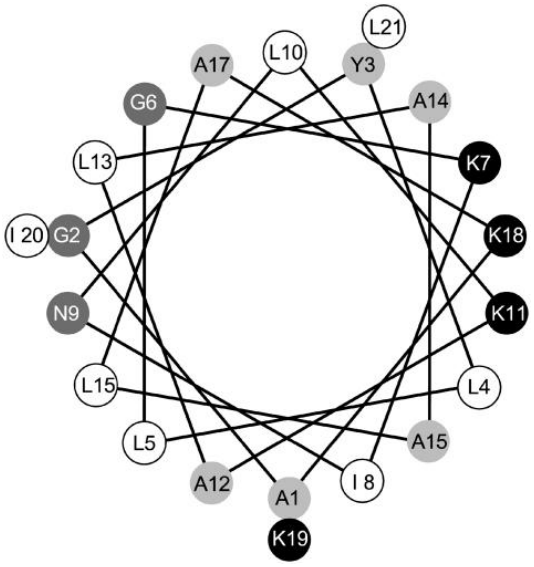

Figure 3.1. Helical wheel projection of Tp10 adapted from the original paper [151]. Black symbols represent positively charged residues, white, hydrophobic residues, dark gray, hydrophilic (uncharged), and light gray, residues with intermediate polarity. The C-terminus is amidated; therefore, it carries no charge.

In comparison with some of the most studied amphipathic α-helical antimicrobials, TP10 presents the largest charge. This high charge is a feature in common with the polycationic CPPs which makes it multifunctional [151]. Due to its potential applications TP10 was selected for this study.

TP10 is known to translocate, alone or together with molecular cargoes, across the plasma membrane of living cells improving the pharmacokinetics and the transport of drugs across biological barriers[152]. It was demonstrated that TP10 presents high pharmaceutical potential in vitro and *in vivo* as carriers for proteins (streptavidin, avidin) [153] but also nucleic acids, opening an intriguing perspective for gene delivery applications [154–156]. In addition, it was found that the ability of this peptide to translocate through cell membranes can be accompanied by toxic effects as result from membranes perturbation at high peptide concentrations. Various mechanisms of penetration and membrane modification by TP10, as well as other membrane active peptides, have been proposed to date including pore formation and transient membrane modifications[157], which also imply peptide conformational transitions[50]. In cells, penetration is believed to involve both endocytosis and direct translocation[158,159], as described above while *in vitro* in membrane models, TP10 is found to induce graded release of the contents of phospholipid large unilamellar vesicles with competing mechanisms often acting in parallel including toroidal, sinking raft and carpet models. Confocal fluorescence microscopy on negatively charged giant unilamellar vesicles, constituted by DOPC and DOPG as phospholipids, highlighted pore formation and translocation phenomena showing labeled peptide passage into the lumen.

Membrane composition [54,102,160], details of the specific environment and peptide concentration [159] define if and how TP10 translocates or modifies membranes as well as its potency.

Interestingly, TP10 showed cytotoxic effects towards carcer cells [152,153], not however causing any significant changes in the normal cell membranes [152]. This selectivity, due to the higher concentration of the anionic phospholipids phosphatidylserine (PS) and phosphatidylethanolamine (PE) exposed in the outer membrane of the former than in the latter, together with the overexpression of anionic glycoprotein and altered fluidity[161], makes the TP10 a good choice for the treatment of oncological patients [152,162].

Some studies have also demonstrated TP10 ability to interact with bacteria or model membranes that mimic the bacterial bilayer composition, thus revealing its antimicrobial activity. For example, the growth of intracellular fluorescence in *E. coli*, *B. subtilis*, *S. aureus* and *C. albicans* when incubated with fluorescein-labelled TP10, demonstrated peptide permeabilization with a consequential potent growth inhibition [163]. Its selectivity toward microbial cells was studied

evaluating the antibacterial activity of TP10 also in presence of human cell cultures. Results indicated that there is a concentration range within the TP10 can inhibit bacterial growth without damaging human cells; only a very high peptide concentration starts to inhibit mammalian cell growth inducing their death.

These specific properties certainly depend on structural characteristics of the peptide, on its local concentration at the membrane, and on tumoral and bacterial membranes composition. Bacterial and tumoral cell membranes share common features. These, pointed out as possible reasons of the selective of action of the peptide, include different membrane composition and fluidity, more negative charge, higher transmembrane potential than mammalian ones [164,165].

3.1.1. Tp10 action on POPC-POPG model membranes

In the first part of the work, the behaviour of TP10 peptide in presence of POPC:POPG model vesicles was evaluated. The zwitterionic phosphatidylcholine (POPC), commonly found in cell membranes, and the anionic phosphatidylglycerol (POPG) were chosen to mimic the negatively charged bacterial membranes [166]. As detailed in Chapter 1, since the membrane composition acts a crucial role in protein-membrane interactions and controls the membrane binding and insertion activity of protein molecules, the effect of the presence of cholesterol on lipid bilayer composition was evaluated. The rationale of this choice is based on the fact that it is well known that cholesterol, a constituent of eukaryotic membranes but rarely found in prokaryotic ones [87], stabilizing the phospholipid bilayers makes them more rigid, reduces the activity of AMPs.

Here, fluorescence spectroscopy was used coupled with confocal and multiphoton microscopy, to localize in real time and in a non-invasive mode the TP10 and to analyze the physical modifications induced by TP10 on POPC:POPG giant vesicles (GVs) with and without cholesterol. As reported in Chapter 1, GVs are here used as model systems because they possess similar physical properties to cell membranes and their size (around 10 µm diameter) allows the visualization of events occurring at the surface. These models have been already used to analyze both the fate of the peptide [159] and the modifications affecting the membranes [47,48], with sub-micron resolution.

To highlight membrane fluidity changes, the properties of two fluorescent membrane dyes were exploited: Laurdan and di-4-ANEPPDHQ. As described in Chapter 2, both dyes are sensitive to their lipid environment and their fluorescence emission spectra display a red shift when the environment changes between the liquid-ordered and disordered phases [142], this also being connected to shortening of fluorescence lifetime. Furthermore, these dyes can be used to sense physico-chemical

aspects of the membranes at different length scales within the bilayer as they occupy diverse locations being the di-4-ANEPPDHQ located in more internal parts [140,143]. These dyes are also characterized by different charges so they may interact differently with membrane environment due to electrostatics. Using fluorescence lifetime imaging microscopy (FLIM), it was possible to analyze events occurring at the membrane interface and within the membrane, in terms of both TP10 and lipid bilayer physical states. In addition, information on TP10 localization were gained by imaging Carboxyfluoscein fluorescence signal when covalently bound to TP10 (CF-TP10). Importantly by evaluating lifetime properties of this dye it was possible to distinguish peptide adhesion to the membrane from its insertion into the membrane

By combining multiple information, it was possible to reveal that TP10 adsorbs on the GVs surface and, at sufficiently high concentration, it inserts into the membrane, where two distinct lipid phases coexist. At first, TP10 induces modifications in the outer part of the membranes and then, depending on the balance between hydrophobic and electrostatic interactions, it propagates in the innermost regions experiencing environments with different structural organization and distinct fluidity. The peptide-membrane interaction has effects both on peptide, inducing a conformational change of TP10, and on lipid bilayers fluidity increasing their rigidity following dehydration. In addition, the reported results reveal that the insertion is a necessary but not sufficient condition for pore formation in membranes; only increasing peptide concentration over a threshold value, the formation of pores occurs. This was observed evaluating the permeation of the fluorescent dye $Alexa_{488}$ (700 Da) from the outside to the inside of membranes by means of confocal laser scanning microscopy.

3.1.2. Tp10 action on giant plasma membrane vesicles

The limited complexity in term of membrane and internal composition of lipidic and synthetic GVs, due to their lack of a cytoplasmic medium, create the needs of using different and more complex model membrane. For a closer natural cell-mimicking environment, membranes containing a large fraction of lipids and proteins and a cytoplasm medium inside vesicles are in fact essentials and for this reason GPMVs seemed a good choice. In recent work [117], GPMVs have also been made more complex by supplementing them with nanocompartiments serving as artificial organelles (i.e. enzymes encapsulated in polymersomes equipped with channel porines). This in order to mimic the architecture and complex functionality of eukaryotic cells, for example by studying at the same time but separately enzymatic reactions occurring in different co-encapsulated artificial organelles.

However, for the presented study that aims to study what happens to physical-chemical properties of membranes and the forces that drive the peptide-membrane interactions, the simplest model of GPMVs was chosen.

The second part of the study presents experiments aimed at clarify the action of TP10 on GPMVs derived from HepG2 cancer cells, simply by adding a special "vesicular buffer"[113] to cells that induces the formation of vesicles with the same membrane and cytosol environment as the donor cells (see Chapter 2 for details). In particular the use of model membranes from the human liver cancer cell line (HepG2) may provide useful information on the mechanisms underlying the possible antitumoral activity of this peptide. It is well known that in the last decade CPPs have demonstrated great potential in tumor therapy, because their conjugation with different cargos enhanced cellular uptake of cargo into cells [167,168]. However, previous works have also tested the direct anticancer activity of some CPPs and the TP10 cytotoxicity towards two tumor cell lines, in particular the erytroblastic leukemia and breast cancer ones, was demonstrated. Although the mechanism of the anticancer activity is not fully understood, perturbation of the membrane, which induces the formation of pores and the leakage of intracellular compounds (such as the lactate dehydrogenase), is involved [168,169].

Here, FLIM measurements were performed to evaluate changes in term of membranes' hydrophobicity and fluidity induced by TP10, by monitoring lifetimes changes of Nile Red and di-4-ANEPPDHQ, respectively. Nile red is a hydrophobic, fluorescent dye whose properties (absorption and fluorescence spectra, quantum yields and lifetime) depend on the polarity of the environment due to a large change in its dipole moment upon excitation [145]. Specifically, in water medium NR present vanishing fluorescence, while in organic solvent or in apolar environments it gives a strong fluorescence and an emission blue shift. Due to the remarkable sensitivity of the absorption and fluorescence properties of NR to the environment, it has been exploited in biophysical studies of local polarity in various micro heterogeneous environments including micelles, cyclodextrins and lipid membranes [146,170]. NR properties have been studied to analyze how membrane order and fluidity are influenced by lipid composition, chain saturation and the cholesterol but nothing was found about using this dye to monitor membrane changes such as a consequence of peptide interaction [171].

The information coming from Nile Red experiments were complemented with the ones on membrane fluidity resulting from di-4-ANEPPDHQ, which is used here to monitor changes of the

physical order of membranes.

Results indicate that initially TP10 interacts with GPMVs inducing an increase of membrane fluidity, which leads to an increase of the number of water molecules in the phospholipid bilayer and thus to loosely packed membranes (disordered membranes). It is known that the movement of water across the membrane is a natural biological process and the maintenance of water balance is critical for cell survival[172]; therefore, its alteration can lead, as a result of the variation of the osmotic pressure between inside and the outside of the lipid bilayer, to cell lysis.

This is associated with an increase in the polarity of the environment to which NR is exposed. Furthermore, over the time, these changes have led to the disintegration of almost all membranes.

3.2. Experimental results and discussion

Tp10 action on POPC-POPG model membranes

3.2.1. TP10 interaction with POPC:POPG and POPC:POPG:Chol model membranes studied by fluorescence spectroscopy and microscopy

Fig.3.2 reports LSCM measurements for exploring the interaction of TP10 peptide with POPC:POPG GVs whose composition was also enriched by the cholesterol presence in the bilayer. Representative 1024×1024-pixel images are shown of non-labelled POPC:POPG (in a ratio of 2:1) (Fig. 3.2 a) and POPC:POPG:Chol (in a ratio of 2:1:2) (Fig. 3.2 b) GVs after 20 h of incubation with CF-TP10 (1.3 μM).

The CF-TP10 signal is shown in green. As can be seen in Fig. 3.2 (a) green fluorescence is uniformly distributed and no co-localisation occurred between CF-TP10 and GVs containing cholesterol. The GV shape appears as black regions. A few bright micron-scale amorphous structures in these samples are identified as CF-TP10 peptide aggregates. An opposite behaviour is found in Fig. 3.2 (b) where a clear co-localisation between the measured green fluorescent signal and GVs is found indicating that TP10 accumulates at the membrane interface and that, in average, no significant changes in GVs shape and morphology is induced by this accumulation. Control measurements (not shown) were carried out via adding free CF to POPC:POPG vesicles to confirm that the dye alone do not localize at the membrane surface under the same experimental conditions.

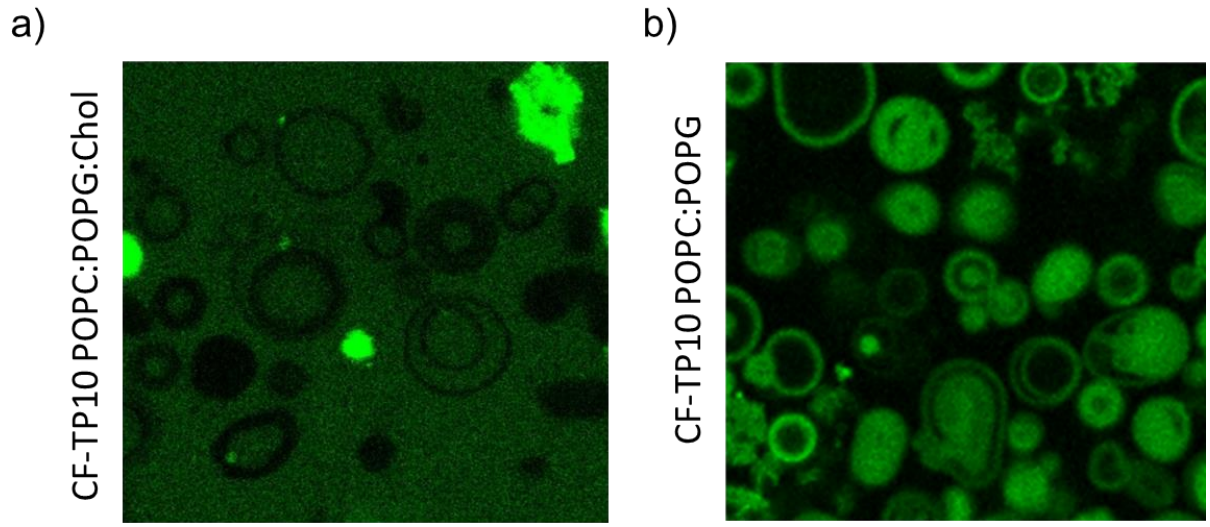

Figure 3.2. 1024×1024 pixels representative LSCM measurements of (a) POPC:POPG:Chol GVs and (b) POPC:POPG GVs after addition of 1.3 µM CF-TP10. The CF fluorescence intensity signal was collected under laser excitation at 470 nm in the range 500-600 nm. Measurements were acquired at equilibrium after 20 h of incubation. In panel (a), CF fluorescence is found to primarily be distributed in the solution and the GVs profiles are identified as dark areas with vanishing fluorescence indicating that no co-localisation exists between CF-TP10 and POPC:POPG membranes. A few brighter structures are identified as CF-TP10 aggregates. In panel (b), co-localisation between CF-TP10 and GV structures is clearly evident, indicating that CF-TP10 is located at the membrane.

To obtain further information on the possible interactions at molecular level between CF-TP10 and the model membranes, spectral bulk measurements on CF-TP10 fluorescence emission, added to GVs containing cholesterol or not, were carried out. As described in Chapter 2, the analysis of fluorescent emission spectra of extrinsic dyes, in this case of the CF covalently attached to peptide in the N-terminus, offers the possibility for peptide characterization. Changes in spectral intensity, shape, and position of the fluorescence spectra, due to relaxation phenomena, reflect modifications of environment surrounding the dye in terms of polarity, viscosity, hydration [118,133]. Changes of the spectra have also been described for fluorescent dyes conjugated with biomolecules, when they are associated with membranes or incorporated into cells [138]. Therefore, observed shift can be used to obtain a coarse description of the environment around the labelled peptide and to localize it. Fig. 3.3 reports normalised emission spectra of CF-TP10 (1.3 µM), acquired before and after CF-TP10 addition to (a) POPC:POPG:Chol and (b) POPC:POPG GVs. No significant changes in fluorescence emission spectra position are found for POPC:POPG:Chol samples (Fig. 3.3 (a)) whilst a significant blue shift of the emission maximum from about 530 nm (black line) to about 520 nm (pink line) is evident for POPC:POPG samples (Fig. 3.3 (b)). The observed shift occurs within the first 5 min after the addition of CF-TP10 to POPC:POPG GVs, then the signal remains stable for at least 24 h. These

spectroscopic data are in line with what found by the LSCM measurements, adding further information at the molecular level. In the presence of cholesterol, TP10 remains in the outer solution not interacting with the membranes, whilst in POPC:POPG GVs data indicate a clear change in the environment of CF-TP10, suggesting internalisation of the peptide into the membrane or close interaction with it.

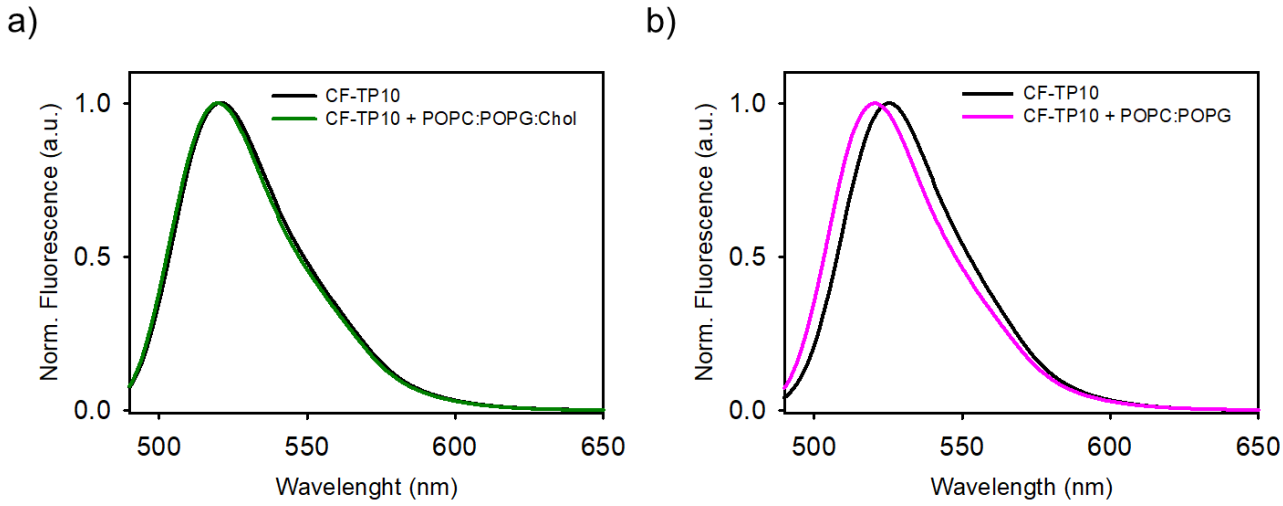

Figure 3.3. (a) CF-TP10 normalised fluorescence emission spectra (λ_{exc}=480 nm), acquired before (black line) and after 20 h (green line) from the addition of CF-TP10 to POPC:POPG:Chol. (b) CF-TP10 normalised fluorescence emission spectra (λ_{exc}= 480 nm), acquired before (black line) and after 20 h (pink line) from the addition of CF-TP10 to POPC:POPG GVs.

Bulk measures to explore variations in membrane phase properties occurring upon TP10 addition to the GVs samples were performed by monitoring Laurdan fluorescence spectra changes. As reported in Chapter 2, Laurdan is a gold standard dye used to monitor changes in membrane organization reporting membrane packing and fluidity [142,173]. The fluorescence signal of this molecule depends on the physical state of the phase and changes from liquid-ordered phase to liquid-disordered phase induce a shift of the Laurdan spectrum. The quantification of these spectral changes is usually obtained by calculating the generalized polarization (GP) which allows to distinguish the liquid (−0.3<GP<0.3) from the gel phase (GP>0.4) of the membranes [112]. In Fig. 3.4 the time evolution of the GP ratios, obtained from the analysis of Laurdan fluorescence spectra variations, measured after the addition of TP10 to POPC:POPG (pink circles) and POPC:POPG:Chol (green circles) GVs, are reported.

Results show that the GP value measured for POPC:POPG:Chol GVs is, as expected and in line with literature values, higher than the one measured for samples in the absence of cholesterol, indicating

a higher rigidity and compactness of the membrane [174,175]. It is not surprising to find that this value remains constant after TP10 addition to cholesterol-containing membranes, that no TP10-membrane interactions occur confirming what previously observed in Fig. 3.2 (a) and 3.3 (a). Analogous results were previously obtained for TP10 and other CPPs and were attributed to the suppression of thermal fluctuations of the membranes and to the presence of rigid lipid-phases induced by the cholesterol presence. Indeed, as previously suggested, phospholipids above their gel liquid phase (-2,15 °C and 0,85 °C for POPC and POPG, respectively) interact with cholesterol increasing their orientation order and rigidity. Cholesterol presence may also modify the hydrophobic matching between membrane and peptides, having consequences on their interaction with the lipid bilayer. On the other hand, Laurdan GP in POPC:POPG samples before the addition of TP10 indicates that the membrane is in its liquid phase and results more accessible to the solvent [142]. After the addition of TP10, the GP value rapidly increased, i.e. within the first 5 min. This small but significant change towards a higher GP value can be interpreted as an indication of a progressive change in membrane fluidity towards a more ordered phase. Similarly, to what was observed in previous studies [47,48,112], it is possible to infer that under the tested conditions TP10 not only accumulates at the surface, but also inserts into the membrane causing dehydration and stiffening of the lipid bilayers. This is also in line with the results presented in Fig. 3.3 (b).

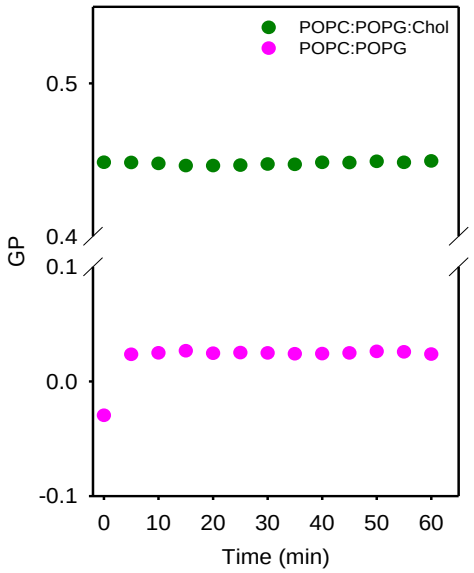

Figure 3.4. Time evolution of GP ratios, obtained from the analysis of Laurdan fluorescence spectrum variations, due to the addition of CF-TP10 to POPC:POPG (pink circles) and POPC:POPG:Chol (green circles) GVs. Laurdan fluorescence emission spectra were acquired in the range 370-650 nm as a function of time every 5 min. Excitation wavelength was λ_{exc}= 380 nm and excitation and emission bandwidth were 5 nm. The cuvette was gently shaken prior to all measurements to keep the sample uniformly dispersed. These

measurements reveal that the interaction between CF-TP10 and GVs occurs only in membranes where cholesterol is not present.

It is worth nothing that the observed TP10 effects do not induce membrane changes in morphology or disruption phenomena. This being in line with a previous study where TP10 action on GUVs was evaluated [159] and where TP10 was found to translocate trough the single bilayer. Furthermore, by monitoring the gradual loss of AF647 fluorescent dye from GUVs, the peptide was found to form pores in membranes in a concentration-dependent manner.

Under the present conditions, after the immediate peptide/membrane interactions, the system remains stable for several hours and no translocation of the peptide is evident. This is not surprising due to the differences in the experimental setup and in the membrane model systems both in terms of lipid composition and lipid organisation [54]. Electrostatic interactions between TP10 positive charges and the anionic head groups of the POPC:POPG lipids vesicles may produce peptide anchoring on the surface[54,176]. However, TP10 was suggested to induce bilayer perturbation by causing mass imbalance after adhesion to the outer part of the membrane and/or via a closer interaction possibly resulting in changes in membrane rigidity. Its aggregation at the membrane may also occur, as previously reported for others CPPs for which the action was linked to aggregation. The evidence that TP10 only interacts with cholesterol-free membranes is an important finding for selective targeting of CPPs to bacterial membranes over eukaryotic ones.

3.2.2. FLIM analysis on CF-TP10 fluorescence lifetime to distinguish peptide adsorption from insertion into the membrane

To further explore the occurring interactions between TP10 and negatively charged membranes in the lipid disordered phase, FLIM measurements were performed. To better highlight the changes of physical properties of vesicles membranes and understand the mechanisms of action of the peptide, we explored two different concentration regimes during the time adding TP10 to the membrane at a 300 nM concentration (500:1 lipid:protein ratio) and at 1.3 µM concentration (115:1 lipid:protein ratio) where significant effects are observed. TP10 was previously found to penetrate GVs in a concentration dependent manner[177] so that by changing concentration regime, we explored two largely different conditions where the equilibrium between monomers and possible aggregates was critically shifted toward the aggregated state at higher concentration. Diffusion driven interaction was obviously altered and internalisation into the membrane possibly favoured at higher concentration.

In Fig. 3.5., FLIM results on unstained POPC:POPG GVs acquired 1 h and 20 h after the addition of CF-TP10 peptide at 300 nM and 1.3 µM final concentrations are reported. These experiments arise from the observations reported in Fig. 2 (b) that reveals CF fluorescence signal sensitivity to TP10 internalisation. FLIM measurements were analysed by means of the phasor approach [125]. FLIM calibration of the system was performed by measuring the known lifetime of the fluorescein that is a single exponential of 4.0 ns [178]. As reported in detail in Chapter 2, this fitting-free analysis provides a global view of fluorescence molecules decays at each pixel in the images: each pixel of the intensity images is mapped in a point in the phasor plot corresponding to the measured fluorescence lifetime. This gives the possibility to localize using coloured cursors specific pixel clouds in the phasor plot and identify the corresponding pixels in the image [125].

Fig. 3.5 shows representative 256×256-pixels intensity images of (a and g) 1.3 µM CF-TP10 in solution after 1 h and 20 h respectively, and POPC:POPG GVs samples 1 h and 20 h after the addition of (b and h) 300 nM and (c and i) 1.3 µM CF-TP10. The phasor plot, corresponding to these measurements and reported in panel (o) presents two main distinguishable lifetime distributions lying on the universal circle, indicating that CF fluorescence decays can be described as single lifetime decays. By selecting lifetime these distributions using two circular cursors (cyan τ_i=3.7 ns, pink τ_f=3.2 ns), the corresponding pixels are mapped back in the images according to the same colours. In particular, the lifetime maps reported in panels (d-f) and (l-n) refer to measures acquired after 1 h and 20 h, respectively. A few pixels with shorter lifetime distribution are also observed and selected using a red cursor. Measurements on TP10 in solution after 1 h, reported in panel (a) and (d), reveal, as expected, a uniform intensity and lifetime distribution, all pixels in panel (d) present a lifetime distribution centred at about 3.7 ns [179]. Data shown in panel (g) and (l) reveal that system is stable also after 20 h. The intensity maps in Fig. 3.5 (b) and (h), where CF-TP10 was added to GVs at lower concentration, if compared to the intensity maps in Fig. 3.5 (c) and (i), when higher peptide concentration was added to GVs, show that in each sample CF fluorescence was not evenly distributed, but that, in average, the samples with higher concentration of TP10 presented higher intensity. Fig. 3.5 (e) and (m) reveal that the measured fluorescence lifetimes of CF, added to GVs at lower concentration, are different over a single structure indicating that the dye is experiencing different environments. Pixels exist with lifetime comparable to the one measured on the sole peptide in solution (cyan), other pixels are characterised by a fluorescence signal with lower lifetime distributions (pink). The observed decrease in lifetime may be ascribed to water molecule depletion from the environment of the dye or other mechanisms, which increase non-radiative decay

processes, e.g. the aggregation of the dye bringing to self–quenching mechanisms or the closer lipid membrane interaction of the dye due to the insertion of the peptide in the membrane [118,179]. In particular, in samples at 300 nM both after 1 h (Fig. 3.5 (e)) and 20 h (Fig. 3.5 (m)), results indicate that CF-TP10 mainly interacted with aqueous phases (cyan), without closely interacting with the membrane, and only few pixels present reduced lifetime (pink). Measurements obtained at higher concentration (1.3 µM) after 1 h and 20 h (Fig. 3.5 (f) and (n)) reveal that although the GVs maintain their regular morphology almost all pixels are coloured in pink indicating a dense packing of CF-TP10 and/ or a higher interaction with membranes. These data also reveal that changes observed after 1h do not present significant modifications if repeated after 20 h: once changes occurred, the sample remains stable at least for 20 h. A few pixels highlighted by the red cursor in the phasor plot correspond to amorphous structures that we identify as large peptide aggregates.

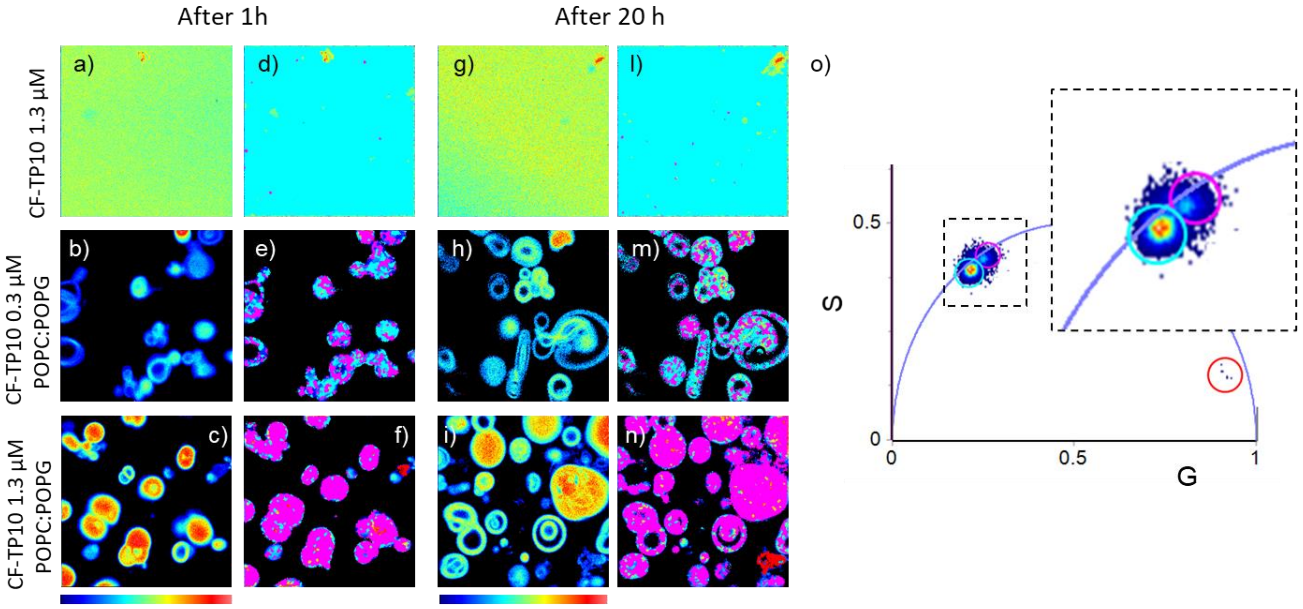

Figure 3.5. Phasor analysis of FLIM measurements on CF-labeled TP10. The signal was acquired under laser excitation at 470 nm and collected in the range 500-650 nm. Intensity maps of (a and g) 1.3 µM CF-TP10 solution in phosphate buffer 20 mM pH 7, POPC:POPG GVs added of (b and h) 300 nM and (c and i) 1.3 µM CF-TP10, acquired after 1h and 20h. (d-f) and (l-n) Lifetime maps corresponding to (a-c) and (g-i) measurements respectively, coloured according to the colour code obtained from the phasor plot (o). Clusters of pixels corresponding to different lifetime distribution were identified in the phasor plot and highlighted by coloured circular cursors: these pixels are mapped in images (d-f) and (l-n) with corresponding colours. The choice of the size and the position of the circles is arbitrary. A magnification of the region highlighting area of interest is reported in the dashed lines surrounded inset.

3.2.3. Insertion of TP10 affects membrane properties: FLIM analysis of membrane sensitive dyes

Taking into account previous data, it is possible to infer that TP10 at high concentration is inserted in the membrane layers. With the aim of focusing on membrane structure changes, fluorescence spectroscopy and FLIM experiments on two similar dyes, Laurdan and di-4-ANEPPDHQ, used to label POPC:POPG vesicles, were performed[140,141,143].

Both dyes are reported to sense membranes trough analogous mechanisms related to water molecules accessibility of the lipid bilayer. Importantly for our purposes, these dyes are known to locate at different depths in the membrane as di-4-ANEPPDHQ is sensitive to deeper regions in the hydrophobic core[141].

Fluorescence bulk spectroscopy experiments were performed on Laurdan dye whose analysis is shown in Fig. 3.6. This reports GP variations as a function of time that as reported above reflect variations of membrane order/ packaging correlated to the accessibility of membrane to water molecules and to the dipolar relaxation of these molecules at the membrane interphase[142]. Fig. 3.6 compares the already observed effects measured after adding 1.3 µM TP10 (Fig. 3.4) to analogous measurements obtained at 300 nM concentration. Data reveal that a decrease in the fluidity of the membrane occurs within 5 min and that the changes are critically larger at higher peptide concentration.

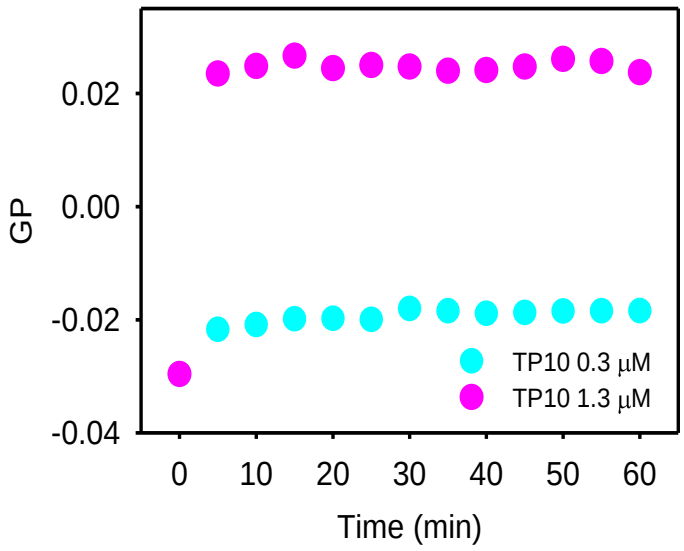

Figure 3.6. Time evolution of GP ratios obtained from the analysis of Laurdan fluorescence spectrum variations, measured in bulk, after the addition of TP10 300 nM (cyan circles) and TP10 1.3 µM (pink circles).

Fig. 3.7 and 3.8 show the phasor analysis of FLIM measurements on Laurdan-stained POPC:POPC GVs acquired in the so called blue channel (410-460 nm) and green channel (480-540 nm),

respectively. By collecting the signal separately in the two channels, it is possible to discriminate the effect of TP10 on the membrane polarity (fluidity, blue channel) and dipolar relaxation (hydration, green channel)[180]. Dipolar relaxation (DR) refers to the capability of polar solvent molecules in the proximity of the dye to reorient[180,181].

In Fig. 3.7 (a-c) and (g-i) 256×256 fluorescence intensity images of the analysed samples are reported. Specifically, in panel (a and g), the signals of GVs before the addition of TP10 are reported together with images acquired after 1 h (b and c) and after 20 h (h and i) from the addition of the peptide at 300 nM (b and h) and 1.3 μM (c and i). Finally, in panels (d-f) and (l-n) are reported the corresponding phasor maps obtained from the same measurements in which each pixel is coloured according to the corresponding selection in the phasor plot (Fig. 3.7 (o)). In the phasor plot the superimposition of the analysis of all measurements is reported. The phasor analysis of Laurdan fluorescence lifetime was previously used to separate ordered and disordered phases both in synthetic and in cellular membranes and importantly to evaluate different properties and changes in the membrane structure distinguishing polarity changes and dipolar relaxation allowing pixel by pixel understanding of these two parameters in the membrane.

Two lifetime distributions are evident, the first selected by the cyan cursor is outside the universal circle, which corresponds to pixels (cyan) localized at the membrane in the sample where TP10 is not present and at low TP10 concentration. The other lifetime distribution lies on the universal circle and is highlighted with pink cursor and only corresponds to pink pixels in the sample where the higher concentration of TP10 is added. Fluorescence lifetime distributions of Laurdan outside the universal circle can be rationalised considering conditions wherein an excited-state reaction occurs, as for example, fast interconversion processes between Laurdan molecules experiencing highly dynamic heterogeneous environment[180].

In the sample at 300 nM no significant changes occurred for lifetime measured in this channel with respect to the one measured for untreated samples. Interestingly, the lifetime distribution of Laurdan in GVs after the addition of the peptide at 1.3 μM shifts to a position on the universal circle (s coordinate remains constant, while g coordinate is reduced). In line with what reported in a recent work by L. Malacrida et E. Gratton[180], it is possible to ascribe these changes to a reduction of membrane fluidity and the final position of the lifetime distribution, single exponential (lifetime 2.7 ns) indicates homogeneous lipid environment with coexisting lipid phases. Also, in this case it is

important to underline that the measurements acquired after 1 h or 20 h do not present significant changes.

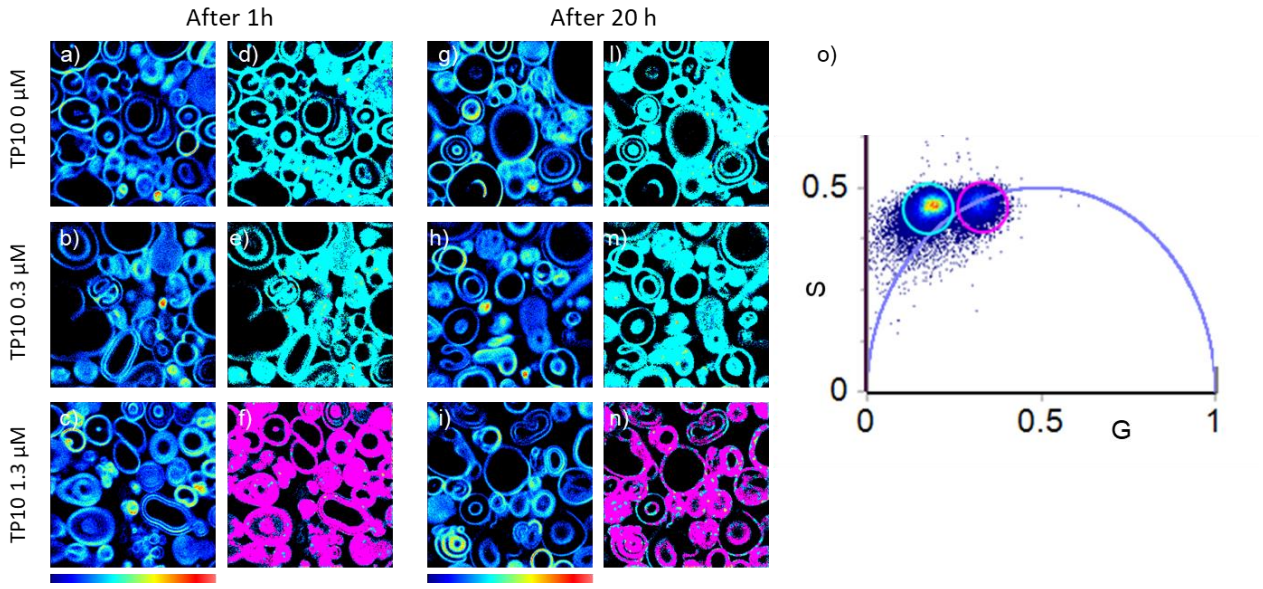

Figure 3.7. Phasor analysis of 256 × 256 pixel FLIM measurements on Laurdan in POPC:POPC GVs in the range 410-460 nm, λ_{exc}= 780nm. Fluorescence intensity images on Laurdan before (a and g) and after 1 h (b and c) and 20 h (h and i) from the addition of TP10 300 nM (a and h) and 1.3 µM (c and i). (e-f) and (h-n) Phasor color maps in which each pixel is colored according to the color of the corresponding cursor in the phasor plot (o). The choice of the size and the position of the cursor is arbitrary.

In Fig. 3.8 (a-c) 256×256 fluorescence intensity images acquired in the green channel of POPC:POPG GVs labelled with Laurdan (a) before and after 1 h from the addition of (b) 300 nM and (c) 1.3 µM TP10 are reported. In panel (d-f) the corresponding intensity maps are reported in which each pixel is colored according to the color of the cursor in the phasor plot (Fig.3.8 (o)). As shown for measurements acquired in the blue channel, only at high peptide concentration it is possible to highlight a difference in Laurdan lifetime and in particular a movement from the outside (green cursor) to the inside (red cursor) of the universal circle. This can be ascribed to a decrease of the membrane hydration levels accompanied by a decrease of DR mechanisms possibly due to lipid compaction. Analogous measurements acquired after 20 h (not reported) did not revealed significant changes.

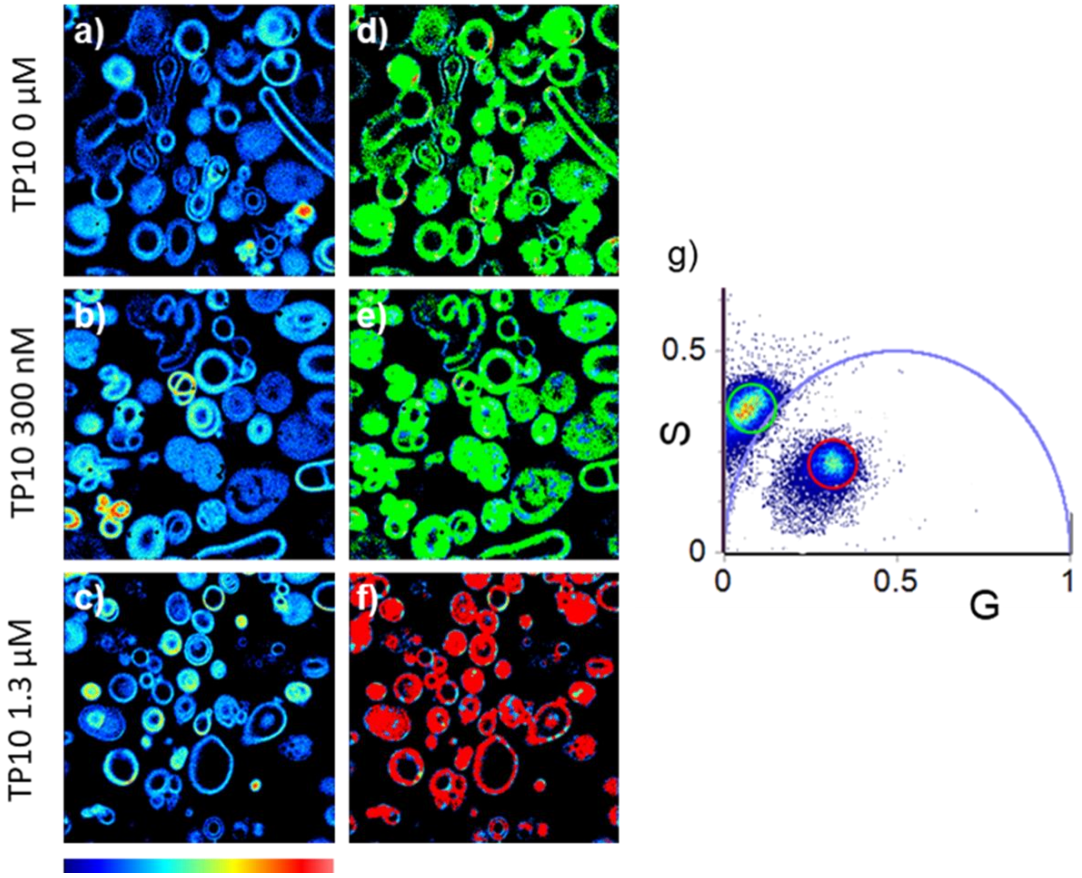

Figure 3.8. Phasor analysis of 256 × 256 pixel FLIM measurements on Laurdan in POPC:POPC GVs in the range 480-540nm, λ_{exc}= 780nm. Fluorescence intensity images on Laurdan before (a) and after 1 h from the addition of TP10 300 nM (b) and 1.3 µM (c). (g) Phasor plot obtained from measurements (a-c). (d-f) Phasor color maps in which each pixel is colored according to the color of the corresponding cursor in the phasor plot. The choice of the size and the position of the cursor is arbitrary.

We next performed FLIM experiments on the same samples using di-4-ANEPPDHQ with the aim to analyse changes in the inner part of the membranes. di-4-ANEPPDHQ, being aligned with the acyl groups, is in fact located in a more internal and hydrophobic region with respect to Laurdan molecule [141]. Moreover, this dye contains in its structures two positive charges, which in the present model systems contribute to the reduction of the mobility of the dye within the bilayer [141].

In Fig. 3.9 (a-c) and (h-l) we present 256×256 pixels of di-4-ANEPPDHQ fluorescence intensity maps in GVs before and after 1 h (a-c) and 20 h (h-l) from TP10 addition at 300 nM and 1.3 µM concentrations. Differently from what observed before, changes on a longer time scale, in the signal reporting for membrane changes under the conditions where TP10 is inserted into the membrane (at 1.3 µM concentration), are found. In this case, measurements acquired 1 h after the addition of the peptide do not superimpose with the ones acquired under stable conditions after incubation for 20 h, indicating that, membrane reorganisation, following TP10 addition in the presence of this dye,

requires longer time. In line with previous results, as shown from the intensity images, no significant changes were found in relation to the GVs size and shape. In Fig. 3.9 (d) and (m) phasors lie inside the universal circle indicating that di-4-ANEPPDHQ lifetimes, in these conditions, are characterised by non-single exponential decays [125]. Measurements acquired after 1 h (Fig. 3.9 a-g) show a quite broad lifetime distribution reflecting the loosely packed membrane in the fluid phase. No significant changes are observed in samples where peptide was added at the lower concentration while a tiny broadening of the distribution toward higher lifetimes is observed in the sample at higher concentration. To visualise that, we used three arbitrary adjacent cursors centred on the straight line, coloured in yellow, green and pink. As can be seen, only in the sample at higher concentration few pink pixels are revealed at the membrane, indicating that characteristic lifetime of the dye is slightly higher in this region. Characteristic lifetimes vary from shorter (yellow) to longer (pink) as the observed distribution moves counter-clockwise in the universal circle. Membrane changes toward less fluid state. The same graphical representation is used for phasor analysis of samples incubated with the peptide after 20 h (Fig. 3.9 m-p). The phasor plot seems to reveal a broader distribution (two main maxima are identified). This visualization in three colours at the late stages of incubation shows that the sample, after the addition of 300 nM TP10, is mostly characterised by fluorescence lifetimes selected by the green cursor (green pixels), a reduced number of yellow pixels with respect to the control sample and few pink pixels which are characteristic of higher lifetimes are also present. At the higher concentration, lifetime distribution is shifted toward higher lifetimes, so that almost all GVs are selected using the pink cursor, which singles out pixels with more rigid membranes.

The observed results suggest that at lower TP10 concentration the interaction is mostly at the membrane surface and induces small changes in di-4-ANEPPDHQ environment. When TP10 was added at the high concentration, the peptide inserted deeper into the membrane layer inducing dehydration and stiffening with consequent increase of di-4-ANEPPDHQ lifetime and membrane reorganisation. This requires longer time with respect to changes occurring closer to the water membrane interface monitored by Laurdan.

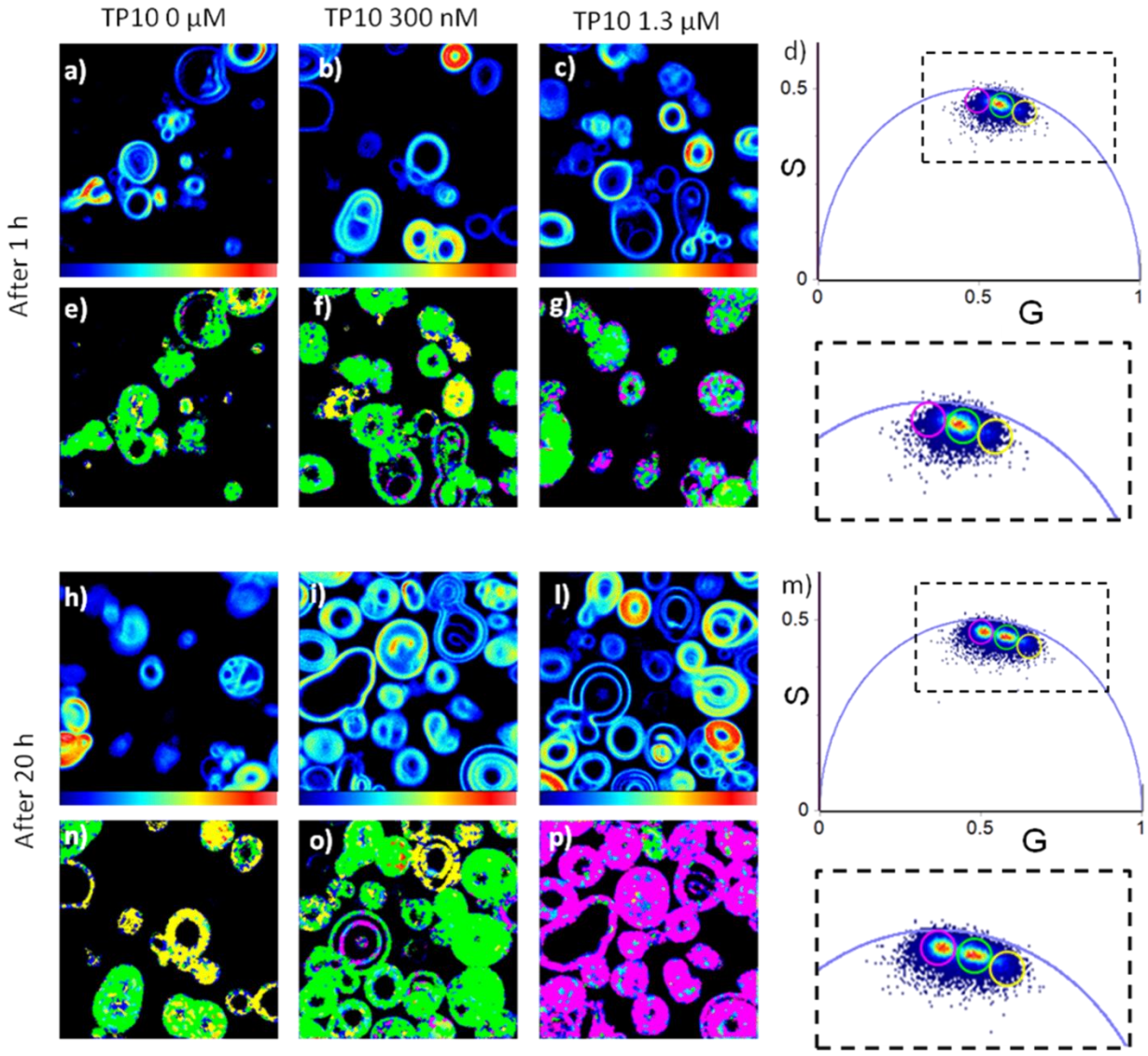

Figure 3.9. Phasor analysis of 256 × 256 pixel FLIM measurements on Di-4-ANEPPDHQ in POPC:POPC GVs after 1 h (a-g) and after 20 h (h-p). Fluorescence intensity images on DI-4-ANEPPDHQ before (a-h) and after 1h (b), (c) and 20h (i),(l) from the addition of TP10 300 nM (b-i) and 1.3 µM (c-l). (d) and (m). Phasor plot obtained from measurements (a-c) and (h-l) respectively, where fluorescence lifetime distributions are highlighted using coloured cursors. The magnifications of the regions highlighting area of interests are reported in the dashed lines surrounded inset. (e-g) and (n-p). Phasor colour maps in which each pixel is coloured according to the colour of the corresponding cursor in the phasor plots. The choice of the size and the position of the cursor is arbitrary.

In Fig. 3.10 the quantitative analysis of data in Fig. 3.9 is reported. Indeed, looking at the phasor plots it is possible to draw a straight line where the lifetime distributions lie on (Fig. 3.9 d and m) connecting two single exponential lifetimes of respectively τ= 2.5 ns and τ=1.1 ns. This FLIM analysis is based on the decomposition of the phasor plot data using these two principal lifetime components identified via the intersection of the straight line, passing through the lifetime distributions cloud. Following this model, it would be possible to infer that the membrane is characterised by two

distinct lipid phases [182], and not a homogenous phase of intermediate order. The equilibria between these phase changes following peptide insertion at different level in the bilayer. In Fig. 3.10 we then show the phasor plot where principal components of the decays are highlighted τ_1=1.1 ns (blue cursor) and τ_2=2.5 ns (red cursor) corresponding to less fluid and more fluid phase respectively [182]. Using two components model:

$$I(t) = F_1 e^{-t/\tau_1} + F_2 e^{-t/\tau_2}$$

The distance between each point of the cloud in the phasor plot and the single exponential phasor represents the fraction of each component [33]. In Fig. 3.10 (b-d) analysis of the data acquired 1 h after the addition of TP10 is reported and in Fig. 3.10 (f-h) analogous results obtained after the samples have reached the equilibrium at 20 h of incubation. Images are coloured in false colours according to the F fraction of the τ component. The scale goes from blue (pure fast component at τ_1=1.1 ns) to red (pure slow component at τ_2=2.5 ns). This scale can be taken in account as a fluidity scale going from less fluid to more rigid membrane configurations.

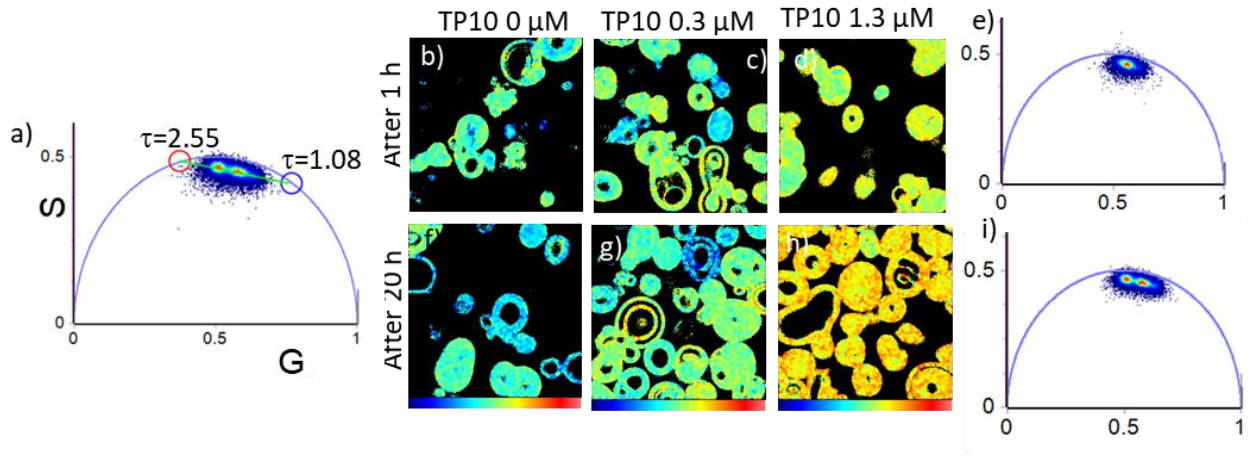

Figure 3.10. Phasor analysis of 256 × 256 pixel FLIM measurements on di-4-ANEPPDHQ. (a) Phasor plot from the analysis of the FLIM images acquired after 20h from the addition of TP10 to POPC:POPG labelled with di-4-ANEPPDHQ. The two principal lifetime components, used for the quantitative analysis, are represented by blue and red cursors. Lifetime principal components are τ_1 = 1.1 ns (blue) and τ_2 = 2.5 (red). (b-d) Lifetime fraction maps for the FLIM images on di-4-ANEPPDHQ before (b) and after 1h from the addition of TP10 300 nM (c) and 1.3 µM (d). (f-h) Lifetime fraction maps for the FLIM images on di-4-ANEPPDHQ before (f) and after 20 h from the addition of TP10 300 nM (g) and 1.3 µM (h). (e) and (i) Phasor plots from the GVs after 1h (e) and 20 h (i) from TP10 addition.

An increase of di-4-ANEPPDHQ lifetime occurs after the addition of TP10 to POPC:POPG GVs and this change depends on peptide concentration and on the incubation time. The fastest decay is

dominant in GVs before the peptide addition and when TP10 was added in a concentration of 300 nM (F_1 = 0.44).The average fraction F_1 decreases increasing the concentration of the added peptide (1.3 μM) being reduced from F_1 = 0.38 (after 1 h) to F_1 = 0.29 (after 20 h). These results suggest that the interactions between membrane and peptide, when the latter is a high concentration, occur not only at membrane surface but also in the inner part of membrane inducing further reorganisation, which result in increased rigidity. Electrostatic interactions with POPG charged heads could favour the hold back the peptides at the surface, while hydrophobic interactions may tend to drive the peptides into the hydrophobic core of the bilayer. In particular, in the phasor plot relative to the data obtained for di-4-ANEPPDHQ lifetime at late stage of incubation two main distributions are clearly evident. In this context, it is possible to infer that the dye experiences two main different environments in terms of membrane fluidity that is induced by TP10 accumulation at the membrane surface with following penetration in the inner parts.

3.2.4. POPC:POPG membranes induce conformational changes of inserted TP10

Structural properties and the secondary structure of CPPs have recently been reported to control to a certain extent their cellular uptake mechanism and to be associated with a specific route of entry. In particular, some works have demonstrated that secondary structures formation influences the translocation process of peptides within the phospholipid bilayer. For this reason, to evaluate whether conformational changes involve TP10 during its insertion into POPC:POPG model membranes CD measurements were carried out [49,183]. CD signal reflects peptide backbone organization and it is widely used to analyze protein secondary structures (see Chapter 2). Fig. 3.11 shows the far-UV CD spectra of TP10 1.3 μM in phosphate buffer solution pH 7 in the presence and in the absence of POPC:POPG GVs.

As can be seen the CD spectrum of this peptide in its free form, in line with the spectra found in literature, is characterized by a minimum centred at 202 nm revealing that TP10 secondary structure is mainly random coil. In the presence of POPC:POPG, TP10 spectrum presents two minima, the first at about 208 nm and the second at about 225 nm. Spectral changes occur immediately after the addition of the vesicles into the peptide solution and can be ascribed to a conversion of the peptide secondary structure from a flexible random coil structure to α-helical structure, which is typically found when short peptides or disordered proteins interact with lipid membrane [184]. These results are in line with previous work [183]performed on CPPs, included TP10, in presence of similar membranes, constituted by DOPG and DOPC as lipids, where the conformational changes of the

peptides toward α-helix structures occurred after peptide penetration into the bilayers. Furthermore, the peptide-membrane interactions have been shown to perturb the stability of the membranes by inducing the release of dyes from pre-loaded vesicles.

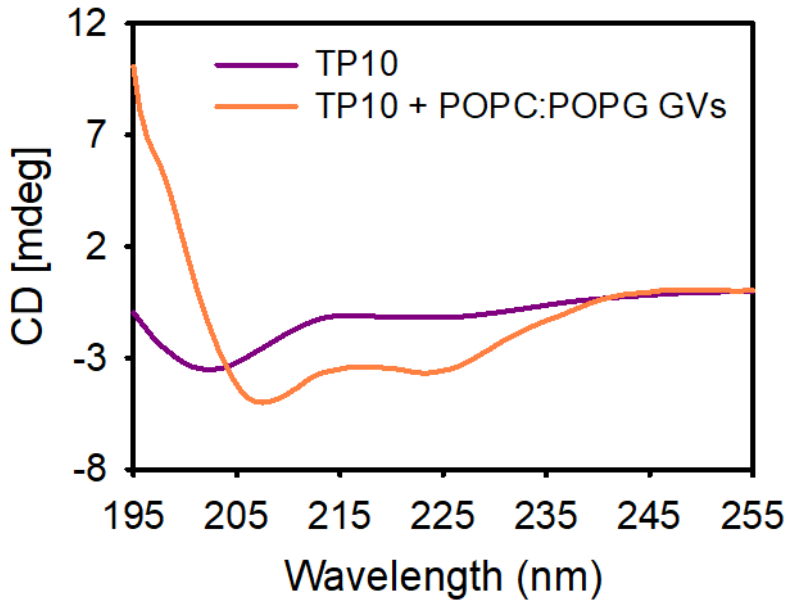

Figure 3.11. Far-UV (195-255 nm) CD spectra of 1.3 μM TP10 in 20 mM phosphate buffer pH 7 (violet line) and in presence of POPC:POPG GVs (orange line), dispersed in the same buffer pH 7. A change from random coil to α-helix structures is observed when TP10 interacts with lipid vesicles.

3.2.5. High TP10 concentrations induce pores formation in the membranes

Based on above data, which revealed TP10 insertion in membranes at 1.3 μM concentration, and based on previous results in licterature[108,159,185] that have demonstrated the ability of some CCPs to form pores in the membrane, the translocation of the fluorescent probe $Alexa_{488}$, from the outside to the inside of POPC:POPG GVs in presence of TP10 was evaluated by means of LSCM measurements.

$Alexa_{488}$ is a small fluorescent molecule with average diameter below 1 nm, which can be used to evaluate the solvent accessibility of diverse structures at the nanoscale[186,187].

Fig. 3.12 presents representative 1024×1024-pixel images of non-labelled POPC:POPG GVs, incubated for 1 h with (a-b) 1.3 μM and (c-d) 10 μM TP10 and after this time added of $Alexa_{488}$ (7 μM). The $Alexa_{488}$ signal is shown in cyan. Fig. 3.12 (a) shows that at the 1.3 μM peptide concentration, the cyan signal is primarily distributed in the solution and the vesicles profiles are visible as dark areas. This indicates that Alexa does not access the inner parts of the vesicles,

suggesting that TP10 does not induce the formation of pores in the membranes or that it forms pores with smaller sizes than the one that will allow $Alexa_{488}$ penetrate inside the membrane. In line with suggestion from literature [152] and as a further control, the experiment was performed at higher peptide concentration (10 μM). In these conditions as evident in panel (c) the cyan signal is almost homogeneously dispersed and the vesicles are clearly visible only through transmission channel (Fig. 3.12 (d)). The increased concentration of the peptide then induces the permeation of $Alexa_{488}$ inside the vesicles. The diffusion of $Alexa_{488}$ occurs without local disruption, rupture of the GVs, changes in the local curvature of the membrane, membrane fusion and vesicle fission, indicating that TP10 forms pores in the membrane through which the membrane permeation of the dye occurs [109].
In addition, data suggest that the insertion of TP10 is a necessary, but not a sufficient condition, for pore formation: only when peptide exceeds a threshold concentration, the TP10 molecules are enough to form pores.

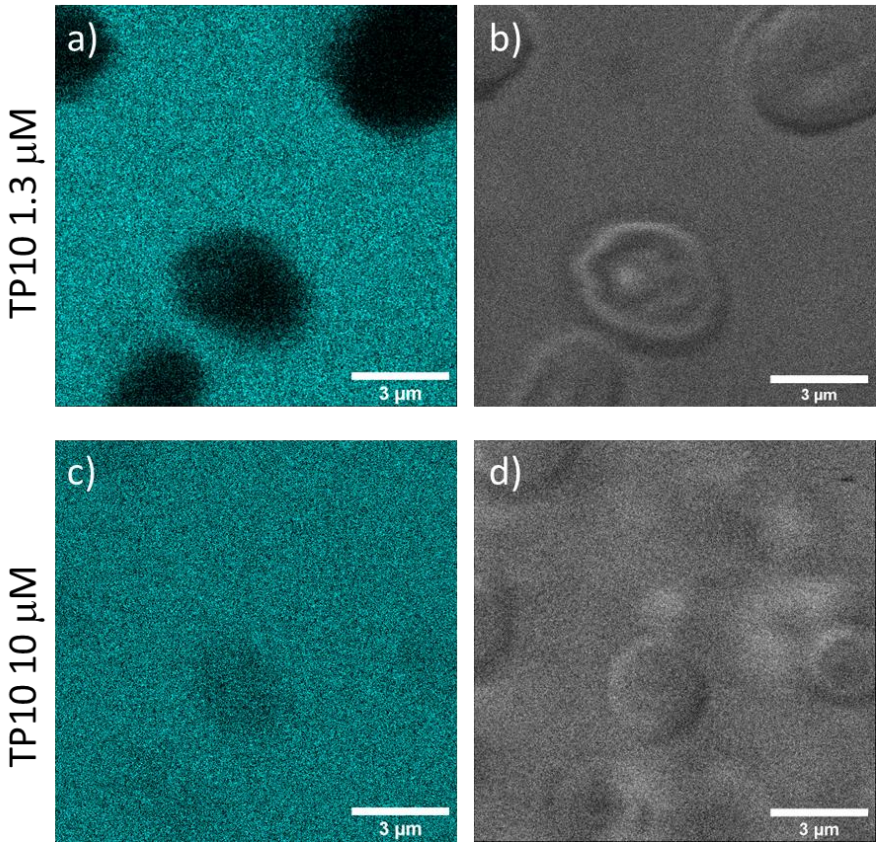

Figure 3.12. 1024×1024 pixels representative LSCM measurements of POPC:POPG GVs, incubated for 1 h with (a-b) 1.3 μM and (c-d) 10 μM TP10 and then added with $Alexa_{488}$ (7 μM). Measurements were acquired after 1 h from the addition of the fluorescent dye. The $Alexa_{488}$ fluorescence intensity signal was collected under laser excitation at 488 nm in the range 500-550 nm.

Further information on the time taken for the dye to permeate is obtained from Fig. 3.13, which shows the intensity maps of 256x256 images acquired (a and c) 1 h and (b and d) 20 h after $Alexa_{488}$ (7 μM) addition to POPC:POPG GVs. The POPC:POPG vesicles were previously incubated for 1 h with 1.3 μM and 10 μM TP10. The intensity scale goes from blue, when the intensity of $Alexa_{488}$ fluorescence is zero or low to red when the fluorescence intensity of the dye increases. This choice allows better visualising changes in fluorescence intensity that can be related to the concentration of the dye. Fig. 3.13 (a) confirms that the lower peptide concentration (1.3 μM) is not enough to form pores because no fluorescent signal appears inside vesicles (the inner part is blue) and it is high only in solution (orange signal). In addition, measures acquired 20 h after fluorescent dye addition, and showed in panel (b), reveal that the system is stable at least for this time. Fig. 3.13 (c) and (d) show that at the higher TP10 concentration, pores are present in the membranes allowing the permeation of the fluorescent dye in a time-dependent manner. After 1 h (panel (c)) from $Alexa_{488}$ addition, the permeation of the dye from outside to inside has already started (the inner part of membranes appears green) but it did not reach the stability. In fact, measures acquired after 20 h (panel (d)) demonstrate that the dye has continued to accumulate inside the vesicles, inducing an increase of fluorescent intensity (orange). It is important to note that despite the presence of pores, no changes in membranes morphology or disruption phenomena are highlighted. However, it is not clear whether the progressive change in intensity is attributable to a different time required for pores to form in the membrane or to the rate of membrane permeation of the fluorescent probe. A model principally used to explain pore formation by α-helical peptides, is the toroidal pore one[188]. In this model, peptides in the extracellular environment take on α-helical structure as they interact with the charged and hydrophobic membranes. Helices are initially oriented parallel to the membrane surface and the hydrophobic residues of the bounded peptides displace the polar head groups, creating a breach in the hydrophobic region and inducing positive curvature strain in the membrane. The introduction of strain and thinning further destabilizes the membrane surface integrity, making it more vulnerable to ensuing peptide interactions. At a threshold peptide-to- lipid ratio, peptides orient perpendicular to membrane, helices begin to self-associate, such that their polar residues are no longer exposed to the membrane hydrocarbon chains, and pores start to form [38].

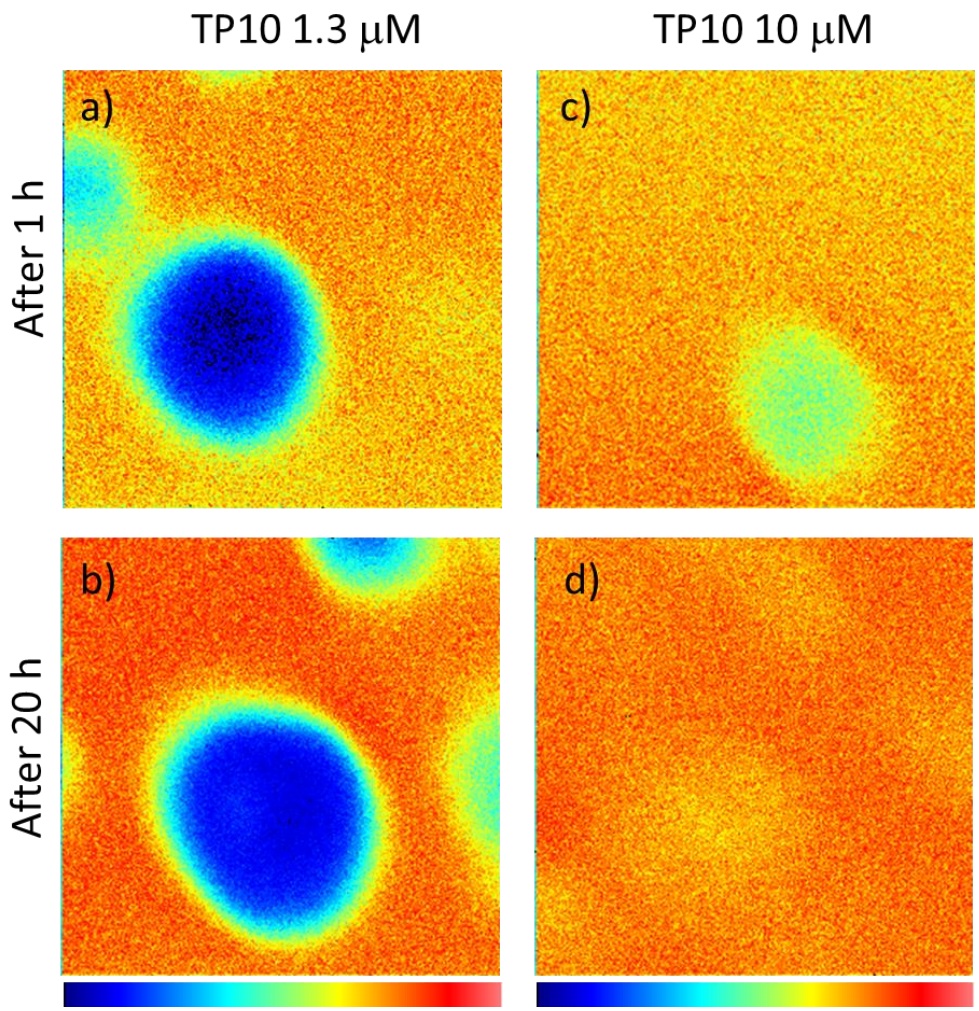

Figure 3.13. 256×256 pixels representative intensity maps of $Alexa_{488}$ (7 μM) acquired after (a and c) 1 h and (b and d) 20 h from its addition to POPC:POPG GVs, pre-incubated for 1 h with (a and b) 1.3 μM and (c and d) 10 μM TP10. The scale bar goes from blue, when the fluorescence intensity is zero, to red when it increases. At 1.3 μM peptide concentration the fluorescent signal stays outside vesicles, while at 10 μM peptide concentration it grows also inside the vesicles in a time-dependent manner.

Tp10 action on giant plasma model vesicles

3.2.6. Fluorescence microscopy and FLIM analysis to analyse TP10 effect on GPMVs

In this second part of the work, GPMVs were used as model membrane. As reported before, GPMVs combine the advantage of having both a cytoplasm and a cell membrane with a defined inner cavity volume and long-term stability without requiring cell cultivation[113,114]. For this study, cancer liver cell line (HepG2) was selected.

Fig. 3.14 shows representative images of HepG2 cells (a) before and (b) after 1 h from the addition of the vesiculation buffer (see details in section 3.4.3). In panel (b) the presence of spherical vesicles,

absent before vesiculation buffer addition and highlighted by the red arrows, is observed. These vesicles present the membrane and internal composition directly mirroring the composition of the cells from which they are originated except for larger cellular organelles. After vesicles formation, GPMVs were separated from adherent cells by transferring the supernatant by pipetting in eppendorf tubes and centrifuged.

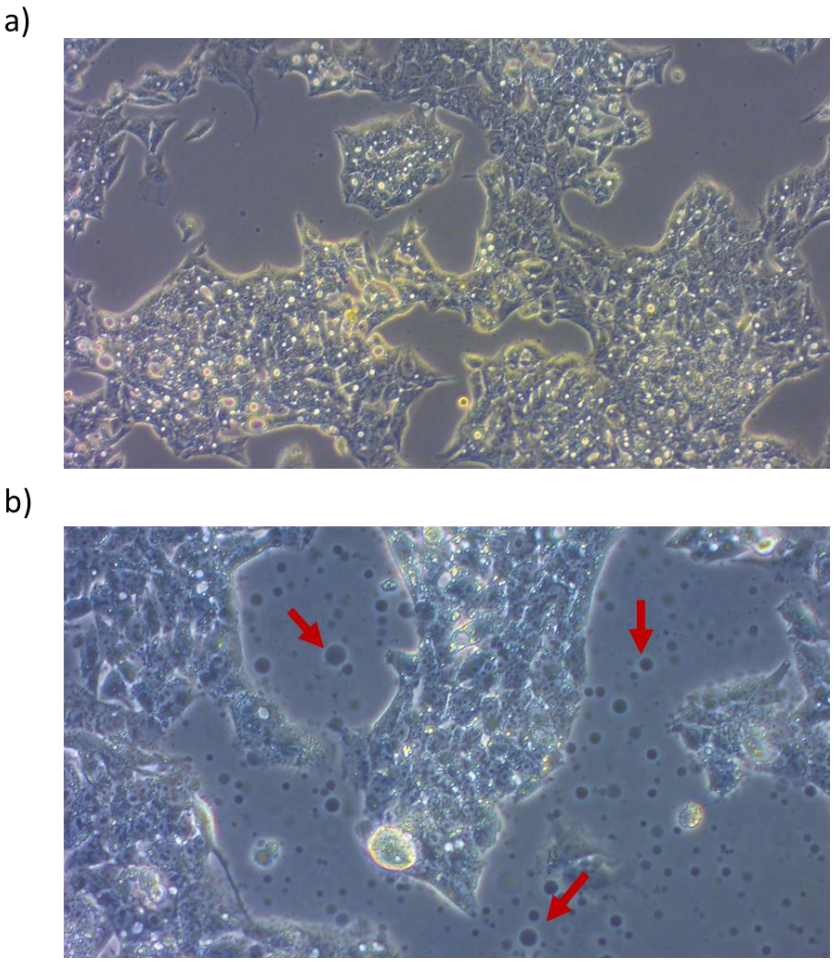

Figure 3.14. Images of HepG2 cells (a) before and (b) after "vesiculation buffer" addition. Vesiculation buffer induces the formation of spherical vesicles, highlighted by the red arrows.

As suggested from preliminary experiments described in the last part of 3.2.5 section, a TP10 concentration of 10 μM was explored. At this concentration it appears that pores are formed in model vesicles.

In Fig 3.15, 1024x1024 pixels representative images of isolated, perfectly spherical, unilamellar GPMVs, labelled with the hydrophobic fluorescent dye NR (see details in section 3.4.3) commonly used as a lipid stain in membranes[189], is reported. The images also reveal that the vesicles are free of contamination of large cytoplasmic organelles.

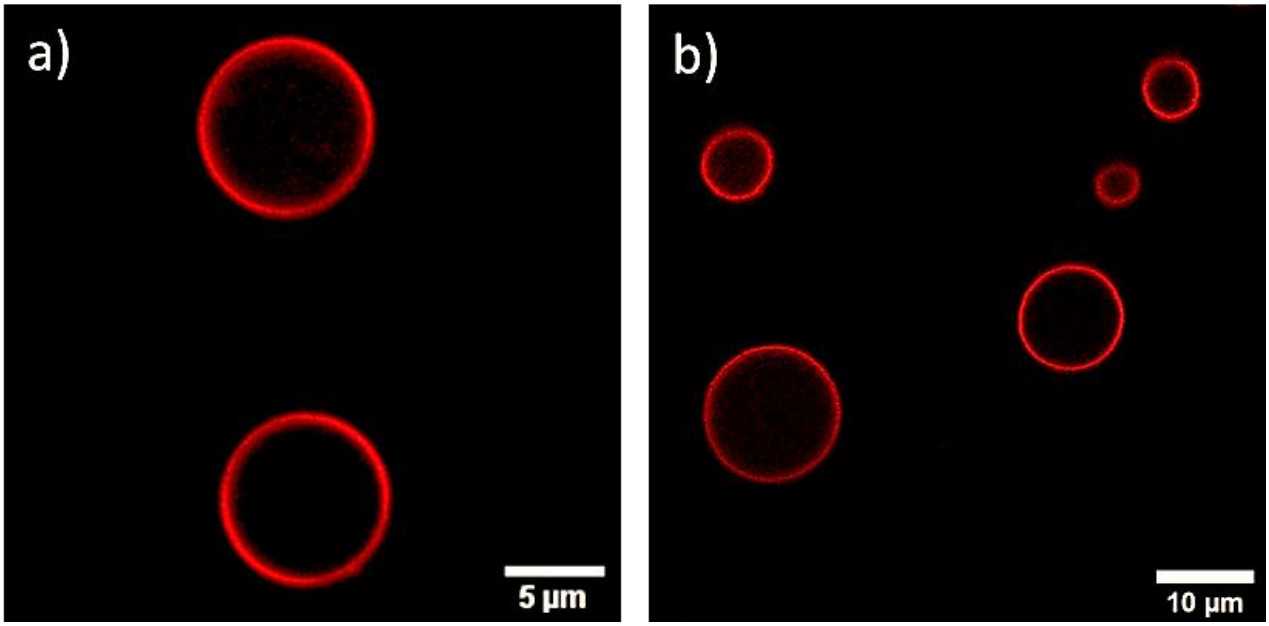

Figure 3.15. 1024×1024 pixels representative LSCM measurements of GPMVs derived from HepG2 cells labelled with (a) NR (λ_{ex}= 540 nm, range 580-700 nm).

Fig. 3.16 reports LSCM measurements aimed at exploring the interaction of TP10 peptide with GMPVs by monitoring changes of membranes morphology and integrity. In Fig. 3.16 1024x1024 pixels representative images of GMPVs labelled with NR, (a) before and after (b) 1 h and (c) 20 h from 10 μM TP10 addition, are reported. Panel (b) reveals that after 1 h from TP10 addition, the GMPVs have started to modify. The presence of diffuse intravesical fluorescence and lipid inclusion in the GPMVs lumen is clearly visible in the images. GPMVs were previously observed to be passively permeable to various hydrophilic solutes[190] in contrast to synthetic giant vesicles; this may be related to issue due to the preparation or imply mechanisms related to endocytosis, a fundamental process of all eukaryotic cells in which extracellular material is taken up by the invagination of the membrane to form encapsulating vesicles. It is known that endocytosis is one the main mechanisms for internalization of cell-penetrating peptides [191,192], which, by inducing a negative-curvature of the membranes, cause an invagination of cell membranes [151,193,194]. However, in the observed conditions significant morphological changes highlight the occurrence of peptide-membrane interactions and exclude passive permeation.

Fig 3.16 (c) reveals that the action of TP10 on the membranes is not completed within 1 h from the peptide addition. In fact, these measurements performed after 20 h show that, although some vesicles have maintained their integrity, TP10 continued to destabilize the greatest number of

vesicles. In particular, some vesicles present edges which are thicker and not perfectly defined anymore, while others are totally disrupted and their fragments appear as lipid cluster that diffuse into the solution.

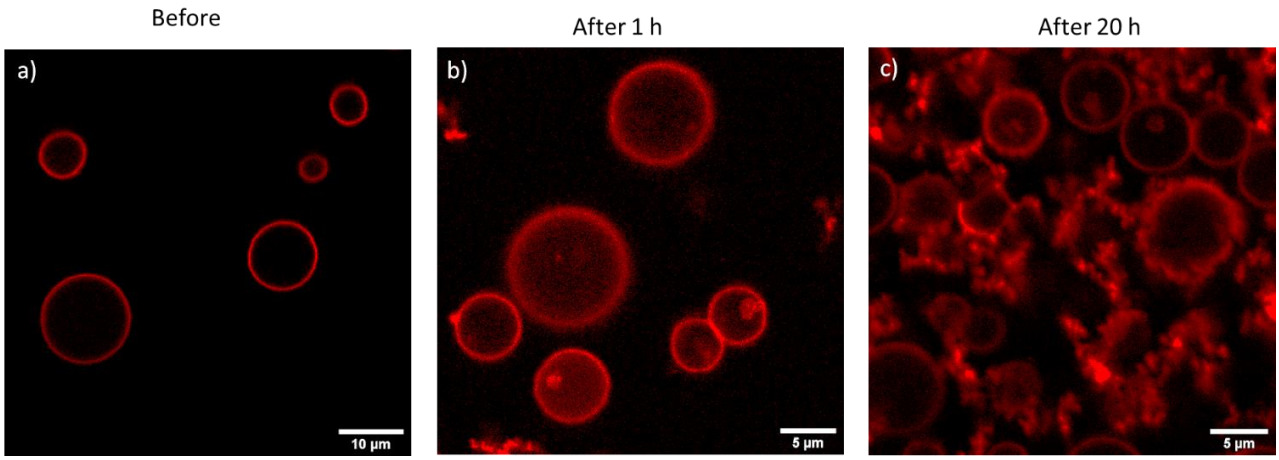

Figure 3.16. 1024×1024 pixels representative LSCM measurements of GPMVs derived from HepG2 cells labelled with NR, before (a), after (b) 1 h and (c) 20 h from the addition of 10 µM TP10. The NR fluorescence intensity signal was collected under laser excitation at 540 nm in the range 580-700 nm.

Now, in order to elucidate the mechanisms that bring the membranes to lose their integrity after TP10 addition, changes of the fluidity and hydrophobicity of bilayers were analysed by means of the analysis of fluorescence lifetime of NR and di-4-ANEDDPHQ. Unlike lipid GV, fluorescence lifetime measurements of both dyes revealed that GPMVs are not stable structures but they change during the time. For this reason, measurements reported below are accompanied by control measurements on non-treated GPMVs measured at the same time after deposition in the chambered coverglasses. In Fig. 3.17 (a and b) 256×256 pixels of NR fluorescence intensity maps in GPMVs (a) in absence and (b) in presence of 10 µM TP10 are reported. The measurements are carried out 1 h after peptide addition. Panels (c and d) show the corresponding phasor color maps in which each pixel is colored according to the corresponding selection in the phasor plots (e and f). In absence of peptide, the sample appears homogeneous and NR is characterized by a single lifetime distribution, highlighted by a red cursor in the phasor plot (e). In presence of TP10, in the phasor plot (f) a broadening of the lifetime distribution is observed. It is possible to qualitatively describe it in terms of two different lifetime distributions highlighted using a red and a yellow cursor. The red cursor highlights the lifetime distribution characterised by longer lifetime which superimposes to the one measured in the absence of peptide (Fig. 3.17 e). The yellow cursor is used to highlight a faster lifetime distribution. The direction of the lifetime modification is indicated in panel (f) by a

red arrow. As evident in Fig. 3.17 (d), pixels where fluorescence lifetime is characterised by the lower lifetime are found at the membranes, while the ones corresponding to the faster lifetime are found within the vesicles.

The observed reduction in the fluorescence lifetime of NR at the edge of the vesicles, following peptide interaction, could be interpreted as a decrease of the hydrophobicity [146,195]. In other words, NR appears to experience a more polar environment possibly due to an increase of the number of water molecules in the hydrophobic bilayer. The presence of intravesical material characterized by the same lifetime (red cursor) of vesicles before peptide addition may stem for the internalisation of more hydrophobic lipids in the vesicles which could confirm the invagination.

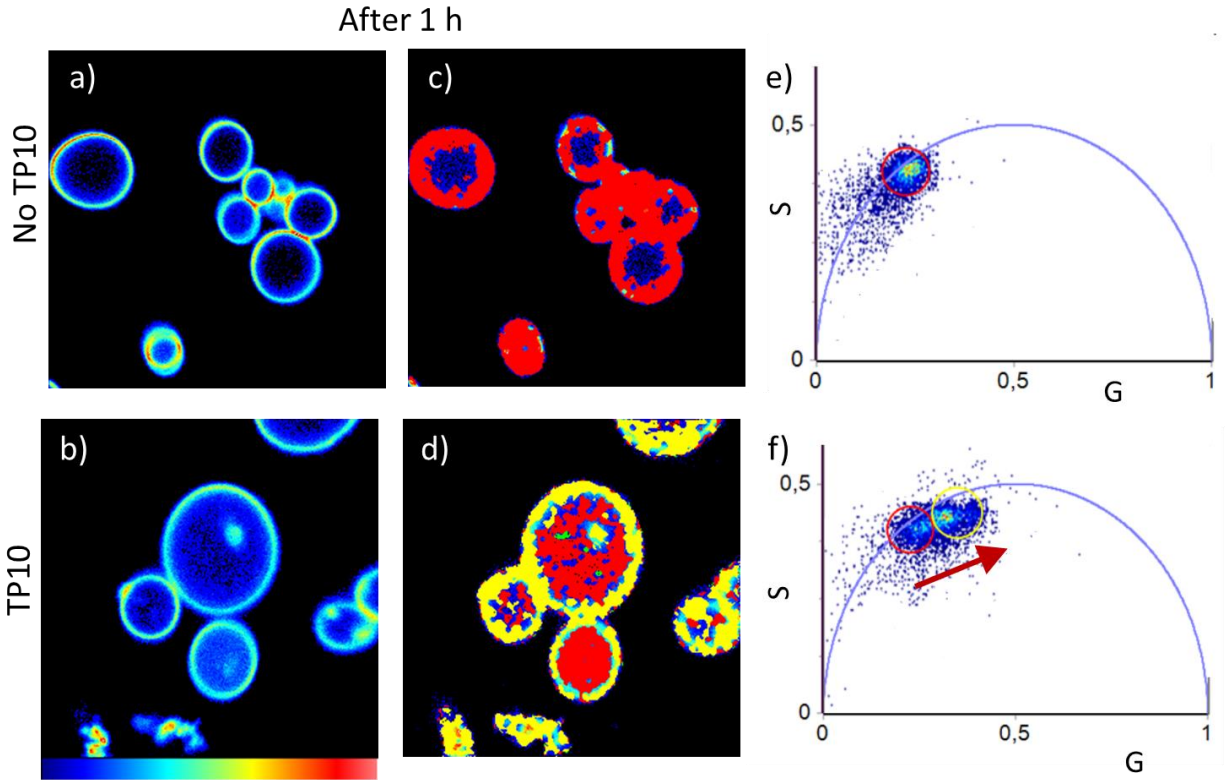

Figure 3.17. Phasor analysis of 256 × 256 pixels FLIM measurements on NR (λ_{exc}= 540 nm, range 580-700 nm) in GPMVs derived from HepG2 cells. Fluorescence intensity images on NR (a) before and (b) after the addition of 10 μM TP10. Both measurements were acquired after 1 h after peptide addition. (c) and (d) the phasor colour maps in which each pixel is coloured according to the colour of the corresponding cursors used to highlight the fluorescence lifetime distribution in the phasor plots (e) and (f) respectively. The choice of the size and the position of the cursor is arbitrary.

The same measurements were then performed on GPMVs 20 h after 10 μM TP10 addition.

In Fig. 3.18 (a and b) 256×256 pixels of NR fluorescence intensity maps in GPMVs (a) in absence and (b) in presence of 10 μM TP10 after 20 h from peptide addition, are reported. Panels (c and d) show

the corresponding phasor color maps in which each pixel is colored according to the color of the cursors in the phasor plots (e and f). Measurements performed on the control sample (panels a, c and e) reveal that untreated GPMVs are not stable structures but they change during the time. Lifetime distributions in the phasor plot (e) is broadened toward longer lifetimes main component, selected using green cursor. The red cursor is in the same position as in Fig. 3.17 (e). The observed changes indicate that NR environment is a homogeneous lipid environment [182] characterized by a less water content, aging of the vesicles possibly leads to dehydration.

Measurements performed 20 h after TP10 addition (panels b, d, f), reveal a large heterogeneity of the sample. Measured fluorescence lifetime changes are in the opposite direction with respect to the one due to sample aging. In particular, there are some few vesicles that have maintained their integrity and are characterized by the same fluorescence lifetime (green cursor) measured for GPMVs measured in absence of TP10, while most of the membranes, which are distorted or destroyed, present shorter lifetime (selected by red and yellow cursors). Some vesicles, as the one indicated by the white arrow in panel (d), appear still intact but present irregular profile. In the phasor map corresponding pixels are colored in red and yellow. These evidences may be rationalised inferring that TP10 could induce increased water molecules accessibility at the external membrane level. Membrane hydration process can be related to membrane disintegration in fragments mostly colored in yellow color (lowest lifetime) in panel 3.18 (d).

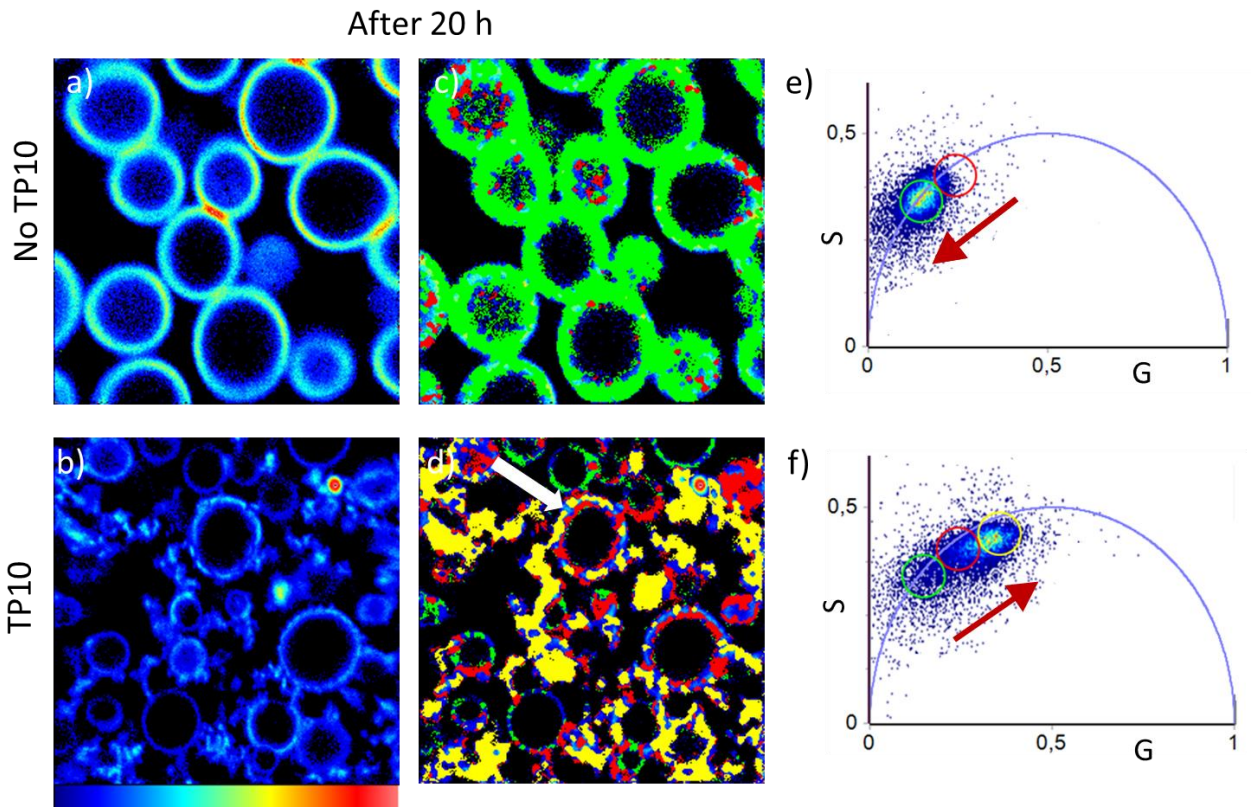

Figure 3.18. Phasor analysis of 256 × 256 pixels FLIM measurements on NR (λ_{exc}= 540 nm, range 580-700 nm) in GPMVs derived from HepG2 cells. Fluorescence intensity images on NR (a) before and (b) after the addition of TP10 10 μM. Both measurements were acquired after 20 h from TP10 addition. (c) and (d) the phasor colour maps in which each pixel is coloured according to the colour of the corresponding cursors used to highlight the fluorescence lifetime distribution in the phasor plots (e) and (f), respectively. The choice of the size and the position of the cursor is arbitrary.

As an example, an analogous measurement, acquired zooming in the area of interest on the single vesicle, is reported in Fig. 3.19. In panel (a) 256x256 pixels fluorescence intensity image of NR in GPMV after 20 h from 10 μM TP10 addition, (b) the corresponding phasor color map and (c) the phasor plot where the green and yellow cursors are in the same position of those reported in Fig. 17 (f). As described above, the sample 20 h after the incubation with TP10 presents a certain heterogeneity and here a representative vesicle, still intact but critically modified in shape, was chosen in order to highlight membrane modifications before the break. Panel (a) highlights that the interaction with TP10 induces a change in the morphology of the membranes. The edges of vesicles appear thicker with respect to the ones in Fig. 3.16 and “wrinkled”. This change, accompanied by the decrease of NR lifetime shown in panel b (membranes are yellow coloured in the lifetime map), can be explained as a decrease of membrane order and increase of water accessibility. NR lifetime distribution at the membrane, within the experimental spatial resolution, is the same as the one

measured for fragments (pixels are colored in yellow in the lifetime map), suggesting that this vesicle may be immediately close to breaking. In these conditions it is reasonable to think that the TP10 perturbs membranes, also forming pores[159], allowing to a high number of water molecules to permeate inside the lipid bilayers, thus exposing NR to a more polar environment. In addition, the different osmotic pressure between the outside of vesicles and the inside, could induce, in an already perturbed membrane, an increase of the number of water molecules that go inwards. This would lead the membranes to swell and burst.

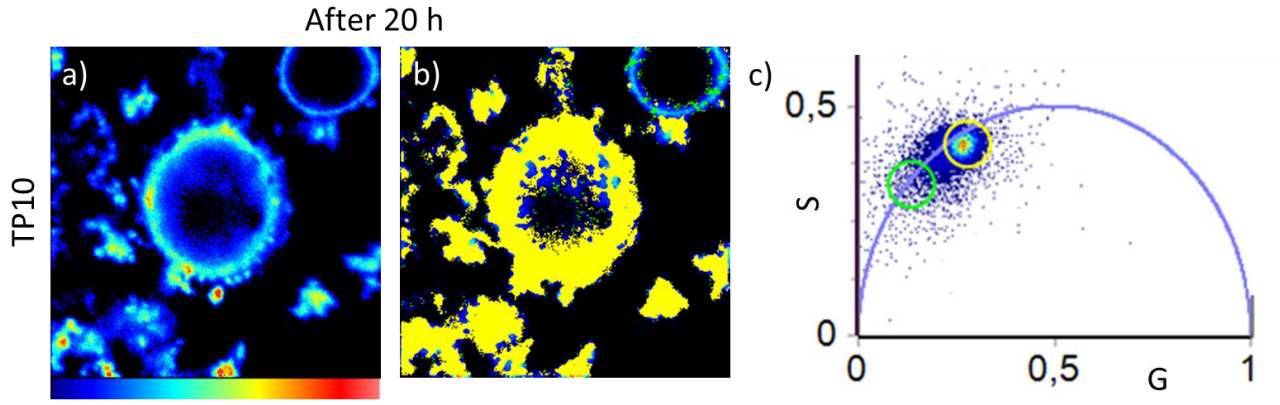

Figure 3.19. (a) 256 × 256 pixels fluorescence intensity images on NR (λ_{exc}= 540 nm, range 580-700 nm) in GPMVs, 20 h after TP10 10 μM addition. (b) Phasor colour map in which each pixel is coloured according to the colour of the corresponding cursor in the phasor plot (c).

To confirm what speculated above about the change of fluidity of lipid bilayers, as a consequence of peptide interaction, membranes were marked using di-4-ANEPPDHQ and FLIM measurements were carried out. In Fig. 3.20 (a and b) 256×256 pixels of di-4-ANEPPDHQ fluorescence intensity maps in GPMVs (a) in absence and (b) in presence of 10 μM TP10 are reported. The measurements are carried out 1 h after peptide addition. Panels (c and d) show the corresponding phasor color maps in which each pixel is colored according to the corresponding selection in the phasor plots (panel e and f).

In absence of TP10, the di-4-ANEPPDHQ presents a single lifetime distribution, highlighted with the pink cursor (panel c), which is located inside the universal circle; this in line with the presence of a heterogeneous lipid environment[182]. The addition of peptide to vesicles induces a broadening of the cloud toward lower lifetime values and Fig. 3.20 (e) reveals that the measured fluorescence lifetime of di-4-ANEPPDHQ is different over a single structure (indicated by white arrow) revealing that the dye is experiencing different environments. Pixels exist with lifetime comparable to the one

measured on vesicles in absence of peptide in solution (pink), other pixels are characterised by a fluorescence signal with lower lifetime (cyan). The observed decrease in lifetime may be ascribed to an increase of the number of water molecules in the lipid bilayer as a consequence of increase of fluidity. This means that a same structure can present a different accessibility to water and so a phase separation. The phase separation in intact plasma membranes, isolated from live cells, has been already observed [113]. This was attributed to tighter packing of cholesterol with phospholipids containing long, saturated acyl chains (L_o) than with phospholipids containing two or more double bonds in their acyl chains (L_d) [196]. In addition, also the presence of proteins is an important contributor to plasma membrane heterogeneity [197] and specific protein/protein and protein/lipid interactions may define various classes of membrane microdomains.

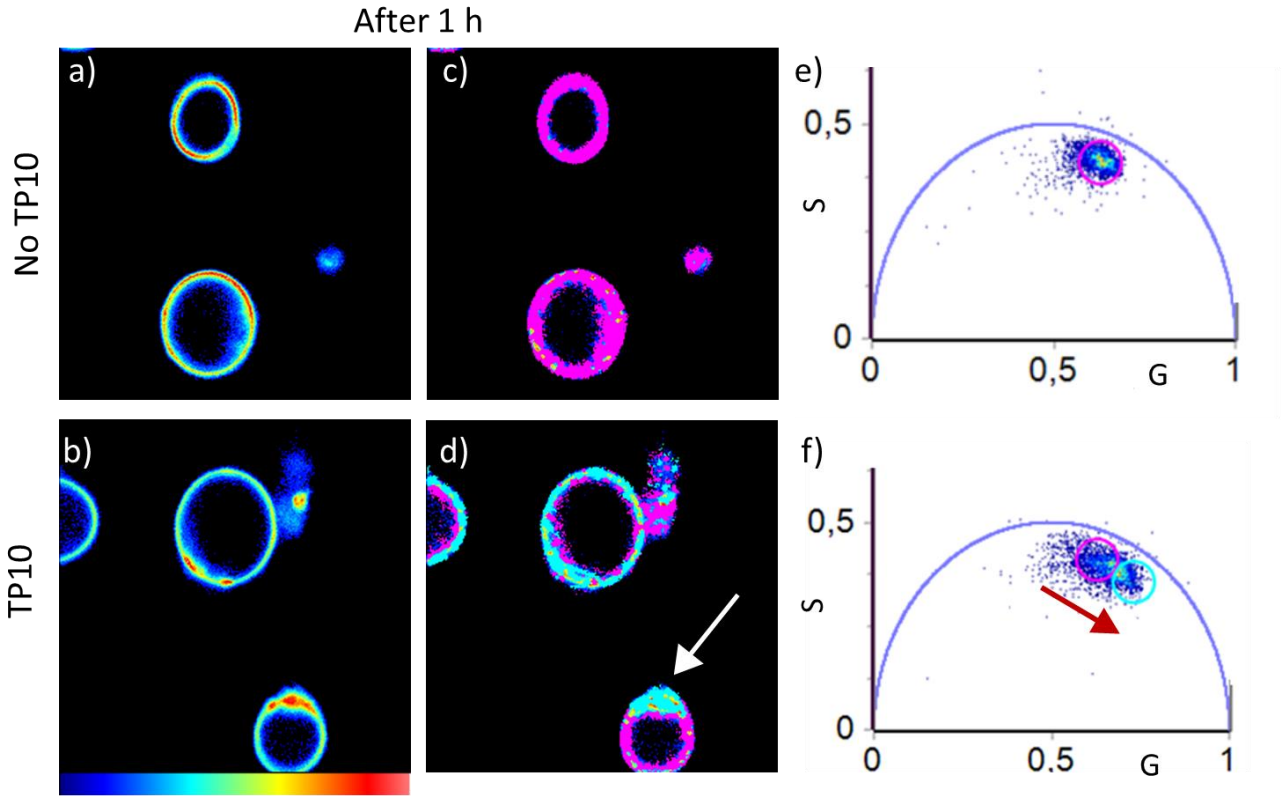

Figure 3.20. Phasor analysis of 256 × 256 pixels FLIM measurements on di-4-ANEPPDHQ (λ_{exc}= 470 nm, range 500-650) in GPMVs. Fluorescence intensity images on di-4-ANEPPDHQ (a) before and (b) after TP10 10 μM addition. Both measurements were acquired at the same time, after 1 h from peptide addition. (c) and (d) the phasor colour maps in which each pixel is coloured according to the colour of the corresponding cursors used to highlight the fluorescence lifetime distribution in the phasor plots (e) and (f), respectively. The choice of the size and the position of the cursor is arbitrary.

Also for di-4-ANEPPDHQ, measurements after 20 h from TP10 addition were carried out and are shown in Fig. 3.21. These measurements confirmed what observed before with NR: vesicles are

dynamic structures whose properties change during the time. In Fig. 3.21 (a and b) 256×256 pixels of di-4-ANEPPDHQ fluorescence intensity maps in GPMVs (a) in absence and (b) in presence of 10 μM TP10 are reported. The measurements are carried out 20 h after peptide addition. Panels (c and d) show the corresponding phasor color maps in which each pixel is colored according to the color of the corresponding cursor in the phasor plot (e).

Panel (e) shows a shift of di-4-ANEPPDHQ lifetime, both in absence and in presence of TP10, toward higher values. This means that the lipid bilayer undergoes a stiffening process that induce expulsion of water molecules. Panel (c) illustrates that also in absence of peptide, after 20 h, the GPMVs are heterogeneous in term of fluidity. Some of them are characterized by higher lifetime (red pixels- lower fluidity), other by lower lifetime (green pixels- higher fluidity) and other present, in the same structure, both lifetime distributions. This means that spontaneously the vesicles go toward a phase separation, even if it is accelerated by TP10 presence (Fig. 3.20 (d)).

Measurements performed after 20 h from TP10 addition (panel d) show the presence of lipidic fragments in solution colored in green. This is in agreement with NR measurements (Fig. 3.18 (d)), which revealed that ruptured vesicles are the ones characterized by higher fluidity.

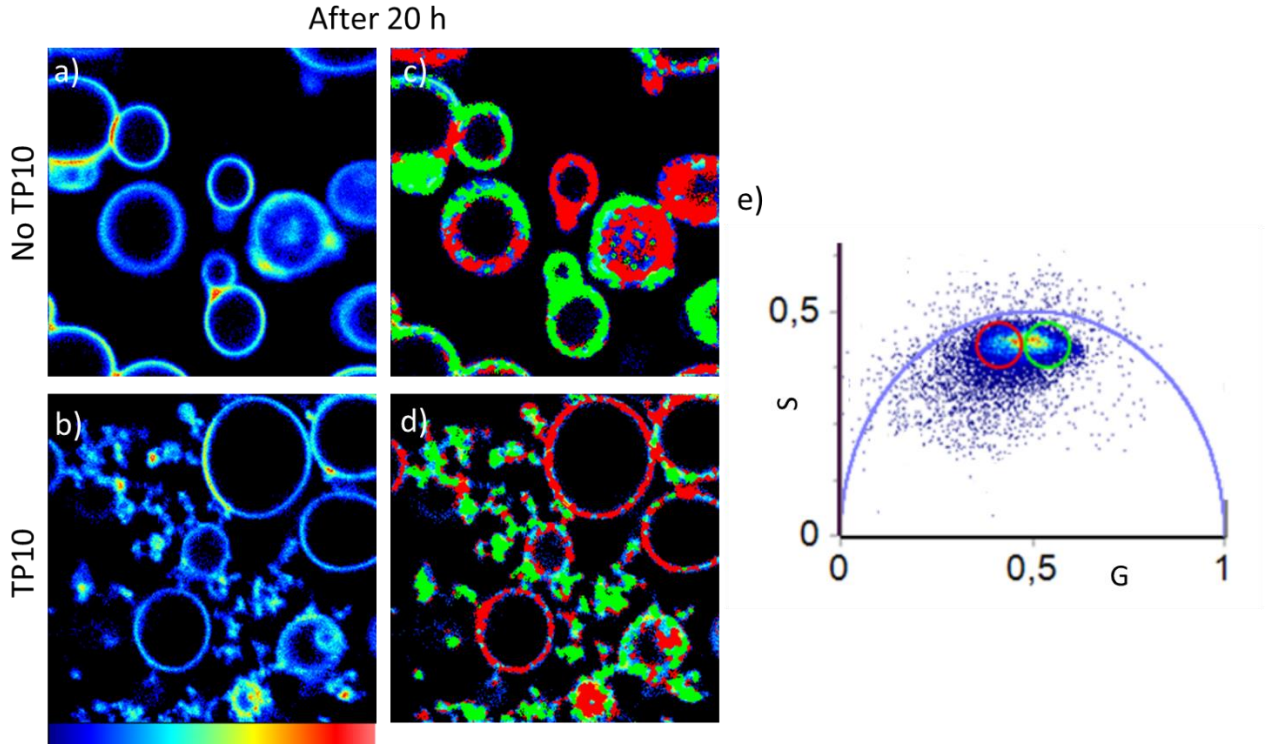

Figure 3.21. Phasor analysis of 256 × 256 pixels FLIM measurements on di-4-ANEPPDHQ (λ_{exc}= 470 nm, range 500-650) in GPMVs. Fluorescence intensity images on di-4-ANEPPDHQ (a) before and (b) after TP10 10 μM addition. Both measurements were acquired at the same time, after 20 h from peptide addition. (c) and (d) the phasor colour maps in which each pixel is coloured according to the colour of the corresponding cursors

used to highlight the fluorescence lifetime distribution in the phasor plots (e) and (f), respectively. The choice of the size and the position of the cursor is arbitrary.

3.3. Conclusions

The analysis of CPPs actions, using model membranes, appropriate dyes, and advanced fluorescence techniques, may contribute to a deeper understanding on how membrane-active peptides act under diverse biological conditions. Here, the fate of TP10 and its effects on two different model membranes were analysed combining spectroscopy and quantitative fluorescence microscopy, which allowed to disentangle the different processes involved in protein-membrane interactions such as adhesion, insertion, pore formation and furthermore to reveal consequent morphological, structural changes and variation in membrane fluidity.

In particular, POPC:POPG GVs were used as model negative charged membranes to mimic those of bacteria and to evaluate the antimicrobial activity of TP10 and study its mechanism of action. The membranes were also enriched with cholesterol to analyse how the presence of sterol affects the interaction of the peptide with membranes that mimic eucaryotic ones. TP10 possible anticancer effects were instead evaluated on GPM vesicles derived by HepG2 carcer cell line.
In the first part of the work, focused on the interaction between TP10 and POPC:POPG GVs, peptide is found not to interact with the POPC:POPG membranes enriched with cholesterol despite of attractive electrostatic forces due to its positive net charge and the negative charged lipids. This, in line with the literature, occurs because the tighter packing of the lipids, induced by cholesterol, reduce the permeability of the membrane and in the observed conditions completely depletes peptide-membrane interactions. In the absence of cholesterol, a concentration dependent interaction between TP10 and model membrane is found. At lower concentration only peptide accumulation at the water membrane interface (adsorption) occurs, which does not induce modification in the lateral organisation of phospholipids. At higher TP10 concentration, data reveal the insertion of the peptide in the membranes, which induces the unstructured peptide to assume a structured α-helix conformation and correlates with the reduction in membrane fluidity and dehydration measured by Laurdan dye. Alteration of the bilayer fluidity caused by interaction with the peptide can lead to instability of the membrane structure and to an enhanced membrane weakness that can be the origin of altered cell and microbial behaviour. Interestingly, the analysis of di-4-ANEPPDHQ, which is positively charged and located in a more internal region with respect to Laurdan, reveals further details and shows that a slower membrane reorganisation occurs leading

to the formation of micron sized domains with overall reduction in membrane fluidity. However, results revealed that TP10 insertion is a necessary but not sufficient condition to induce pores formation in the membranes. One of the main mechanisms proposed for α-helix CCPs is in fact the toroidal pore one[188]. Only at very high values of peptide concentration, the gradually permeation of the fluorescent dye $Alexa_{488}$ from the outside to the inner part of the vesicles occurs as a consequence of pores formation.

Data reported in second part of the work, relative to the interaction between TP10 and GPMVs, demonstrated that, at peptide concentrations where pores are formed in giant vesicles, peptide interacts with membranes, initially inducing an increase of their fluidity. This would allow to a high number of water molecules to permeate the bilayers leading to a decrease of the hydrophobicity. It is not excluded that the increase of water permeation is also connected to the formation of pores following TP10 insertion. Hydrophobicity and fluidity were monitored by FLIM measurements of NR and di-4-ANEPPDHQ, respectively. Furthermore, in the first part of peptide-membrane interaction, the presence of TP10 induces the penetration in the membrane of vesicle components. Peptide-membrane interaction is also related to an increase of membrane fluidity that consequently induces a higher amount of water molecules to penetrate the membrane with a decrease of membrane hydrophobicity. All this perturbs the stability and integrity of the membranes which progressively change their morphology and undergo rupture process.

In conclusion, through FLIM measurements it is possible to analyse the properties of the molecular environment of the fluorophore, to explore simultaneously the peptide localisation and the mutual TP10-membrane interaction at a molecular level gaining in this way information that is hardly accessible via intensity measurements alone.

3.4. Sample preparation and parameters used for measurements

TP10 preparation

TP10 and CF-TP10 (purchased from EZBiolab, Parsippany, New Jersey) were dissolved in 20 mM potassium phosphate buffer (pH 7) and the peptide concentration was determined by absorption measurement by means of a UV–Vis spectrophotometer (Jasco V-760), using an extinction coefficient $\varepsilon_{280nm} = 1298\ M^{-1}\cdot cm^{-1}$.

Giant vesicles preparation and staining

Giant vesicles (GVs) were prepared from POPC:POPG in a 1:2 molar ratio and POPC:POPG:Chol giant vesicles (GVs) in a 1:2:1 molar ratio. POPC, POPG and cholesterol were purchased from Sigma-

Aldrich. The lipid stocks were prepared by mixing the lipids in 3:2 chloroform:methanol solution and dried overnight to form lipid films in round flasks on a rotary evaporator (Buchi (Flawil, Switzerland), Rotavapor R-215, equipped with the Buchi Vacuum Controller V-855). The dry lipid films were hydrated using a 20 mM potassium phosphate buffer at pH 7 and sonicated for 5 min. The resulting sample comprised a heterogeneous distribution of multilamellar giant vesicles with a diameter of several micrometers.

After the GVs formation, the sample was diluted 1:10 and, when needed, labelled using Laurdan and di-4-ANEPPDHQ. Stock solutions of Laurdan (100 μM) and di-4-ANEPPDHQ (100 μM) were prepared in DMSO and stored protected from light exposure. Both dyes were added to diluted GVs in a probe-lipid molar ratio of 1:500 and left to equilibrate for 3 h before measurements.

Giant Plasma Membrane Vesicles (GPMV) preparation and staining

HepG2 cells were cultured in Eagle's Minimum Essential Medium supplemented with 10% fetal bovine serum, 2 mM L-glutamine and 100 units/ml of penicillin-streptomycin at 37°C in a humidified 5% CO_2 and were passaged once a week at 1:2 split ratio. Cells were used at about 70% confluence. Briefly, HepG2 cells were treated with GPMV buffer (10 mM HEPES, 150 mM NaCl, 2 mM CaCl2, pH 7.4) with vesiculation agents (PFA solution (4% (wt/vol)), and were imaged by microscopy (Axio Observer.D1, Zeiss) after 1 h of incubation at 37 °C [113].

After vesicles formation, GPMVs were separated from adherent cells by transferring the supernatant by pipetting in eppendorf tubes. Although most cells remain attached to the flask, cellular debris in the supernatant were separated from GPMVs by differential centrifugation (100g for 10 min).

In accordance with the literature[113], for fluorescence microscopy experiments, the GPMV suspensions were added of Nile Red and Di-4-Aneppdhq in a final concentration of 4 μM and allowed for 1.5 hours for dyes incorporation, prior to any experiment.

Steady state fluorescence spectroscopy in bulk

Fluorescence spectra were acquired at room temperature using a Jasco-FP-8500 spectrofluorometer equipped with a Jasco ETC-815 peltier as temperature controller in 1 cm path length quartz cuvettes. The response time was 1 s, data interval of 0.5 nm and scan speed of 100 nm/min.

CF-TP10 fluorescence emission spectra were acquired, in the range 470-650 nm, using λ_{exc}= 480 nm with an excitation bandwidth of 2.5 nm, an emission bandwidth of 5 nm.

Laurdan fluorescence emission spectra were acquired in the range 370-650 nm as a function of time

every 5 min. Excitation wavelength was λ_{exc}= 380 nm and excitation and emission bandwidth were 5 nm. The cuvette was gently shaken prior to all measurements to keep the sample uniformly dispersed.

Confocal laser scanning fluorescence microscopy (CLSM)

Confocal fluorescence microscopy measurements were acquired using a 63×/1.4 oil objective (Leica Microsystems, Wetzlar, Germany) and a Leica TSC SP5 confocal laser scanning microscope. Scanning frequency was 400 Hz.

Carboxyfluorescein fluorescence signal was detected in the range 500-600 nm, using λ_{exc}= 470 nm. $Alexa_{488}$ emission was acquired in the range 500-550 nm, using λ_{exc} = 488 nm.

Nile red fluorescence signal was acquired in the range 580-700 nm, λ_{exc} = 540 nm.

Fluorescent lifetime imaging microscopy

CF and di-4-ANEPPDHQ fluorescence was acquired using excitation at 470 nm from the pulsed White Light Laser (Leica Microsystem) in the range 500-650 nm.

Nile red fluorescence was acquired using excitation at 540 nm from the pulsed White Light Laser in the range 580-700 nm.

Laurdan fluorescence was acquired under two-photon excitation using λ_{exc}=780 nm in two channels: 410-460 nm (blue channel) and 480-540 nm (green channel).

FLIM calibration of the system was performed by measuring the known lifetime of the fluorescein (for di-4-ANEPPDHQ and CF-TP10) that is a single exponential of 4.0 ns[198]. For Nile Red measurements the lifetime calibration was obtained using $Alexa_{594}$ considering a single exponential decay with 3.9 ns while for Laurdan measurements $Alexa_{405}$ was used, considering a single exponential decay with 3.4 ns lifetime.

Circular dichroisms

The CD spectra were recorded on a Jasco J-715 spectropolarimeter in the far-UV region (194–260 nm), using quartz cuvettes with a path length of 1 cm. All spectra have been acquired at room temperature and for each spectrum, three accumulations have been acquired.

Chapter 4

α-casein-membranes interaction depends on the initial state of protein conformation

4.1. Introduction and purpose

In this chapter with the aim of deepening the general mechanisms underlying the development of pathological or therapeutic conditions, the interaction between POPC:POPG model membranes and α-casein, used as a model protein for its peculiar structural and functional characteristics, were investigated.

Caseins are relatively small milk proteins (molecular mass in the range of 25 kDa) which belong to the family of intrinsically disordered proteins (IDPs) [199]. Several isoforms have been identified in the heterogeneous casein protein family, including α_{S1}-casein, α_{S2}-casein, β-casein, and κ-casein, the main one being α_s (which includes α_{s1} and α_{s2} caseins)[200,201]. These components differ in their amino acid, phosphorus and carbohydrate content, but all of them present an amphiphilic structure [202]. Due to the amphiphilic property, caseins exhibit a strong tendency to self-aggregate into supramolecular structures, and, specifically, into the form of micellar structures which in aqueous solution are held together by the balance of hydrophobic, hydrogen, electrostatic interactions[200,201]. Caseins distinctive structural properties of IDPs and the capability to form amyloid fibrils also makes them an interesting model system in relation to the analysis of potentially pathological protein-membrane interactions. In particular, it was observed the fibril-forming property for κ casein [203] and α_{s2} casein [204], that is countered by the β- and α_{s1}- casein acting in this contest as molecular chaperones. In addition, some studies have also demonstrated the antibacterial activity [205,206]of short peptides characterized by a high number of positively charged amino acids isolated within the sequence of this protein.

α-casein is a 23.5 kDa protein and its isoelectric point is in the range of 4.4-5.3 [207]. At alkaline pHs, between pH 7.4 and pH 10, this protein is characterized by an overall low hydrophobicity, and by a net negative charge [208] that induces the protein to unfold into an open structure characterized by a random coil conformation [209]. Among caseins' family, α-casein is one of the most studied and it is thought to have a central role in micelles formation and in the transport process from the Endoplasmatic Reticulum (ER) to Golgi apparatus within the secretory pathway of mammary epithelial cells [210,211].

At alkaline neutral pHs, α-casein possesses a peculiar aggregative behaviour and it is prone to interact with ligands and lipid interfaces *in vivo*, including biological membranes. By lowering the solution pH, the net positive charge of casein molecules together with hydrogen bonds and hydrophobic interactions allows casein chains' folding into more structured conformations like α-helixes and β-sheets and also aggregating in micellar structures. The difference in pH existing among mammalian organelles, in particular between the neutral pH of ER and the mildly acidic pH of the Golgi [212], may result in conformational changes of protein which could be key factors in the transport phenomena involving casein molecules between these organelles. Moreover, these pH changes may be involved in the functional self-assembly of casein in micellar structures in the Golgi apparatus [210,211].

The main physiological functions of micelles are related to the supply of ions such as calcium and phosphate to neonates [213] and the binding of calcium phosphate to caseins seems to protect the mammary gland from pathological calcifications[200].

Importantly, the compactness, hydrophobicity, and diameter of micellar structures depend on environmental conditions: i.e alteration of the pH may lead to a change in micelle size and a decreased stability [137,208]. Notwithstanding the large number of studies, the structure and the stability of casein micelles in different environment is still highly debated [214,215]. For example, there are controversial opinions on the stability of micelles in alkaline solutions. For several decades, it has been widely accepted that alkaline pH disrupts casein micelles [216,217]. Betsy Vaia et al., observed that the rate and extent of disruption of casein micelles at alkaline pH increased with pH and they are disrupted completely by increasing the pH to 10.0 [216]. Recently, *in vitro* studies have demonstrated their resistance to these pH values. Although the increase of pH swells the micelle, works have demonstrated that attractive forces amongst casein molecules are still sufficient to maintain the micellar integrity even at pH 12 [137,218]. Interestingly, due to their ability to self-assembly and disassembly by changing the pH, they were proposed as emerging biomaterials for drug delivery [219–221]. Specifically, micelle structures have been used for controlled release of hydrophobic bioactive components (such as vitamins) and/or hydrophilic molecules that can be embedded in these nano-supramolecular structures [222].

In the first part of the present study, the interaction between negatively charged POPC:POPG giant vesicles (GVs), and α-casein has been analysed using as starting points two conformational states of α-casein obtained in solution at different pH: micelles stabilised at pH 2 and casein in its native conformational state at pH 7. The choice of such harsh pH as pH 2 is intended to stabilise micellar

species presence in solution, possibly insolating them. This gave the possibility of studying the general physical interactions which induce the loss of stability of these biological relevant species.

The key events and species occurring upon interaction of α-casein with negatively charged model membranes were highlighted thanks to spatially resolved analysis, provided by advanced microscopy. This overcomes the limitations of bulk experiments where key events and protein intermediate states, occurring upon interaction with membranes, are often masked due to the large heterogeneity of the sample in terms of number of species involved (e.g., different aggregation states, protein-lipid co-aggregates etc.) and of their spatial distribution [223]. By means of spectroscopic methods, fluorescence imaging and Raster Image Correlation Spectroscopy (RICS), we analysed this highly complex and spatially heterogeneous phenomenon, which involves i) the protein' structural changes and modification in the association states ii) membranes morphology changes and iii) solvent effects.
Interestingly, obtained results indicate that the initial state of the protein establishes the course of events that occur upon changes of pH and involve both the aggregation processes of α-casein molecules and their interaction with membranes. The two samples' states induce, at the same final conditions, a distinctly different effect on the morphology and stiffness of the membranes. The latter was studied analysing variation of fluorescent Laurdan dye spectral properties.

The second part of the study is aimed at evaluating the effect of the temperature on α-casein micelles by means the same experimental techniques used in the first part. In addition to pH, also the temperature plays a key role in regulating conformational changes and activity of proteins[3,224]. In particular, high temperatures can disrupt hydrogen bonding and hydrophobic interactions that hold the protein in a certain conformation, and lead protein to misfold and possibly to aggregate, forming potentially toxic species [225,226]. Previous works have already shown that the effect of temperature on the size of the micelles is different depending on the environmental conditions. Here presented results reveal that in acidic aqueous solution, high temperatures lead the micelles to aggregate each other in larger structures, probably due to the increased hydrophobic effect [227].

The effect of these new species on POPC:POPC GVs was evaluate by means spectroscopic measurements of Laurdan in cuvette, fluorescence microscopy and RICS analysis. These experiments, which combine bulk and single vesicles measurements, demonstrate that although micelles in their aggregated or not aggregated form seem to induce the same change on membranes

morphology, there are small but significant differences in the interaction time of the two samples with vesicles and in the stiffness of membrane induced by them. This confirms once again that the initial state of the protein governs its fate. All these observations may be essential for understanding the possible functional, pathological or therapeutic properties associated to α-casein proteins.

4.2. Experimental results and discussion

pH driven conformational states modify mutually disruptive α-casein membrane interactions

4.2.1. α-casein forms micelles at acidic pH values

In cellular environment, different conditions, as different local concentration of proteins or local presence of different ions, changes in pH, carbohydrates compositions, may regulate multiple mechanisms. They can either minimize aggregation or molecular interactions and maintain functional state favourable or the opposite. *In vitro* it is possible, by varying the solvent properties, to modify the association/ aggregation state. For example, dimethylsulfoxide (DMSO) and 2,2,2-trifuoroethanol (TFE) were found to induce disaggregation by interfering with H-bonds stabilized β-structure [228,229]. Exposing fibrils to ethanol or TFE–water mixtures resulted in protein aggregates disassembly and reassembly, thus suggesting that changes in dielectric constant of the surrounding medium is fundamental for the amyloid stability [16,230,231]. Salt concentration and pH changes were shown to both promote aggregation and trigger fibril association and dissolution [232].

In particular pH is one fundamental parameter that significantly affects protein conformation and aggregation due to its effects on protein net charge[233,234]. With the idea that the balance between hydrophobic and electrostatic interactions regulates protein conformational and aggregation state and, following the same general laws, it regulates the effectiveness or protein membrane interactions the first part of the work is aimed at characterising the differences in α-casein aggregation state, secondary structure, hydrophobicity existing between α-casein at neutral and acidic pH. To this aim, RICS analysis, circular dichroism and fluorescence spectra measurements of two extrinsic dyes (Pyrene and Ans) were used.

Fig. 4.1 reports RICS analysis, which was used to not invasively assess the potential presence of protein supramolecular assemblies in different solution conditions. Panel (a) shows 256×256 pixel size representative images of 36 μM α-casein samples (containing $Alexa_{488}$ labelled protein at 13 nM) in solution at pH 2 and pH 7 together with the spatial autocorrelation functions and the fitting. Fluorescence images in panel (a) do not reveal the presence of structures with characteristic size above diffraction limited resolution of the microscope (~200 nm) so that uniform fluorescence is

measured. In line with this observation, the shape of the autocorrelation functions is characteristic of free diffusion. Several measurements were performed on multiple areas of the samples and diffusion coefficients obtained from RICS analysis are reported in panel 4.1 (b).

A critical difference is found between the two samples, being the diffusion coefficients in the sample at pH 7 significantly larger than the one in sample at pH 2. The measured diffusion coefficient for α-casein pH 7 sample is about 60.0 $\mu m^2/s$ and, in line with literature, stems for the dominant presence of proteins in the monomeric form or self-associated into dimeric or tetrameric structures [235]. In α-casein samples at pH 2 the measured D is about 31.0 $\mu m^2/s$, indicating the presence of large slow diffusing aggregates. This result is in accordance with data reported in literature showing that α-casein has a great tendency to form micelles (about 10 subunits or more) at this pH and, accordingly, this result indicates the presence of supramolecular micellar structures [137].

In order to verify if the protein exists in different aggregation states (i.e., different diffusion coefficients), we used the moving average (MAV) subtraction tool. Indeed, in the cases where large species are evident in the RICS measurements, immobile subtraction algorithm was used to eliminate the contribution to fluctuations of all the immobile/slowly diffusing species residing in the same pixel for a time longer than the acquisition time of multiple frames [33,236]. The number of the frame averages used for the immobile substation is indicated by the MAV. By changing the length of the MAV, it is possible to select processes on different timescales, define the time scale of slow intensity fluctuations that affect the RICS autocorrelation function and eliminate them. Our data, reported in Fig. 4.1 (c) reveal that the autocorrelation functions, varying the MAV, are not affected in their shape meaning that the sample is characterised by homogeneous size distribution over the observed timescale.

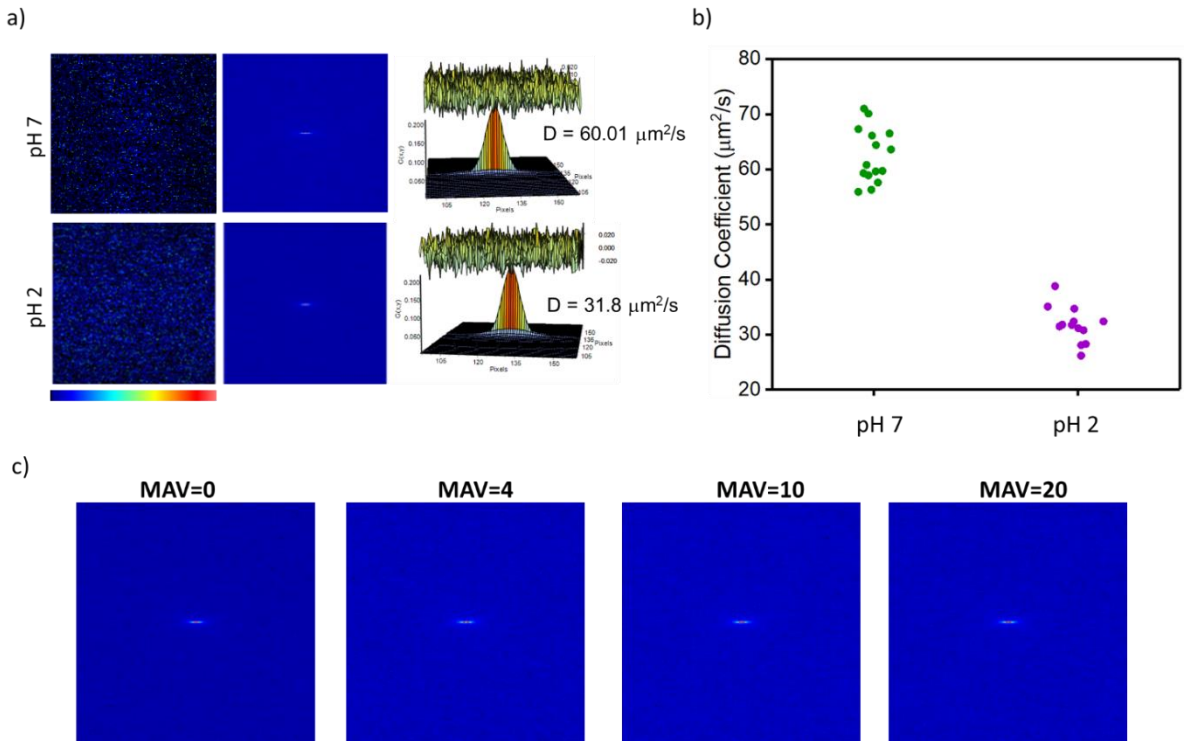

Figure 4.1. (a) Representative 256 × 256 confocal images of 36 μM α-casein in pH 7 and pH 2 labelled with $Alexa_{488}$ (13 nM). Spatial autocorrelation function of the two samples and their respective fits are also reported. The diffusion coefficients (D) are of about 60 μm^2 /s for α-casein pH 7 and of about 32 μm^2 /s for α-casein pH 2 (b) Diffusion coefficient distribution of the two samples. (c) Spatial autocorrelation functions of 36 μM α-casein pH 2 without immobile fraction subtraction and after immobile fraction subtraction with MAV=4, MAV=10 and MAV=20. In this case by changing the moving average the correlation function does not undergo variations so that it is possible to exclude that, slow particles contribute to the diffusion.

Differences in the aggregation state of proteins often coincide with their conformational changes because the latter can determine an exposure of reactive hydrophobic, charged groups buried, giving rise to new intermolecular interactions. Modifications of secondary structure of proteins, which are strictly influenced by pH, are detected by monitoring their CD spectra in the far UV region, where the main contribution to the spectra comes from the peptide backbone [150]. Fig. 4.2 shows the far UV CD spectra of α-casein at pH 7 and pH 2.

In line with data reported in the literature [209], at pH 7 α-casein presents a CD spectrum characteristic of a high content of α-helices and random coil structures. Increasing the pH above the isoelectric point of protein molecules, gives rise to an increase of the negative charges that strengthen the repulsive forces of the α-casein chain, which in turn, produces loose and expanded structures. At pH 2 the spectrum shows a shift of the first minimum in ellipticity from 200 to 206 nm accompanied by spectral changes which is indicative that random coil conformations are replaced by ordered

conformations like α-helices and intermolecular β-sheets. At acidic pH, i.e. below the protein isoelectric point, many amino acid residues in α-casein, such as lysine, arginine and histidine are protonated. It is widely accepted that the ability of H^+ to form hydrogen bond is stronger than that of the neutral H atoms, it is possible to infer that hydrogen bonds between aminoacidic residues are stabilised within α-casein molecules in these conditions that lead to more structured conformations which is revealed by the observed CD spectrum.

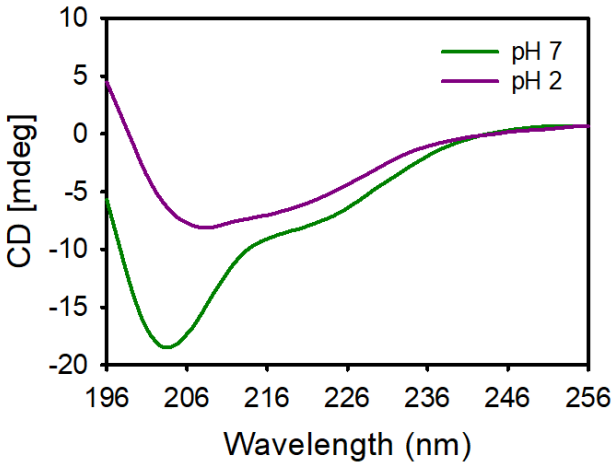

Figure 4.2. Far-UV (194-260 nm) CD spectra of 36 μM α-casein pH 7 and α-casein pH 2.

To corroborate the idea that micelles are present in the sample at both pH values, experiments using the hydrophobic Pyrene fluorescent dye were performed. Pyrene has been already used to probe the existence of α-casein in micellar state and to investigate the influence of pH on micelles properties [137]. In Fig. 4.3 (a) the fluorescence emission spectra (λ_{exc} = 330 nm) of Pyrene in solution pH 2 and pH 7 in presence or not of the two α-casein samples are shown. These measurements are aimed at corroborating the idea that micelles are present in the sample at pH 2 and that only small fraction of α-casein molecules are organized in micelle structures at neutral pH. Variation in the fluorescence intensity ratio between the peaks centred at 373 nm and 393 nm (I_1/I_3) is considered an indicator of the presence of these structures and can be used as a quantitative determination of its surrounding polarity. Pyrene I_1/I_3 drastically changes with the change in the polarity of the medium; the value of I_1/I_3 is higher when the probe molecules are in a more polar environment. In presence of micelles in solution, its incorporation inside micelles because of their hydrophobic character, induces the decrease of the I_1/I_3 ratio. The reported data show that Pyrene in aqueous solution at both pHs is characterized by a peak ratio $I_1/I_3 = 1.10 \pm 0.01$ (overlapped spectra). In the presence of α-casein this value decreases to 1.06 ± 0.01 at pH 7 and to 1.02 ± 0.01 at pH 2. This

result supports the hypothesis of a dominant presence of micellar structures at acidic pH and that only small fraction of α-casein molecules is organized in micelle structures at neutral pH.

Additional measurements were also performed using another extrinsic dye, the ANS whose fluorescence is strongly dependent on the polarity of the local environment around the chromophore [237]. In water, the emission is relatively weak, with a maximum around 520 nm. Upon binding to hydrophobic patches of proteins, the fluorescence spectrum is blue-shifted with a maximum around 470 nm and the emission intensity is increased [137]. In Fig. 4.3 (b) the fluorescence emission spectra (λ_{exc}= 350 nm), normalized for their absorbance at 275 nm, of ANS dissolved in the two samples at pH 2 and 7 at the same concentration are reported. They show a high fluorescent emission with a maximum centred at 470 nm for ANS added to α-casein sample at pH 2, while a lower fluorescent emission, with a maximum centred at 480 nm, for ANS added to α-casein sample at pH 7. Also in this case, results are in line with previously reported literature indicating a higher affinity of ANS for α-casein in acidic conditions suggesting the presence of stable and compact micellar structures [208].

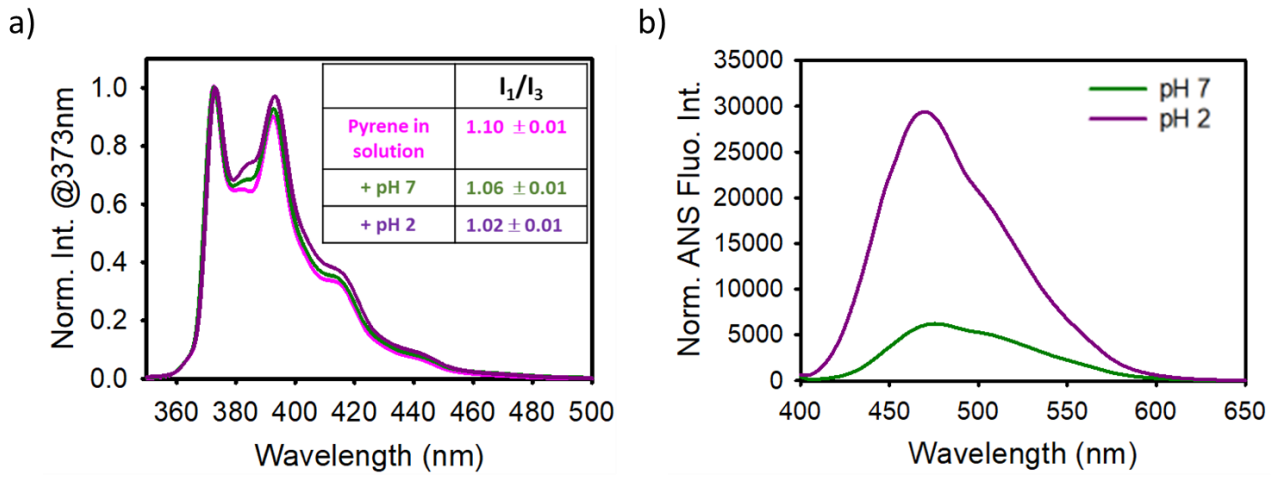

Figure 4.3. (a) Fluorescence emission spectra (λ_{exc} = 330 nm), in the range 350–550 nm and normalized to their value at 373 nm, of Pyrene (1×10^{-6} M) in solution pH 7 and solution pH 2, both in absence and in presence of α-casein. Spectra in water solution in the absence of protein are overlapped. The results of the ratio between the first and the third peaks are reported in the table in the inset. (b) ANS (9×10^{-6} M) fluorescence emission spectra (λ_{exc}= 350 nm, range 400-650 nm) in presence of 36 μM α-casein pH 7 and pH 2.

The results shown reveal that α-casein can form micelles in a pH-dependent manner, being their formation significantly favoured at acid pH. This is in line with recent studies that have shown that

micelles destabilisation is a pH-driven process. Changes in the surface charge and the consequent conformational changes, modulated by electrostatic and hydrophobic interactions, may favour or disfavour the formation and regulate the compaction of micellar structures [202,208]. The hydrogens bonds, between α-casein molecules favoured at acid pH, together with the hydrophobic ones and the so-called cation–π interactions between the cationic side chains of lysine, arginine and histidine and the aromatic side chains of phenylalanine, tyrosine, or tryptophan residues play a key role in the self-assembly of α-casein [201]. The global observation of previous data makes clear the nature of the two samples in the selected experimental conditions, revealing that α-casein monomers, with α-helical and random coil structure, constitute the dominant population in sample at pH 7. At pH 2, compact α-casein micellar structures are mainly present stabilised by intermolecular β-structures whose formation is favoured by acidic pH.

4.2.2. Destabilization of α-casein micelles changing the pH

The conformational flexibility of α-casein proteins represents a really good chance to study *in vitro* the molecular events controlled by pH changes. Indeed, pH alterations could force conformational modifications and aggregation/disaggregation processes whose occurrence may be related to different biological effects. This is common in intracellular environment where pH changes are known to affect many cellular properties as they induce changes in membrane potential, in the diffusion or action of different molecules, in functional interactions, in the state of polymerization of the cytoskeleton etc. To regulate cellular functions, many organelles lysosomes, mitochondria and endosomal vesicles act as functional compartments, which maintain their internal pH different from the cytoplasmic one [212,238]. In this scenario, as a model we analyse the fate of the two samples characterized at pH 2 and pH 7 when the pH of the solution is brought to the isoelectric point of the protein at pH 5.3. This is aimed at revealing the role of the electrostatic interactions in protein stability, at highlighting key events and protein states and at focusing on how the "sample's history" affects the protein-protein and protein-environment interactions. In other words, we will verify that environmental changes induced modifications in protein structures and those following intermolecular interactions keep memory of the initial environmental conditions and protein aggregation state.

Fig. 4.4 shows 256 × 256 representative confocal fluorescence microscopy image of α-casein at pH 2 (final concentration 36 μM labelled with $Alexa_{488}$ (13 nM)), added to solution pH 7 to reach a final pH of 5.3. At this pH, large amorphous aggregates are visible. Near the pI of the protein, the decrease

in net charge weakens the intra- and inter- chain interactions, the stabilization of micelles decreases too and they start to become closer to each other, coalesce and form denser aggregates that precipitate in micron scale aggregates. Therefore, while at acidic pH it is possible to infer that the α-casein molecules are preferentially held together by hydrogen bonds and cation-π interactions, at pH 5.3 the main forces involved are likely to be the hydrophobic ones.

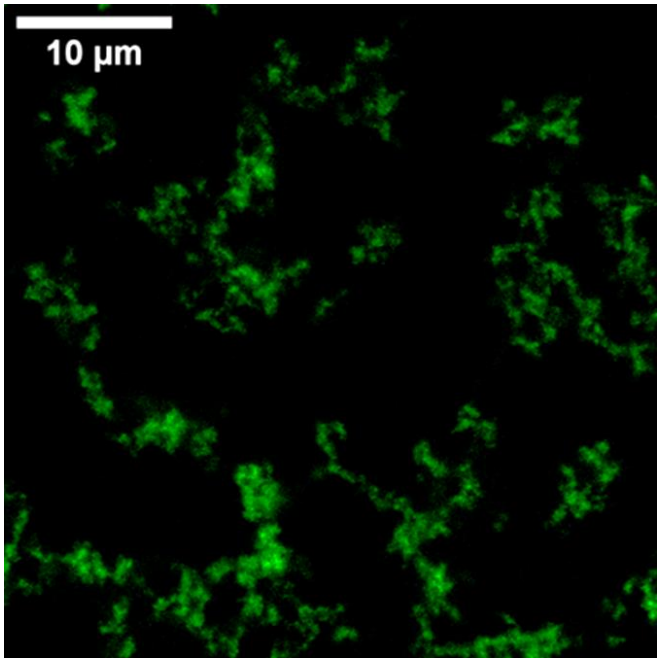

Figure 4.4. 256 × 256 representative confocal fluorescence microscopy image of 36 µM α-casein in pH 2 added to pH 7 solution reaching a final pH of 5.3. α-casein molecules at pH 5.3 assemble together in amorphous larger aggregates.

To obtain accurate spatio-temporal information on protein diffusion and aggregation status during this pH change, RICS measurements are performed. Fig. 4.5 (a) reports 256 × 256 pixel size representative images of 36 µM micelles containing 13 nM component of protein labelled with $Alexa_{488}$ together with the representative spatial autocorrelation function and the fitting calculated in a 64 x 64 ROIs. As can be seen, an appreciable inhomogeneity in fluorescence signal attributed to labelled proteins is found. This suggests the coexistence of multiple species in solution and the presence of fluorescent protein aggregates. For this reason, to analyse RICS data MAV subtraction was used in order to eliminate the contribution of the immobile molecules and to emphasize processes on different timescale. The MAV=10 used for this analysis, given the experimental

conditions (frame time=1.2 s), corresponds to a residence tie of ~10 s. The diffusion coefficients distributions of these species obtained by RICS analysis in different areas of the sample are reported in Fig. 4.5 (b). Data prove that when the sample is brought to pH 5.3 from micellar state, it shows a heterogeneous distribution. In particular, large low diffusing protein aggregates with D = 2 ± 2 $\mu m^2/s$ are formed. In the same sample, other smaller diffusing species are found characterized by diffusion coefficient values ranging from 17 $\mu m^2/s$ to 70 $\mu m^2/s$. The latter is comparable to the diffusion coefficient of α-casein pH 7 (Fig. 4.1. (b)). This means that, as expected, micelles are not stable structures but undergo a partial disassembly and reassembly process when bring to pH 2 to pH 5.3.

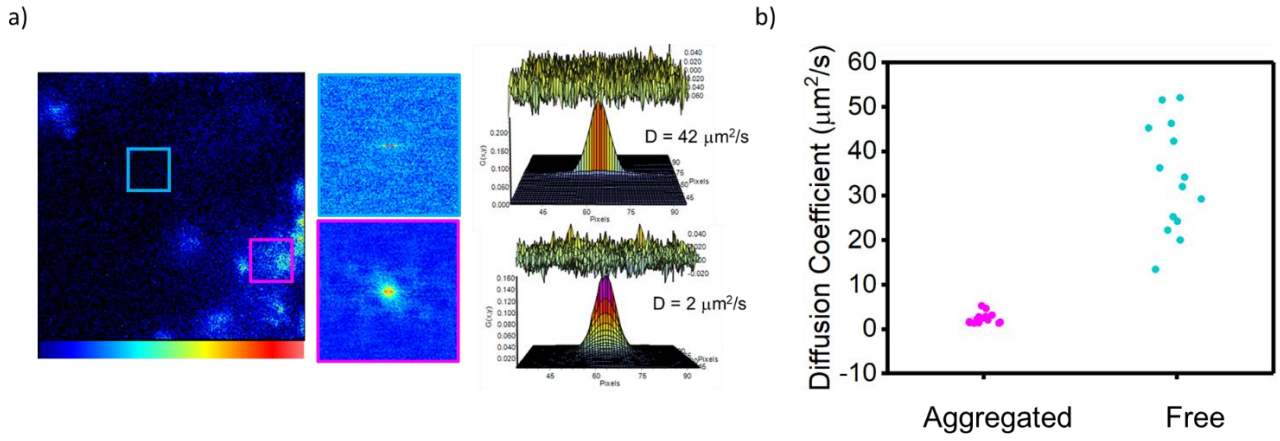

Figure 4.5. (a) Representative 256 × 256 confocal images, the corresponding spatial autocorrelation functions of areas marked (64 × 64) and the respective fits of 36 μM α-casein in pH 2 added to pH 7. Large amorphous aggregates characterized (D ~ 2 $\mu m^2/s$) coexist with smaller species (D ~ 42 $\mu m^2/s$). (b) Diffusion coefficient distribution of the aggregated part and free one in solution.

Fig. 4.6 shows spectroscopic measures aimed at analyse if conformational modifications and changes of polarity of the sample occurs as a consequence of pH alteration. In particular, fig 4.6 (a) reports the far-UV CD spectra of α-casein before and after pH change from pH 2 to pH 5.3. These bulk measurements show a decrease in magnitude when the protein is at pH 5.3, that is in accord with the formation of larger aggregates near the isoelectric point, and a significant change in spectral shape due to pH change. In particular, the first peak at 206 nm decreases in magnitude, becoming almost equal to the second minimum at 222 nm. This suggest that the sample loses its initial structure and undergoing structural changes toward α-helix structures.
In addition, ANS fluorescence measurements were carried out to analyse if the observed conformational change induces a different exposure of the hydrophobic residues. ANS spectra, reported in Fig. 4.6 (b), reveal that a critical reduction in intensity and red shift occur when the

sample is titrated at pH 5.3. Specifically, the decrease and the red shift (peaks are now centred at 480 nm) of ANS spectrum in presence of α-casein at pH 5.3 could be due to a different exposure of the α-casein hydrophobic patches to the dye and/or the decrease of the electrostatic interactions between the positive charges of α-casein and ANS negatively charged. Thus, ANS at pH 2 was in close interaction with micellar structures, following the pH changes the affinity or the number of the binding sites for this dye result to decrease.

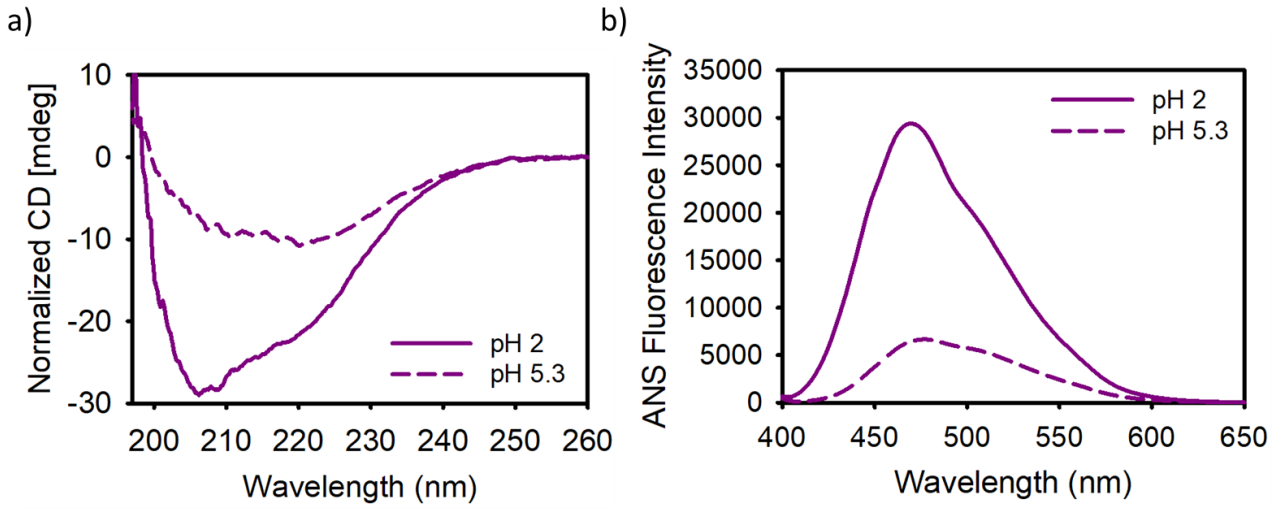

Figure 4.6. (a) Far-UV (194-260 nm) CD spectra and (b) ANS (9×10^{-6} M) fluorescence emission spectra (λ_{exc}= 380 nm, range 400-650 nm), normalized by absorbance, of 36 μM α-casein brought at pH 5.3 (dotted lines) in comparison with α-casein in pH 2.

Summing up, by changing solution conditions, electrostatic interactions between protein molecules are critically modified. The observation that micelles quickly disassemble confirms the idea that electrostatic controls the stability of micellar structures. At pH 2, many amino acid residues are protonated so that intermolecular H-bonding capability is increased favouring micellar structures formation. Increasing the pH, the ionization of acidic side groups of aminoacids like aspartic acid (Asp) and glutamic acid (Glu) of the proteins increases, whereas that of the basic side groups decreases; as a result, the net-negative charge and hence intermolecular repulsion increases, which may lead to the loose structure of the α-casein micelles. Interestingly, by repeating the same experiments series using the sample at pH 7 corrected towards pH 5.3, small CD spectral changes are in line with the one observed in the literature for sample at similar pH values [209](data not shown) and macroscopic aggregation is not observed (confirmed below by measurements in Fig. 4.10 (a)).

4.2.3. Aggregation state of α-casein regulates protein-membrane interactions induced by pH switch

The study of disassembly and reassembly phenomena aims to highlight the events underling both physiological and pathogenic processes. Depending on environmental conditions (i.e. pH, temperature), proteins can go towards aggregation processes, which may be followed by abnormal interactions with the environment. It is known that α-casein reacts very rapidly to environmental changes and it is able to interact with multiple target molecules and in particular with lipid membranes [211,213,239]. This study aims to shed light on the significance of membrane interactions in α-casein aggregation and disaggregation processes and to clarify if the interactions have adverse effects upon lipid bilayer properties and morphology.

The data below highlight the events occurring when α-casein micelles are brought at the protein isoelectric pH in a sample containing model membranes. Spectroscopic cuvette measurements of Laurdan, used to label POPC:POPG GVs, in presence of α-casein micelles when the system is brought to a final pH of 5.3, were performed. These experiments aimed to obtain bulk information on membrane organisation in term of hydration and fluidity of phospholipid bilayers as a consequence of protein interaction. As reported in detail in Chapter 2, the fluorescent signal of Laurdan molecule strictly depends on the membrane phase (e.g., local and translational mobility) and its modification induce changes in the GP values [142,175]. In Fig. 4.7 Laurdan fluorescence analysis of the sample is reported. This shows that at time zero, before protein addition, membrane is in the liquid phase (GP ~ -0.04) and so more accessible to the solvent. A previous study [239], aimed at evaluating the role of phase of the phospholipid membrane caused by its interaction with α-caseins, revealed that α-casein particles interacted with bilayers in their liquid state and not with solid phase bilayers, probably because of the compact lateral organization of the phospholipids in the solid phase that prevents penetration of the protein. After α-casein addition, a progressive increase of the GP value occurs, meaning a change of membrane fluidity toward a more ordered phase due to protein interaction. In particular, an abrupt increase of the GP value from -0.04 to 0 in the first 5 minutes is followed by a slow and more or less linear growth of the GP value to 0.03. After 50 minutes the GP value seems to have reached the stability. The presented results show that the membrane stiffening is mild but significant and that protein interaction induces dehydration of lipid bilayers resulting in more rigid membranes [46–48,140,142].

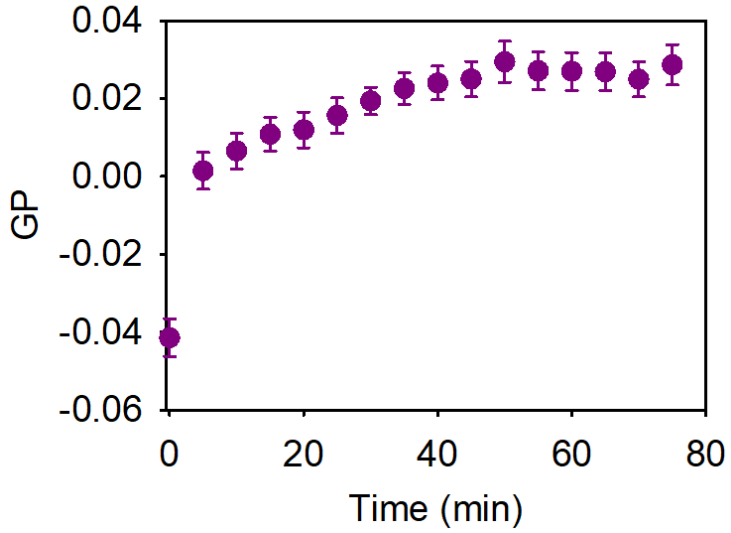

Figure 4.7. Time evolution of GP ratios obtained from the analysis of fluorescence spectrum variations of Laurdan (λ_{ex}= 380 nm, acquisition range = 370-650) used to stain POPC:POPG vesicles after the addition of α-casein micelles.

In order to investigate if the morphology of single vesicles is affected by the α-casein presence and to localize the protein during its interaction process, double color fluorescence microscopy measurements were carried out. In particular, Fig. 4.8 shows representative fluorescence microscopy measurements on POPC:POPG giant vesicles stained with Laurdan (magenta channel) (a) before and (b) after 10 minutes from the addition of 36 μM α-casein labelled with $Alexa_{488}$ (13 nM) (green channel), initially in the micellar state at pH 2 towards a final pH of 5.3. $Alexa_{488}$ fluorescence is used to follow the fate of protein, which is found to colocalise with GV's membranes. Panel 4.8 (a) shows liposomes that in the absence of protein present a regular shape, with almost spherical morphology; the sample shows a detectable heterogeneity in terms of size (ranging from 2 to 10 μm) and in bilayer organisation. Panel 4.8 (b) demonstrates the spatial overlap between the fluorescence signals acquired in the two channels that occurs after the addition of labelled protein, thus indicating that the protein interacts with GUVs. Images also reveal that α-casein interacts only with the outer part of the membranes. As can be seen, the green signal is revealed only at the edges of GVs, while no protein is localised in the core. In the observed optical section of lipid membrane structures, it is clearly evident that co-localisation occurs (white areas) between lipid layer and proteins at the micronscale, suggesting that α-casein molecules are not only adsorbed on membrane surface but they insert in the bilayer. This results in a dramatic membranes remodelling, leading to the observed micronscale flower-like structures (one of them is highlighted by dotted

box). The changes in membrane rigidity found by bulk measures (Fig. 4.7) are likely to be localised on interactions sites where protein is localised in the external part of the vesicles. To confirm this, two-photons experiments on Laurdan labelled membranes in presence of not labelled α-casein will be performed. As already observed[48], this experiment will allow to analyse the fluorescence signals, obtaining GP measures on single vesicle and thereby providing information on the physical characteristics of lipid bilayers and morphological changes induced by α-casein, simultaneously.After α-casein addition, liposomes seem to semi-crystallize into co-aggregates with spherical symmetry constituted by a central lipid core and an external shell with hybrid lipid- α-casein composition. It is also evident that other structures are also present in the sample that appear only made of protein molecules as they are not significantly stained by the lipophilic dye (green micron scale structures, highlighted by dashed box).

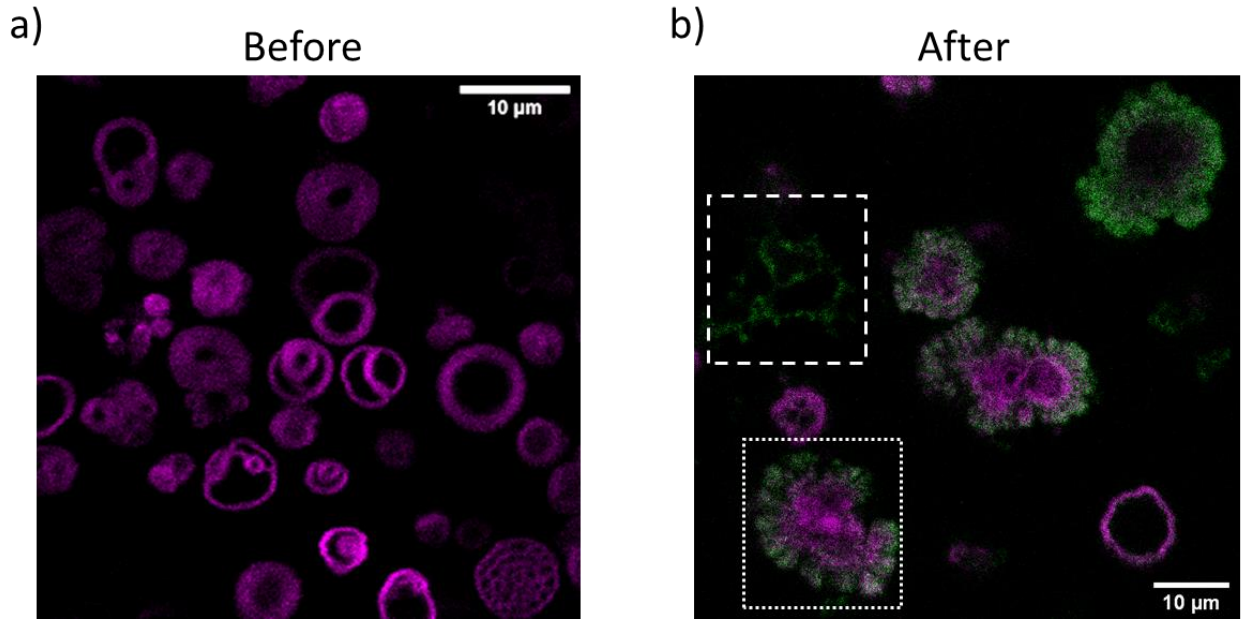

Figure 4.8. 1024 X 1024 pixels representative fluorescence image shows POPC:POPG vesicles, stained with Laurdan (magenta), (a) before and (b) after the addition of 36 µM $Alexa_{488}$-micelles. In presence of 36 µM $Alexa_{488}$-micelles, the overlap of two colors indicates protein-vesicles co-localization that induces a clearly membrane morphology modification. The boxes highlight α-casein aggregates formed at pH 5.3 (dashed) and the liposome with a flower-like conformation (dotted) after protein interaction.

To gain further information on the interaction, RICS experiments were performed by adding 36 µM micelles labelled with $Alexa_{488}$ (13 nM) to unstained giant vesicles to a final pH of 5.3. Changes in diffusion coefficient were monitored. Before α-casein addition, liposomes are only visible in the

transmission channel, while upon interaction with α-casein, fluorescence is observed at the membrane. In Fig. 4.9 (a) I report RICS analysis: 256 × 256 pixel size representative images of liposomes in presence of $Alexa_{488}$-micelles, where coloured squares represent 64 × 64 pixel regions of interest (ROIs) where the analysis was performed. Corresponding spatial correlation functions and fits are also shown. By analysing different ROIs in the image, we are able to disentangle the contribution of freely diffusing α-casein structures in solution away from the membrane and α-casein molecules in close proximity or interacting with the membrane. The diffusion coefficient distributions of α-casein diffusing in solution, α-casein aggregated and α-casein that interacted with liposomes are shown in Fig. 4.9 (b). After α-casein addition to the sample, the measured diffusion coefficient in ROIs away from the liposome's membrane is variable and ranging from 17 $\mu m^2/s$ to 65 $\mu m^2/s$, being comparable with data in Fig. 4.5 (b). These data suggest the disassembly of the micelles. In these conditions α-casein molecules are likely to assume the same state as the one measured at the same pH in the absence of membranes. Measurements in region where liposomes are present show that a certain fraction of protein interacts with membrane structures: the measured diffusion coefficient at the membrane drops to lower values 6 ± 2 $\mu m^2/s$. This value is distinguishable from diffusion coefficients reported for protein aggregates (2 ± 1 μm^2 /s) found in the absence of liposomes which are also found in this sample.

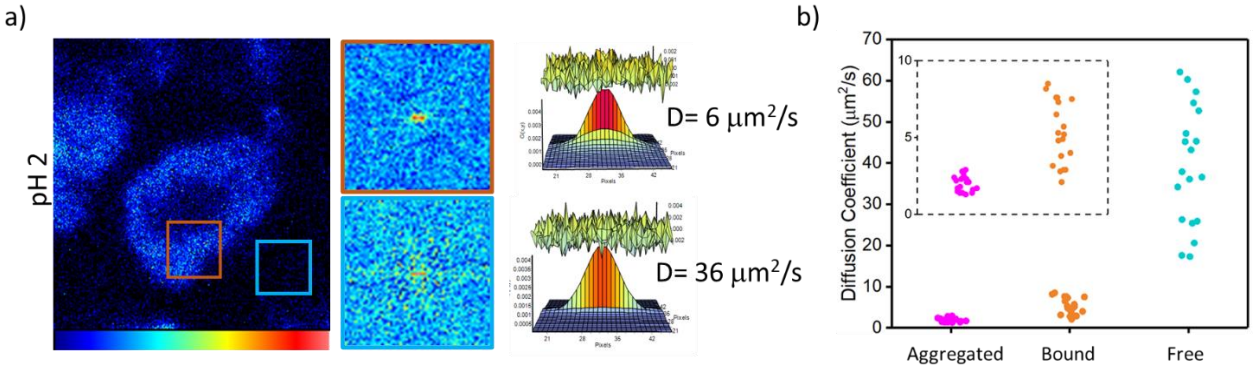

Figure 4.9. (a) 256 × 256 representative confocal images of liposomes interacting with α-casein in which coloured squares represent 64 x 64 ROIs where RICS measurements are performed. Spatial autocorrelation functions and relative fits, spatial correlation functions are marked with the same colour of the ROI in which they are calculated. (b) Diffusion coefficient distributions of α-casein in its different states (free, aggregated and bound to liposomes).

Interestingly, if the same experiment is repeated in conditions where the protein starts from its native like state at pH 7 only minor changes are observed. In Fig. 4.10 the RICS analysis of a sample

containing non stained liposomes is reported after the addition of 36 µM α-casein pH 7 labelled with 13 nM $Alexa_{488}$. Final pH of this sample is pH 5.3 as before. In panel 4.10 (a) a representative fluorescence intensity image is reported where no structure with size above the optical resolution are observed. The correlation function and respective fit are also reported whose analysis gives back a diffusion coefficient of 47 ± 10 $\mu m^2/s$, which is compatible with the presence of native protein diffusing together with small oligomers, which may be formed due to the loss of electrostatic interactions. Interestingly, in this case, the liposomes are only visible in the transmission channel (Fig. 4.5 (b)), no significant fluorescence signal is observed at their surface and their morphology remains unvaried. This clearly indicates that, in the observed conditions, no significant interaction occurs

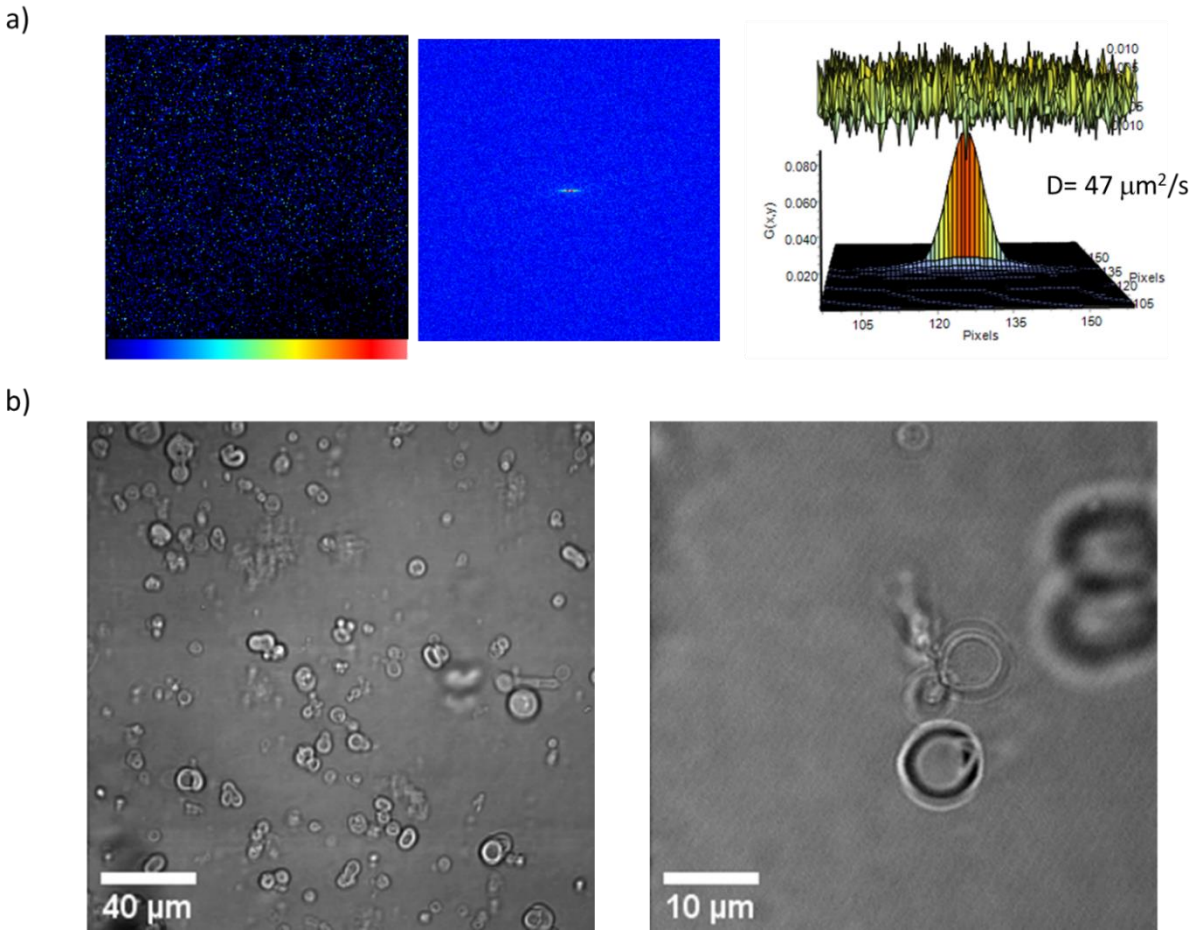

Figure 4.10. (a) RICS analysis: right column: 256 × 256 representative confocal images of liposomes added of α-casein-$Alexa_{488}$ (36 µM, pH 7). Final pH is brought to 5.3 value. Left column: spatial autocorrelation functions and relative fits. (b) representative images of POPC:POPG liposomes in the transmission channel.

The liposomes are visible only in the transmission channel indicating that no interaction occurs between protein and membrane.

At pH 5.3, liposomes are negatively charged and the protein has a negligible charge disfavouring both aggregation and protein adhesion to lipids. Summarising these results, it is possible to state that α-casein interactions with membranes, in conditions where the net charge of the protein is reduced close to zero by a sudden change in pH is regulated by the initial state of the protein.

Thermally induced α-casein aggregation states modulate interaction with model membrane

4.2.4. High temperature induces micelles aggregation: spectroscopic and microscopic characterization

α-casein micelles described above where thermally treated at 70 °C for 24 h in order to induce aggregation. This in line with the general idea that high temperatures induce aggregation processes associated with protein unfolding, which allows hydrophobic parts of different proteins to form intermolecular structures [235,240,241]. The sample was characterised using the same protocol described above. In the following, micelle samples described in previous section at room temperature in solution at pH 2 will be referred as "N-c", while the abbreviation "H-c" will be used to indicate the sample after thermal treatment.

To assess sample aggregation RICS measurements are reported in Fig. 4.11, this allowing the direct comparison with previously reported measurements. Although in recent years, dynamic light scattering (DLS) has become the method of choice for evaluating particle size [241], to corroborate the hypothesis that α-casein micelles aggregate in larger structures at high temperature, RICS technique has been chosen. RICS, presents the advantages to be sensitive to single molecules and allows MAV subtraction which may represent a useful tool to separate the contribution to the signal of larger species [33,242] which often hinder DLS analysis.

Fig. 4.11 shows the RICS analysis of the α-casein sample in solution pH 2 subjected to heating process. 256 × 256-pixel size representative image of 36 μM H-c, containing 13 nM component of protein labelled with $Alexa_{488}$, is reported together with the representative spatial autocorrelation function and the fitting, obtained from the analysis of the sample. As can be seen an appreciable spatial inhomogeneity of fluorescence distribution is found for H-c sample if compared to N-c one (Fig. 4.1). This suggests the coexistence of multiple species in solution and the presence of fluorescent protein aggregates. The measured D value for H-c sample (about 4 $\mu m^2/s$) is significantly

smaller than the one measured for N-c sample (about 35 $\mu m^2/s$, Fig. 4.1) revealing the presence of larger aggregates in the H-c sample. In these cases, immobile subtraction algorithm was used to eliminate the contribution of fluctuations due to these large species, which are found in the same position for several time frames. The MAV algorithm was used and the length of the MAV was optimized to the larger number of frames until the calculated autocorrelation function remained the same. This procedure is aimed at eliminating the contribution of immobile species.

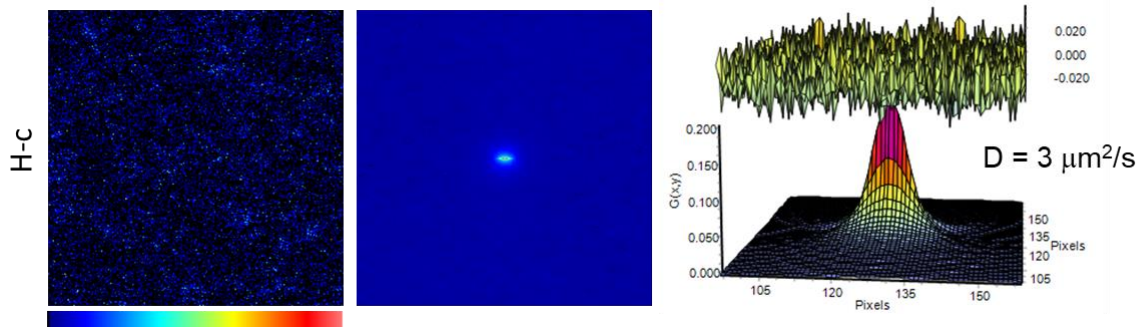

Figure 4.11. Representative 256 × 256 confocal images of 36 µM H-c (at 70 °C for 24 h) in pH 2 labelled with $Alexa_{488}$ (13 nM). Spatial autocorrelation function and the respective fit are also reported. The diffusion coefficient is 3 $\mu m^2/s$.

Fig. 4.12 compares results previously discussed in Fig. 4.2 and Fig. 4.3 on α-casein micelles pH 2 to analogous measurements performed on H-c sample.

As shown in panel (a), circular dichroism spectra not reveal significant differences between the N-c and H-c samples, indicating that the heating treatment does not alter the secondary structure of micelles. H-c, as well as N-c, presents by two minima at 206 and 220 nm already attributed to a high content of intermolecular beta-structures. Also Pyrene fluorescence spectra reported in panel (b) are superimposable being the I_1/I_3 ratio for both samples is 1.02 $\pm$ 0.01, confirming that this dye senses analogous environment in terms of hydrophobicity and that the number of micelles in solution does not change. A small difference is found in the fluorescence spectra of ANS as evident in Fig. 4.12 (c). The N-c sample intensity results slightly but significantly larger while the spectral profile and the position of ANS fluorescence emission remain the same. This difference could be explained in terms of a reduced number of accessible hydrophobic binding sites [243,244], due to increased compactness of micellar structures induced by thermal treatment, which may cause reduced accessibility of internal region of aggregates to the dye [243]. Moreover, it is possible to think

that micelles undergo aggregation, due to the increased hydrophobic effect, so that the non-polar residues in the surface, involved in ANS binding in N-C, are not available as they can be involved in intra-micelles interactions with other non-polar patches.

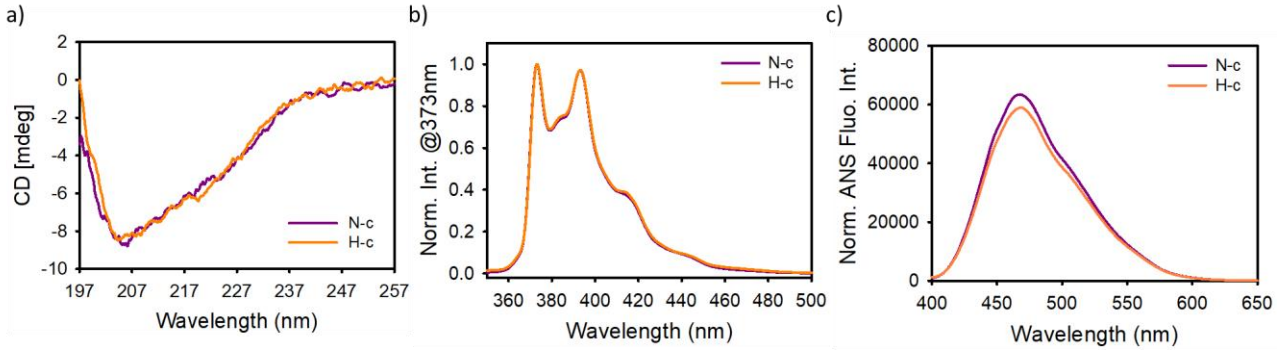

Figure 4.12. (a) Far-UV (197-257 nm) CD spectra of 36 µM N-c and H-c (pH=2). (b) Fluorescence emission spectra (λ_{exc} = 330 nm), in the range 350–550 nm and normalized to their value at 373 nm, of Pyrene (1 µM) in presence of N-c and H-c. (c) ANS fluorescence emission spectra (λ_{exc}= 350 nm, range 400-650 nm) added to 36 µM N-c and H-c solution.

All together these measurements suggest that α-casein micelles do not critically change in terms of structure and in number but they interact to each other. Due to thermal treatment hydrophobic interactions favour the clustering between intact micelles leading to micelle aggregates.

4.2.5. Micelle aggregates disaggregate and re-aggregate when brought close the isoelectric point.

In view of results reported in section 4.2.3 on N-c samples, the importance of electrostatic interactions on the stability of micellar aggregates was also evaluated by RICS techniques by bringing the sample from pH 2 to pH 5.3. This method can in fact be used to detect in real time and in a non-invasive way the aggregation-disaggregation processes highlighting spatially heterogeneous mechanisms. The measurements revealed that micelle aggregates are not stable structures and at a pH value close to the isoelectric point, when the net charge decreases, they disassemble and form amorphous aggregates with larger size. This is being an analogous behaviour to the one observed for micelles subjected to the same pH switch. The RICS analysis performed on H-c sample allowed to spatially and temporally follow the fast process that leads to the formation of these visible structures in solution.

In Fig. 4.13 (a-d) 256x256 pixel size representative images, acquired in different times, of 36 µM micelles aggregates containing 13 nM component of protein labelled with $Alexa_{488}$, are shown. The respective autocorrelation functions and fits are reported in panels (e-h) and (i-n), respectively. The

spatial autocorrelation function immediately tapers off and the disappearing of the vertical component, which takes in account for slower species, is evident (Fig.4.14 (b)). After that, the autocorrelation function is progressively modified and, as a function of time, can be analysed to recover the diffusion coefficients. In the representative image the progressive appearance on micron scale diffusing aggregates is observed with larger size with respect to the one measured at pH 2. Fig. 4.13 (o) shows the diffusion coefficient change over time as a consequence of pH modification. The initial increase of D to the value of 65 ± 10 $\mu m^2/s$ reveals the presence of protein in monomeric form or self-associated into dimeric or tetrameric structures. This is followed by a decrease to 1.2 ± 1 $\mu m^2/s$, passing through intermediate values of 20 ± 10 $\mu m^2/s$. It is a very fast process that reaches the stability within 10 minutes.

Finally, it is important to notice that as observed for micelles, not only large aggregates are present in the sample but they coexist with smaller species. RICS allows to analyse samples in different regions of interest (ROI) within the same image. 64x64 ROIs were analysed and representative results are reported in Fig. 4.14, where a 256x256 pixel image of the sample, chosen as example, containing two representative ROIs colored squares is shown. Results highlight the fact that the sample is highly heterogeneous and that, at the end of the process, it contains micron-scale and monomeric species. Specifically, for data reported in Fig. 4.14 the analysis results in a diffusion coefficient of 1.9 ± 0.2 $\mu m^2/s$ where large clusters are observed (e.g. red square) and in diffusion coefficients of 42 ± 10 $\mu m^2/s$ in areas where no aggregates are evident (e.g. green square).

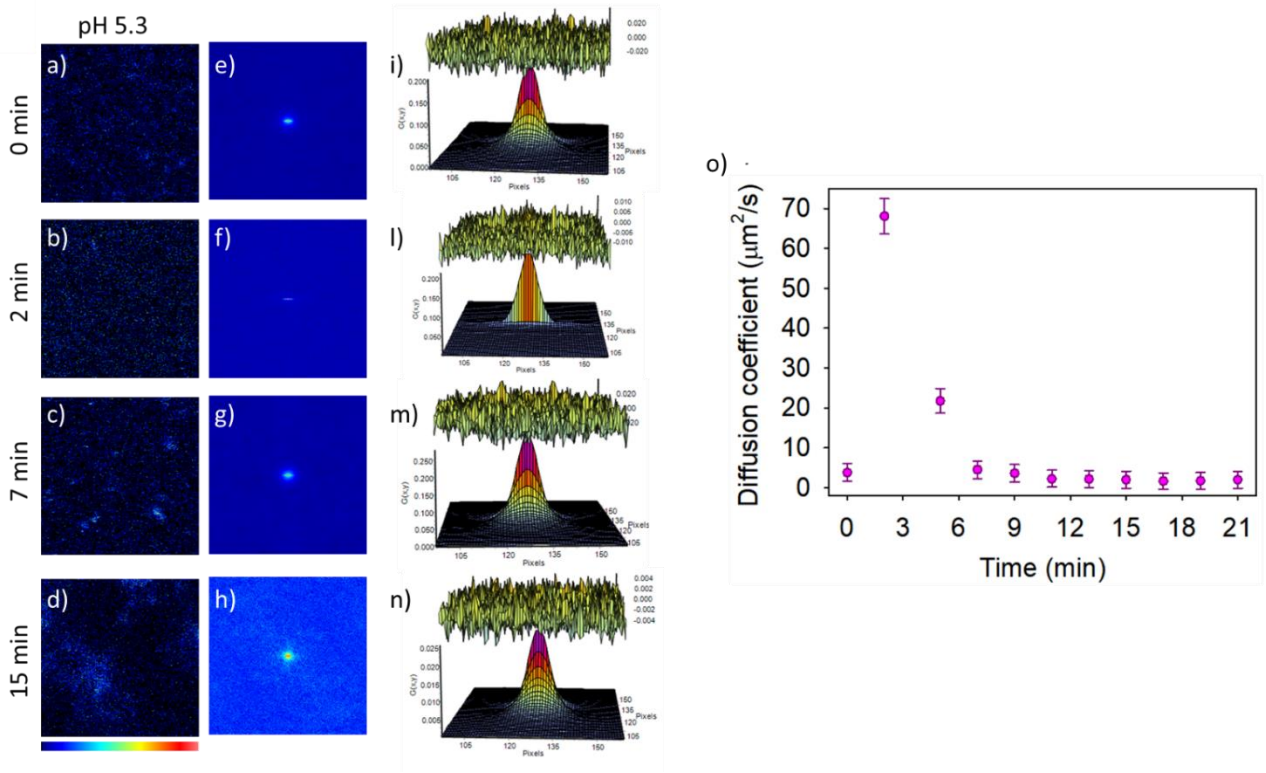

Figure 4.13. (a-d) Representative 256 × 256 confocal images of $Alexa_{488}$-micelle aggregates, (e-h) their respective spatial autocorrelation functions and (i-n) fits, acquired at different times, after their addition to pH 7 solution ranging the final pH of 5.3. (o) Diffusion coefficients of the sample (pH=5.3) as a function of the time.

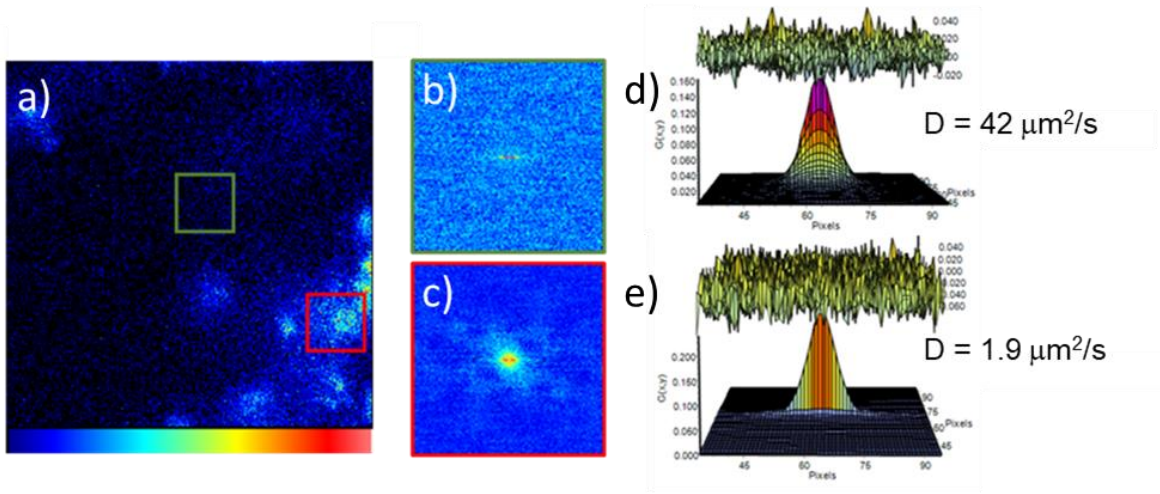

Figure 4.14. (a) Representative 256 × 256 confocal image, (b-c) the corresponding spatial autocorrelation functions of areas marked (64 × 64) and (d-e) the respective fits of 125 µL of H-c (final concentration of 36 µM) added to 375 µL solution pH 7 (final pH 5.3). 64x64 pixel ROIs can be selected and the analysis leads to D ~ 1.9 $\mu m^2/s$ in ROIs where large cluster are observed (e.g. red square) and D ~ 42 $\mu m^2/s$ in region where only sub-resolution species are present (e.g green square).

Since disassembly and reassembly phenomena are at the bases of physiological but also pathogenic processes [245] and the interaction with membranes could have cytotoxic consequences [246,247], the effect of micelle aggregates on model membranes, during the pH change from pH 2 to pH of 5.3, was studied using the same protocol as the one described in section 4.2.3.

Fig. 4.15 shows 1024x1024 pixels representative fluorescence microscopy measurement on POPC:POPG giant vesicles stained with Laurdan (magenta channel) after the addition of 36 µM micelle aggregates labelled with $Alexa_{488}$ (13 nM) (green channel), final pH of 5.3. By comparing Fig. 4.15 with Fig. 4.8, no significant differences between the effect induced on vesicles by micelles in their not aggregated (Fig. 4.8) or aggregated (Fig. 4.15) state are highlighted. In both cases protein addition leads to a dramatic change in the morphology of the membranes that appear as "flower-like" structures characterised by a lipidic core (magenta) and by the presence of lipid-protein co-aggregates in the shell (white areas).

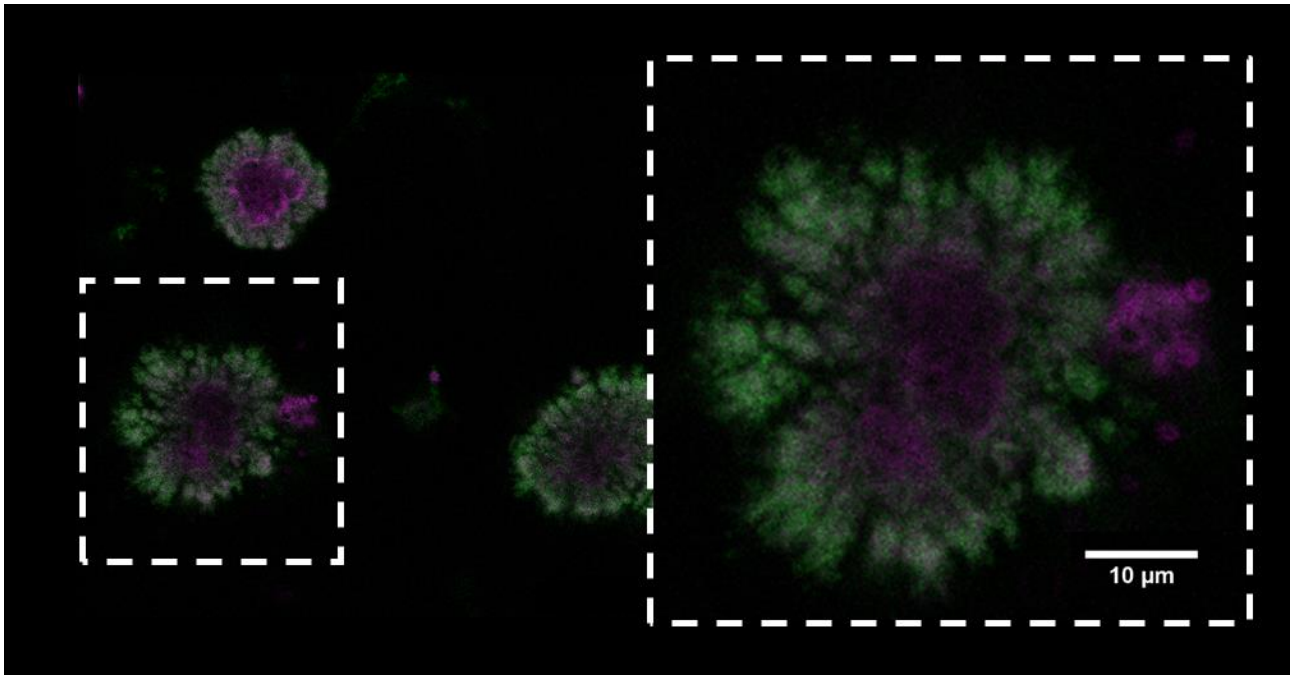

Figure 4.15. 1024 X 1024 pixels representative fluorescence image shows POPC:POPG vesicles, stained with Laurdan (magenta), after the addition of 36 µM $Alexa_{488}$-micelles aggregates. The magnification highlights the liposome where the overlap of two colors indicates protein-lipid interaction, which induces vesicles to assume a flower-like conformation.

To confirm that there were no differences between H-c and N-c effects, RICS and Laurdan measurements on vesicles in presence of micelle aggregates were performed. In this way information on the spatiotemporal dynamics of protein in presence of lipidic structures and on the

effect of protein interaction on membrane fluidity, respectively. In Fig. 4.16 (a) RICS analysis: 256 × 256 pixel size representative images of POPC:POPG GVs after the addition of 36 μM micelles aggregates containing 13 nM component of protein labelled is reported. Corresponding spatial correlation functions and fits are also shown. The colored squares represent 64 × 64 pixel ROIs where the analysis was performed. After H-c addition, immediately the vesicles appear fluorescent, that there is colocalization between membrane and fluorescently labelled protein. Since the interaction with the membranes occurs immediately, within 5 minutes, and the disaggregation process happens in the same temporal scale (Fig. 4.13 (o)), it is reasonable to think that the species responsible of the interaction with GVs could be the intermediates ones that are formed during the disaggregation-reaggregation process. It is already known that the cytotoxic effects are often attributable to oligomers [247], forming during aggregation or released from mature fibrils, thanks to small size and exposure of hydrophobic surfaces.

By analysing different ROIs in the image, we were able to discern, between freely diffusing α-casein molecule in solution away from the membrane, characterised by D of about 32 $\mu m^2/s$ and α-casein molecules in close proximity or interacting with the membrane that present D around 1 $\mu m^2/s$ indicating slower mobility of the aggregates with respect to the ones obtained by adding N-c to the sample (D~6 $\mu m^2/s$, Fig. 4.9). This different behaviour could be referred to a change of the environment, to which the proteins are exposed, in terms of hydration and packing of phospholipid bilayer. To evaluate this hypothesis, we analysed the signal of the Laurdan used to phospholipid bilayers and therefore membrane fluidity changes. The Laurdan GP variation of bulk measurements as a function of the time is reported in Fig. 4.16 (b). We observe that GVs initially in the liquid phase (GP~-0.04) go towards a progressive change in membrane fluidity to a more ordered phase[142] after α-casein aggregates addition. By comparing these data with those reported in Fig. 4.7, it is possible to highlight only a difference in the final membrane stiffening induced by the N-c (GP~0.03, Fig. 4.7) and H-c (GP~0.04) samples. However, there is a significant difference between the two samples in the interaction time with vesicles. H-c sample induces a faster increase of the GP value that reaches the stability after 30 minutes. The higher GP value, could indicate that in the final state the presence of protein leads to larger membrane dehydration resulting in more rigid membranes[142]. This could explain the lower diffusion coefficient found when H-c interacts with liposomes if compared to N-c.

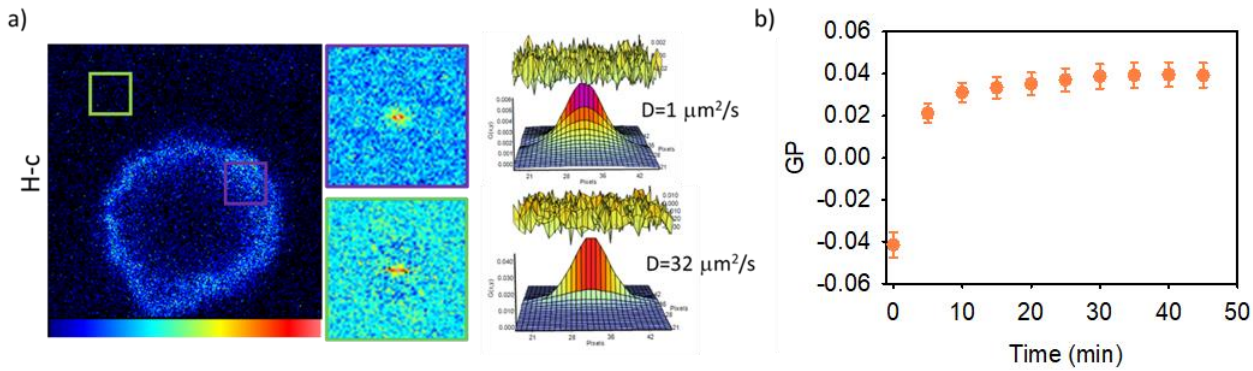

Figure 4.16. (a) RICS analysis: right column: 256 × 256 representative confocal images of liposomes interacting with 36 μM H-c labelled with Alexa488 (13 nM), in which colored squares represent 64x64 ROIs where RICS measurements are performed. Left column: spatial autocorrelation function and relative fit, spatial correlation function is marked with the same colour of the ROI in which they are calculated. (b) Time evolution of GP ratios obtained from the analysis of Laurdan fluorescence spectrum variations, measured in bulk, after the addition of H-c.

These results suggest that the released species and/or formed during the disaggregation/reaggregation processes could be different between micelles and micelles aggregates. This hypothesis was confirmed by circular dichroism measurements. Fig. 4.17 reports CD spectrum, acquired in the far-UV region, of N-c sample (already reported in Fig. 4.6) compared to the spectrum of H-c sample, both acquired at the stability after the samples are titrated at pH 5.3. An evident difference is observed between the final conformations of the two samples. The spectrum of H-c pH 5.3, that shows a minimum of ellipticity centred at around 200 nm typical of random coil structures, is significantly different from that of N-c pH 5.3 that revealed the presence of α-helix structures in the sample. The purpose of the reported spectra is to underline that although the two sample presented a comparable conformation in pH 2 (Fig. 4.11 (a)), during the pH change they undergo different structural reorganization that probably leads to the formation of diverse intermediated species responsible of the different effect induced on membranes.

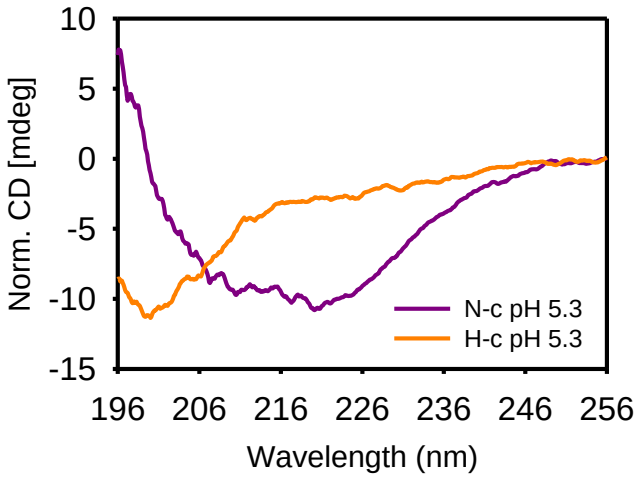

Figure 4.17. Far-UV (196-256 nm) CD spectra, normalized by absorbance, of 36 µM α-casein micelles (purple) and micelle aggregated (orange) brought at pH 5.3.

This is once again proof that the initial state of the protein critically regulates the fate of α-casein, its aggregation and effect on membrane structures.

4.3. Conclusions

The action of a protein in the cellular environment is dictated by its structure that strictly depends on environmental conditions. Among the various effects, in the organism, a protein may experience pH and temperature changes, which regulate its macromolecular properties such as the stability and activity, being these two lasts not necessarily disentangled. The comprehension of the different association/aggregation states of proteins and the evaluation of their behaviour in presence of lipid membranes are essential to elucidate the basis of functional and pathological conditions.

In this chapter α-casein protein was characterised in different association states and the effect of different molecular species were evaluated on model membranes. The results clearly put in evidence that the initial conformational/structural properties and aggregation states of the protein regulate its fate, as well as, the interaction with lipid bilayers.

The ability of α-casein to form small micelles at acidic pH was highlighted, which aggregate in larger structures at increasing temperature. In these assembly states, protein secondary structures are mainly characterised by intermolecular β-sheets. At pH 7, as expected, the protein is in its native like state, exists mostly in monomeric form with a secondary structure presenting a high content of α−helices and random coils. A main difference between α-casein at the two different pH values also consists in the interaction with the hydrophobic dyes Pyrene and ANS, being the protein at pH 2 the

one with larger affinity to both dyes. Once α-casein micelles and micelles aggregates are dissolved at pH values close to the isoelectric point in absence and in presence of membranes, micelles undergo a partial disassembly process accompanied by disordered aggregation into amorphous structures (both oligomers and large micron-scale aggregates) characterized by different final conformational states. At pH 7, the change of pH to the isoelectric point only induces slight modifications in the diffusion coefficient. Results also show that proteins initially in their micellar state or when micelles are aggregates are able to interact with the POPC:POPG GVs in liquid disordered phase. In both cases at the equilibrium the protein is found to be localised in the external part and its insertion in membrane layers is likely to exclude water, increasing the rigidity of the lipid membranes in the regions where the protein is present.

Both micelles and micelle's aggregates disassemble and result in reactive species which induce the dehydration of the lipid bilayer being micelle's aggregates impact larger and faster. This is possibly due to the different highly reactive hydrophobic species generated by the disassembly/reassembly processes that occur during the abrupt pH change which are mostly disordered in the case of aggregates micelles disassembly. These species are able to quickly interact each other forming large aggregates or to interact with membrane bilayers. Interestingly α-casein membrane co-aggregates are formed with a flower-like shape that, to our knowledge, was not previously observed in the literature as a result of protein-membrane interactions.

4.4. Sample preparation and parameters used for measurements

α-casein samples preparation

α-casein (purchased from Sigma Aldrich) was dissolved to a final concentration of 4 mg/ml in 25 mM HCl with 100 mM NaCl 0.1 M (pH 2), or in 20 mM potassium phosphate buffer (pH 7) and filtered through 0.2 µm cellulose acetate membrane filters. Furthermore, α-casein dissolved in pH 2 was subjected to heating process in a water bath at 70°C for 24 h.

Giant vesicles preparation and staining

POPC:POPG GVs were prepared with the same protocol reported in section 3.4.

Steady state fluorescence spectroscopy in bulk

Fluorescence spectra were acquired at room temperature using a Jasco-FP-8500 spectrofluorometer equipped with a Jasco ETC-815 peltier as temperature controller in 1 cm path length quartz cuvettes. The response time was 1 s, data interval of 0.5 nm and scan speed of 100

nm/min.

Pyrene emission spectra were measured in the range 350–550 nm with the excitation wavelength being 330 nm. The Pyrene concentration was 1.0 μM.

ANS emission spectra were acquired in the range 400-650 nm using λ_{exc}= 350 nm with an excitation bandwidth of 5 nm, an emission bandwidth of 5 nm. The ANS concentration was 9.0 μM.

Laurdan fluorescence emission spectra were acquired in the range 370–650 nm as a function of time every 5 minutes. Excitation wavelength was λ_{exc} = 380 nm and excitation and emission bandwidth was 5 nm.

Confocal laser scanning fluorescence microscopy (CLSM)

Confocal fluorescence microscopy measurements, reported in this thesis, were acquired using a 63×/1.4 oil objective (Leica Microsystems, Wetzlar, Germany) and a Leica TSC SP5 confocal laser scanning microscope. Scanning frequency was 400 Hz.

$Alexa_{488}$ emission was acquired in the range 510-600 nm, using λ_{exc} = 488 nm.

Two-photon microscopy

Laurdan emission was acquired in the range 430-450 nm (blue channel) and in the range 475-495 nm (green channel) using 2-photon excitation (Spectra-Physics Mai-Tai Ti:Sa ultra-fast laser), at 780 nm.

Raster Image Correlation Spectroscopy (RICS)

Images were acquired in single channel with an Olympus FluoView1200 confocal laser scanning microscope (Olympus, Tokyo, Japan) using an UPLSAPO 60 × 1.2 NA objective using chambered cover gasses (Lab-Teck II Nunc). For RICS analysis, 70 frame image stacks were acquired (256 × 256 pixels) at different dwell time of 8, 10, 12.5, 20 μs/pixel. The electronic zoom was set at ×16.3 (pixel size of 0.05 μm). Analysis was performed using the RICS algorithm of SimFCS program. RICS autocorrelation function has been fitted using the diffusion model to calculate G_0 and D. The excitation volume was calibrated by using a solution of $Alexa_{488}$ in water containing and setting the diffusion coefficient to 350 $\mu m^2/s$. For this measurement, the dwell time was reduced to 4 μs/pixel. In the cases where large species are evident in the RICS measurements, immobile subtraction algorithm was used to eliminate the contribution of fluctuations due to these species, which are found in the same position for several time frames. The Moving Average (MAV) algorithm of SimFCS was used and the length of the MAV was optimized to the larger number of frames until the calculated autocorrelation function remained the same. This procedure was aimed at eliminating the contribution of immobile species.

Circular dichroism

The CD spectra were recorded on a Jasco J-715 spectropolarimeter in the far-UV region (194–260 nm), using quartz cuvettes with a path length of 0.5 mm. All spectra have been acquired at room temperature and for each spectrum, three accumulations have been acquired.

5. Conclusions and perspectives

The aim of this work was to understand how membranes and proteins act under diverse biological conditions, elucidating the forces that drive the interaction between them and the effects induced by the interaction both on conformation/aggregation states of proteins, and morphology and physical-chemical properties of membranes.

To carry out this study, it was first analysed how membrane composition influences and regulates the interaction of the small, cationic, amphiphilic TP10 peptide. Diverse model membranes, extremely different in term of phospholipid bilayer complexity and inner composition, were used. The interaction between the peptide and POPC:POPG GVs, POPC:POPG:Chol GVs and GPMVs derived by HepG2 cell line was evaluated by the combined use of spectroscopic and advanced microscopy techniques. The results have demonstrated that the interactions between TP10 and membranes result in mutually structural perturbations of both the peptide and the membranes. On one hand, membrane surfaces, depending on their chemical composition, can promote the conformational change of the peptide. On the other hand, TP10, depending on membrane composition, can modify membranes physical-chemical properties and disrupt membrane structural integrity. Thanks to the parallel use of multiple targeted molecular reporters and FLIM/phasor analysis it was in fact possible to distinguish TP10 absorption from insertion, evaluate its effect on membrane hydration and fluidity, and its ability to form pores, modifying or not membrane morphology and integrity. The presented results demonstrated that FLIM is an excellent, non invasive technique for highlighting at single vesicle level and in 3 dimensions diverging aspects of such multi-faceted complex phenomenon as peptide-membrane interaction.

The second part of the work aimed to analyse the effect of different association/aggregation states, obtained varying environmental conditions (such as pH and temperature), of the α-casein on the simplest POPC:POPG model membranes, in order to elucidate the basis of functional and pathological conditions. α-casein presents highly different features in term of exposed charges, hydrophobicity, size and structural complexity, if compared with TP10.

Also in this case spectroscopic techniques were used to carry out the study but coupled with RICS technique. This method gave the possibility to analyze the aggregation states (monomers, micelles, and micellar aggregates) of the protein in different environmental conditions and to follow in real time the disaggregation and re-aggregation processes of micellar aggregates induced by pH changes. The species formed during this disaggregation/aggregation process were considered the

responsible of the interaction with membranes. RICS was also useful to evaluate the different interaction level of them with the bilayers, also monitoring the morphological modifications affecting the membranes. The results clearly indicated that the initial conformational and aggregation states of the protein regulate its fate and that the interaction with lipid bilayers induces the formation of protein membrane co-aggregates with a flower-like shape not previously observed in the literature, as a result of protein-membrane interactions. The global view of the results suggested that electrostatic and hydrophobic interactions are the main forces involved in the protein-membrane interaction and that, by using appropriate dyes and combining spectroscopy and quantitative fluorescence microscopy, it is possible to disentangle the different processes involved in these highly dynamic and heterogeneous processes. Nevertheless, it is not clear which are the factors that lead to an increase of GPMVs fluidity after TP10 interaction. It has in fact been observed that bothTP10 and *α*-casein induce dehydration and stiffening of POPC:POPG GVs. The opposite behavior observed for GPMVs could be ascribed to the highly different membrane composition in term of lipids and proteins. Based on the literature[112] it was reasonable to think that cholesterol played a key role. It had been observed that *α*-syn induces cholesterol depletion from vesicles, resulting in the formation of protein-cholesterol aggregates and increase of the disordered phase in the bilayers. However, this hypothesis would appear to be excluded from the experiments performed on POPC:POPG:Chol GVs since no interaction was observed between TP10 and these membranes. Further, previous research[248,249] directly performed on GPMVs enriched or depleted of cholesterol have shown similar results. It was also discovered that the accumulation of TP10 into GPMVs is inhibited by ceramide possibly due to the formation of highly ordered ceramide platforms that, interfering with the fluidity of the membrane, reduce the uptake of the peptide[248]. Therefore, the reason for the different behaviour should be sought elsewhere.

In addition, preliminary experiments (not reported in this thesis) performed using GPMVs derived from fibroblasts and TP10 revealed that the peptide is also able to interact with these vesicles, modifying or not their morphology and integrity depending on peptide concentration. Fibroblasts are mesenchymal cells that synthesize the extracellular matrix of connective tissue but play a key role in diseases, cancer progression[250,251] and inflammatory[252] and fibrotic conditions. For example, in inflammatory diseases such as rheumatoid arthritis, it is now known that fibroblasts are the key cellular source of inflammatory cytokines and chemokines that enable chronic tissue inflammation. There are biological therapies (e.g., tocilizumab, targeting IL-6 receptor) that block fibroblast-derived cytokines, relieving symptoms and slowing the disease but not able to eradicate it;

moreover, currently there are no FDA-approved therapies that directly target fibroblasts in inflammatory diseases. Yet several hypotheses suggest targeting of fibroblasts. First, although targeting immune cells in inflammatory disease inevitably compromises the immune response to infections, targeting stromal cells may circumvent immunosuppression while abrogating pathology in the involved tissues. Second, fibroblast-targeted therapy may represent an alternative strategy for patients resistant to conventional immunosuppressive therapies. In this scenario, the action of TP10 against fibroblast, in addition to its ability (shared also with other CPPs[253,254]) to decrease inflammatory cytokine release[255], could pave the way for new therapies.

In addition, the possibility to obtain vesicles, in a simple way, from normal cells could be of great interest in drug delivery[256,257], exploiting the natural targeting properties[258,259] of the vesicles and, due to their natural composition, resulting to be less immunogenic than artificial nanoparticulate carriers. In conclusion, the presented approach could be directly applicable to various biological systems in studies facing the challenge of analysing peptide/protein membrane interactions and representing a significant technical advancement applicable for a wide experimental field including studies of both functional (e.g., protein trafficking, cellular signalling, and ion channel formation) and pathological (e.g., amyloid membrane toxic interactions) phenomena.

Bibliography

1. Protein Function - Molecular Biology of the Cell - NCBI Bookshelf. https://www.ncbi.nlm.nih.gov/books/NBK26911/.
2. Nelson, D. L. (David L., Cox, M. M. & Lehninger, A. L. Lehninger principles of biochemistry. 45.
3. Finkelstein, A. v. & Ptitsyn, O. B. (Oleg B. Protein physics. 530.
4. Dill, K. A. Dominant Forces in Protein Folding. *Biochemistry* **29**, 7133–7155 (1990).
5. Baldwin, R. L. Dynamic hydration shell restores Kauzmann's 1959 explanation of how the hydrophobic factor drives protein folding. *Proc Natl Acad Sci U S A* **111**, 13052 (2014).
6. Chandler, D. Interfaces and the driving force of hydrophobic assembly. *Nature 2005 437:7059* **437**, 640–647 (2005).
7. Némethy, G., Steinberg, I. Z. & Scheraga, H. A. Influence of water structure and of hydrophobic interactions on the strength of side-chain hydrogen bonds in proteins. *Biopolymers* **1**, 43–69 (1963).
8. Jahn, T. R. & Radford, S. E. The Yin and Yang of protein folding. *FEBS J* **272**, 5962–5970 (2005).
9. Dobson, C. M. Protein folding and misfolding. *Nature* **426**, 884–890 (2003).
10. Balchin, D., Hayer-Hartl, M. & Hartl, F. U. In vivo aspects of protein folding and quality control. *Science (1979)* **353**, (2016).
11. Dill, K. A. & Chan, H. S. From levinthal to pathways to funnels. *Nat Struct Biol* **4**, 10–19 (1997).
12. Sunde, M., chemistry, C. B.-A. in protein & 1997, undefined. The structure of amyloid fibrils by electron microscopy and X-ray diffraction. *Elsevier*.
13. Petkova, A. T. *et al.* A structural model for Alzheimer's β-amyloid fibrils based on experimental constraints from solid state NMR. *Proc Natl Acad Sci U S A* **99**, 16742–16747 (2002).
14. Thirumalai, D. & Reddy, G. Protein thermodynamics: Are native proteins metastable? *Nat Chem* **3**, 910–911 (2011).
15. Baldwin, A. J. *et al.* Metastability of native proteins and the phenomenon of amyloid formation. *J Am Chem Soc* **133**, 14160–14163 (2011).
16. di Carlo, M. G. *et al.* Trifluoroethanol modulates α-synuclein amyloid-like aggregate formation, stability and dissolution. *Biophys Chem* **216**, 23–30 (2016).
17. Foderà, V., Zaccone, A., Lattuada, M. & Donald, A. M. Electrostatics controls the formation of amyloid superstructures in protein aggregation. *Phys Rev Lett* **111**, (2013).
18. Vetri, V. & Foderà, V. The route to protein aggregate superstructures: Particulates and amyloid-like spherulites. *FEBS Lett* **589**, 2448–2463 (2015).
19. Anselmo, S., Sancataldo, G., Foderà, V. & Vetri, V. α-casein micelles-membranes interaction: Flower-like lipid protein coaggregates formation. *Biochim Biophys Acta Gen Subj* 130196 (2022) doi:10.1016/J.BBAGEN.2022.130196.
20. Galdiero, S. *et al.* Peptide-Lipid Interactions: Experiments and Applications. *Int J Mol Sci* **14**, 18758 (2013).

21. Zwaal, R. F. A., Comfurius, P. & Bevers, E. M. Lipid–protein interactions in blood coagulation. *Biochimica et Biophysica Acta (BBA) - Reviews on Biomembranes* **1376**, 433–453 (1998).

22. Christie, S., Shi, X. & Smith, A. W. Resolving Membrane Protein-Protein Interactions in Live Cells with Pulsed Interleaved Excitation Fluorescence Cross-Correlation Spectroscopy. *Acc Chem Res* **53**, 792–799 (2020).

23. Wang, H. & Li, G. Membrane biophysics: New insights and methods. *Membrane Biophysics: New Insights and Methods* 1–421 (2017) doi:10.1007/978-981-10-6823-2/COVER.

24. van Uitert, I., le Gac, S. & van den Berg, A. The influence of different membrane components on the electrical stability of bilayer lipid membranes. *Biochimica et Biophysica Acta (BBA) - Biomembranes* **1798**, 21–31 (2010).

25. Renne, M. F. & de Kroon, A. I. P. M. The role of phospholipid molecular species in determining the physical properties of yeast membranes. *FEBS Lett* **592**, 1330 (2018).

26. de Meyer, F. & Smit, B. Effect of cholesterol on the structure of a phospholipid bilayer. *Proc Natl Acad Sci U S A* **106**, 3654–3658 (2009).

27. Ballweg, S. *et al.* Regulation of lipid saturation without sensing membrane fluidity. *Nature Communications 2020 11:1* **11**, 1–13 (2020).

28. Baylis, P. H. Water movement through lipid bilayers, pores and plasma membranes: Theory and reality. . *Cell Biochem Funct* **6**, 223–223 (1988).

29. Lande, M. B., Donovan, J. M. & Zeidel, M. L. The relationship between membrane fluidity and permeabilities to water, solutes, ammonia, and protons. *Journal of General Physiology* **106**, 67–84 (1995).

30. Sameni, S., Malacrida, L., Tan, Z. & Digman, M. A. Alteration in Fluidity of Cell Plasma Membrane in Huntington Disease Revealed by Spectral Phasor Analysis. *Sci Rep* **8**, (2018).

31. Jourd'heuil, D., Aspinall, A., Reynolds, J. D. & Meddings, J. B. Membrane fluidity increases during apoptosis of sheep ileal Peyer's patch B cells. *Can J Physiol Pharmacol* **74**, 706–711 (1996).

32. Gibbons, E. *et al.* Molecular Details of Membrane Fluidity Changes during Apoptosis and Relationship to Phospholipase A2 Activity. *Biochim Biophys Acta* **1828**, 887 (2013).

33. Vetri, V. *et al.* Fluctuation Methods To Study Protein Aggregation in Live Cells: Concanavalin A Oligomers Formation. *Biophys J* **100**, 774–783 (2011).

34. Wu, Y. *et al.* Molecular rheometry: direct determination of viscosity in Lo and Ld lipid phases via fluorescence lifetime imaging. *Physical Chemistry Chemical Physics* **15**, 14986–14993 (2013).

35. Dal Molin, M. *et al.* Fluorescent flippers for mechanosensitive membrane probes. *J Am Chem Soc* **137**, 568–571 (2015).

36. Klymchenko, A. S. Solvatochromic and Fluorogenic Dyes as Environment-Sensitive Probes: Design and Biological Applications. *Acc Chem Res* **50**, 366–375 (2017).

37. Danylchuk, D. I., Sezgin, E., Chabert, P. & Klymchenko, A. S. Redesigning Solvatochromic Probe Laurdan for Imaging Lipid Order Selectively in Cell Plasma Membranes. *Anal Chem* **92**, 14798–14805 (2020).

38. Yeaman, M. R. & Yount, N. Y. Mechanisms of antimicrobial peptide action and resistance. *Pharmacol Rev* **55**, 27–55 (2003).

39. Lai, Y. & Gallo, R. L. AMPed up immunity: how antimicrobial peptides have multiple roles in immune defense. *Trends Immunol* **30**, 131–141 (2009).

40. Johnson, J. E. & Cornell, R. B. Amphitropic proteins: regulation by reversible membrane interactions (review). *Mol Membr Biol* **16**, 217–235 (1999).

41. Burn, P. Talking point Amphitropic proteins: a new class of membrane proteins. *Trends Biochem Sci* **13**, 79–83 (1988).

42. Rødland, I., Halskau, Ø., Martínez, A. & Holmsen, H. α-Lactalbumin binding and membrane integrity—effect of charge and degree of unsaturation of glycerophospholipids. *Biochimica et Biophysica Acta (BBA) - Biomembranes* **1717**, 11–20 (2005).

43. Barbana, C. & Pérez, M. D. Interaction of α-lactalbumin with lipids and possible implications for its emulsifying properties - A review. *Int Dairy J* **21**, 727–741 (2011).

44. Casey, J. R., Grinstein, S. & Orlowski, J. Sensors and regulators of intracellular pH. *Nature Reviews Molecular Cell Biology 2009 11:1* **11**, 50–61 (2009).

45. Heimburg, T., Marsh, D. & Hildebrandt, P. Cytochrome c-lipid interactions studied by resonance Raman and 31P NMR spectroscopy. Correlation between the conformational changes of the protein and the lipid bilayer. *Biochemistry* **30**, 9084–9089 (1991).

46. Anselmo, S., Sancataldo, G., Mørck Nielsen, H., Foderà, V. & Vetri, V. Peptide-Membrane Interactions Monitored by Fluorescence Lifetime Imaging: A Study Case of Transportan 10. *Langmuir* **37**, 13148–13159 (2021).

47. Rao, E., Foderà, V., Leone, M. & Vetri, V. Direct observation of alpha-lactalbumin, adsorption and incorporation into lipid membrane and formation of lipid/protein hybrid structures. *Biochim Biophys Acta Gen Subj* **1863**, 784–794 (2019).

48. van Maarschalkerweerd, A., Vetri, V., Langkilde, A. E., Foderà, V. & Vestergaard, B. Protein/lipid coaggregates are formed during α-synuclein-induced disruption of lipid bilayers. *Biomacromolecules* **15**, 3643–3654 (2014).

49. Gong, Z., Ikonomova, S. P. & Karlsson, A. J. Secondary structure of cell-penetrating peptides during interaction with fungal cells. *Protein Science* **27**, 702–713 (2018).

50. Avitabile, C., D'Andrea, L. D. & Romanelli, A. Circular Dichroism studies on the interactions of antimicrobial peptides with bacterial cells. *Scientific Reports 2014 4:1* **4**, 1–7 (2014).

51. Bañuelos, S. & Muga, A. Binding of molten globule-like conformations to lipid bilayers. Structure of native and partially folded alpha-lactalbumin bound to model membranes. *J Biol Chem* **270**, 29910–29915 (1995).

52. Zhang, X., Ge, N. & Keiderling, T. A. Electrostatic and Hydrophobic Interactions Governing the Interaction and Binding of β-Lactoglobulin to Membranes†. *Biochemistry* **46**, 5252–5260 (2007).

53. Kanwa, N., De, S. K., Maity, A. & Chakraborty, A. Interaction of aliphatic amino acids with zwitterionic and charged lipid membranes: Hydration and dehydration phenomena. *Physical Chemistry Chemical Physics* **22**, 3234–3244 (2020).

54. Bárány-Wallje, E., Gaur, J., Lundberg, P., Langel, Ü. & Gräslund, A. Differential membrane perturbation caused by the cell penetrating peptide Tp10 depending on attached cargo. *FEBS Lett* **581**, 2389–2393 (2007).

55. Sharmin, S. *et al.* Effects of Lipid Composition on the Entry of Cell-Penetrating Peptide Oligoarginine into Single Vesicles. *Biochemistry* **55**, 4154–4165 (2016).

56. Halskau, Ø., Frøystein, N. Å., Muga, A. & Martínez, A. The Membrane-bound Conformation of α-Lactalbumin Studied by NMR-monitored 1H Exchange. *J Mol Biol* **321**, 99–110 (2002).

57. Stefani, M. & Dobson, C. M. Protein aggregation and aggregate toxicity: New insights into protein folding, misfolding diseases and biological evolution. *J Mol Med* **81**, 678–699 (2003).

58. Stefani, M. Biochemical and biophysical features of both oligomer/fibril and cell membrane in amyloid cytotoxicity. *FEBS J* **277**, 4602–4613 (2010).

59. Butterfield, S. M. & Lashuel, H. A. Amyloidogenic Protein–Membrane Interactions: Mechanistic Insight from Model Systems. *Angewandte Chemie International Edition* **49**, 5628–5654 (2010).

60. Bucciantini, M., Rigacci, S. & Stefani, M. Amyloid aggregation: Role of biological membranes and the aggregate-membrane system. *Journal of Physical Chemistry Letters* **5**, 517–527 (2014).

61. Chiti, F. & Dobson, C. M. Protein Misfolding, Functional Amyloid, and Human Disease. *http://dx.doi.org/10.1146/annurev.biochem.75.101304.123901* **75**, 333–366 (2006).

62. Gonzalez-Garcia, M., Fusco, G. & de Simone, A. Membrane Interactions and Toxicity by Misfolded Protein Oligomers. *Front Cell Dev Biol* **9**, 395 (2021).

63. Winner, B. *et al.* In vivo demonstration that α-synuclein oligomers are toxic. *Proc Natl Acad Sci U S A* **108**, 4194–4199 (2011).

64. Fusco, G. *et al.* Structural basis of membrane disruption and cellular toxicity by a-synuclein oligomers. *Science (1979)* **358**, 1440–1443 (2017).

65. Shahnawaz, M. & Soto, C. Microcin amyloid fibrils A are reservoir of toxic oligomeric species. *Journal of Biological Chemistry* **287**, 11665–11676 (2012).

66. Bemporad, F. & Chiti, F. Protein Misfolded Oligomers: Experimental Approaches, Mechanism of Formation, and Structure-Toxicity Relationships. *Chem Biol* **19**, 315–327 (2012).

67. Zamotin, V. *et al.* Cytotoxicity of albebetin oligomers depends on cross-β-sheet formation. *FEBS Lett* **580**, 2451–2457 (2006).

68. Walsh, D., letters, D. S.-P. and peptide & 2004, undefined. Oligomers on the brain: the emerging role of soluble protein aggregates in neurodegeneration. *ingentaconnect.com*.

69. Meier, J. J. *et al.* Inhibition of human IAPP fibril formation does not prevent β-cell death: Evidence for distinct actions of oligomers and fibrils of human IAPP. *Am J Physiol Endocrinol Metab* **291**, (2006).

70. Mclean, C. A. *et al.* Soluble Pool of A Amyloid as a Determinant of Severity of Neurodegeneration in Alzheimer's Disease. (1999) doi:10.1002/1531-8249.

71. Butterfield, S. M. & Lashuel, H. A. Amyloidogenic protein-membrane interactions: Mechanistic insight from model systems. *Angewandte Chemie - International Edition* **49**, 5628–5654 (2010).

72. Gao, Q., Wu, G. & Lai, K. W. C. Cholesterol Modulates the Formation of the Aβ Ion Channel in Lipid Bilayers. *Biochemistry* **59**, 992–998 (2020).

73. Yip, C. M., Elton, E. A., Darabie, A. A., Morrison, M. R. & Mclaurin, J. Cholesterol, a modulator of membrane-associated aβ-fibrillogenesis and neurotoxicity. *J Mol Biol* **311**, 723–734 (2001).

74. Kakio, A., Nishimoto, S. ichi, Yanagisawa, K., Kozutsumi, Y. & Matsuzaki, K. Interactions of amyloid β-protein with various gangliosides in raft-like membranes: Importance of GM1 ganglioside-bound form as an endogenous seed for Alzheimer amyloid. *Biochemistry* **41**, 7385–7390 (2002).

75. Milanesi, L. *et al.* Direct three-dimensional visualization of membrane disruption by amyloid fibrils. *Proc Natl Acad Sci U S A* **109**, 20455–20460 (2012).

76. Kastorna, A., Trusova, V., Gorbenko, G. & Kinnunen, P. Chemistry and Physics of Lipids Membrane effects of lysozyme amyloid fibrils. *Chem Phys Lipids* **165**, 331–337 (2012).

77. Sciacca, M. F. *et al.* Lipid-Chaperone Hypothesis: A Common Molecular Mechanism of Membrane Disruption by Intrinsically Disordered Proteins. *Cite This: ACS Chem. Neurosci* **11**, 4350 (2020).

78. Tempra, C., Scollo, F., Pannuzzo, M., Lolicato, F. & la Rosa, C. A unifying framework for amyloid-mediated membrane damage: The lipid-chaperone hypothesis. *Biochimica et Biophysica Acta (BBA) - Proteins and Proteomics* **1870**, 140767 (2022).

79. Skamris, T., Marasini, C., Madsen, K. L., Foderà, V. & Vestergaard, B. Early Stage Alpha-Synuclein Amyloid Fibrils are Reservoirs of Membrane-Binding Species. *Scientific Reports 2019 9:1* **9**, 1–11 (2019).

80. Hebda, J. A. & Miranker, A. D. The interplay of catalysis and toxicity by amyloid intermediates on lipid bilayers: Insights from type II diabetes. *Annu Rev Biophys* **38**, 125–152 (2009).

81. Chiti, F. & Dobson, C. M. Protein misfolding, functional amyloid, and human disease. *Annu Rev Biochem* **75**, 333–366 (2006).

82. Williamson, J. A., Loria, J. P. & Miranker, A. D. Helix Stabilization Precedes Aqueous and Bilayer-Catalyzed Fiber Formation in Islet Amyloid Polypeptide. *J Mol Biol* **393**, 383–396 (2009).

83. Martins, I. C. *et al.* Lipids revert inert Abeta amyloid fibrils to neurotoxic protofibrils that affect learning in mice. *EMBO J* **27**, 224–233 (2008).

84. Kiuchi, Y., Isobe, Y., Fukushima, K. & Kimura, M. Disassembly of amyloid β-protein fibril by basement membrane components. *Life Sci* **70**, 2421–2431 (2002).

85. Castillo, G. M. *et al.* Laminin Inhibition of-Amyloid Protein (A) Fibrillogenesis and Identification of an A Binding Site Localized to the Globular Domain Repeats on the Laminin A Chain. (2000) doi:10.1002/1097-4547.

86. Karpiński, T. M. & Adamczak, A. Anticancer Activity of Bacterial Proteins and Peptides. *Pharmaceutics* **10**, (2018).

87. Mahlapuu, M., Håkansson, J., Ringstad, L. & Björn, C. Antimicrobial peptides: An emerging category of therapeutic agents. *Front Cell Infect Microbiol* **6**, 194 (2016).

88. Snyder, E. L. & Dowdy, S. F. Cell Penetrating Peptides in Drug Delivery. (2004).

89. pharmacology, M. L.-C. opinion in & 2002, undefined. Peptide-mediated cell delivery: application in protein target validation. *Elsevier*.

90. Fischer, P. M., Krausz, E. & Lane, D. P. Cellular delivery of impermeable effector molecules in the form of conjugates with peptides capable of mediating membrane translocation. *Bioconjug Chem* **12**, 825–841 (2001).

91. Svensson, M. *et al.* α-Lactalbumin unfolding is not sufficient to cause apoptosis, but is required for the conversion to HAMLET (human α-lactalbumin made lethal to tumor cells). *Protein Science* **12**, 2794–2804 (2003).

92. Oliver, W. T. & Wells, J. E. Lysozyme as an alternative to growth promoting antibiotics in swine production. *J Anim Sci Biotechnol* **6**, (2015).

93. Zhang, Q. Y. *et al.* Antimicrobial peptides: mechanism of action, activity and clinical potential. *Military Medical Research 2021 8:1* **8**, 1–25 (2021).

94. Huan, Y., Kong, Q., Mou, H. & Yi, H. Antimicrobial Peptides: Classification, Design, Application and Research Progress in Multiple Fields. *Front Microbiol* **11**, 582779 (2020).

95. Chen, X. *et al.* Cellular Physiology and Biochemistry Cellular Physiology and Biochemistry Roles and Mechanisms of Human Cathelicidin LL-37 in Cancer. *Cell Physiol Biochem* **47**, 1060–1073 (2018).

96. Cheng, M. *et al.* Cathelicidin suppresses colon cancer development by inhibition of cancer associated fibroblasts. *Clin Exp Gastroenterol* **8**, 13 (2015).

97. Sandgren, S. *et al.* The human antimicrobial peptide LL-37 transfers extracellular DNA plasmid to the nuclear compartment of mammalian cells via lipid rafts and proteoglycan-dependent endocytosis. *J Biol Chem* **279**, 17951–17956 (2004).

98. Said Hassane, F., Saleh, A. F., Abes, R., Gait, M. J. & Lebleu, B. Cell penetrating peptides: overview and applications to the delivery of oligonucleotides. *Cell Mol Life Sci* **67**, 715–726 (2010).

99. Bahnsen, J. S., Franzyk, H., Sandberg-Schaal, A. & Nielsen, H. M. Antimicrobial and cell-penetrating properties of penetratin analogs: Effect of sequence and secondary structure. *Biochimica et Biophysica Acta (BBA) - Biomembranes* **1828**, 223–232 (2013).

100. Moretta, A. *et al.* Antimicrobial Peptides: A New Hope in Biomedical and Pharmaceutical Fields. *Front Cell Infect Microbiol* **11**, 453 (2021).

101. Routledge, S. J., Linney, J. A. & Goddard, A. D. Liposomes as models for membrane integrity. *Biochem Soc Trans* **47**, 919–932 (2019).

102. Peschel, A. How do bacteria resist human antimicrobial peptides? *Trends Microbiol* **10**, 179–186 (2002).

103. Shai, Y. Mechanism of the binding, insertion and destabilization of phospholipid bilayer membranes by alpha-helical antimicrobial and cell non-selective membrane-lytic peptides. *Biochim Biophys Acta* **1462**, 55–70 (1999).

104. Peetla, C., Stine, A. & Labhasetwar, V. Biophysical interactions with model lipid membranes: applications in drug discovery and drug delivery. *Mol Pharm* **6**, 1264–1276 (2009).

105. Drazenovic, J. *et al.* Effect of lamellarity and size on calorimetric phase transitions in single component phosphatidylcholine vesicles. *Biochimica et Biophysica Acta (BBA) - Biomembranes* **1848**, 532–543 (2015).

106. Yamazaki, M. The Single GUV Method for Probing Biomembrane Dynamics.

107. Tamba, Y. & Yamazaki, M. Single giant unilamellar vesicle method reveals effect of antimicrobial peptide magainin 2 on membrane permeability. *Biochemistry* **44**, 15823–15833 (2005).

108. Islam, M. Z., Sharmin, S., Moniruzzaman, M. & Yamazaki, M. Elementary processes for the entry of cell-penetrating peptides into lipid bilayer vesicles and bacterial cells. *Appl Microbiol Biotechnol* **102**, 3879–3892 (2018).

109. Islam, M. Z., Alam, J. M., Tamba, Y., Karal, M. A. S. & Yamazaki, M. The single GUV method for revealing the functions of antimicrobial, pore-forming toxin, and cell-penetrating peptides or proteins. *Physical Chemistry Chemical Physics* **16**, 15752–15767 (2014).

110. Moghal, M. M. R., Shuma, M. L., Islam, M. Z. & Yamazaki, M. A Single GUV Method for Revealing the Action of Cell-Penetrating Peptides in Biomembranes. *Methods in Molecular Biology* **2383**, 167–179 (2022).

111. Tayebi, L., Vashaee, D. & Parikh, A. N. Stability of Uni- and Multillamellar Spherical Vesicles. *ChemPhysChem* **13**, 314–322 (2012).

112. van Maarschalkerweerd, A., Vetri, V. & Vestergaard, B. Cholesterol facilitates interactions between α-synuclein oligomers and charge-neutral membranes. *FEBS Lett* **589**, 2661–2667 (2015).

113. Sezgin, E. *et al.* Elucidating membrane structure and protein behavior using giant plasma membrane vesicles. *Nature Protocols 2012 7:6* **7**, 1042–1051 (2012).

114. Einfalt, T. *et al.* Bioinspired Molecular Factories with Architecture and In Vivo Functionalities as Cell Mimics. *Adv Sci (Weinh)* **7**, (2020).

115. Scott, R. E. Plasma Membrane Vesiculation: A New Technique for Isolation of Plasma Membranes. *Science (1979)* **194**, 743–745 (1976).

116. Sezgin, E. Giant plasma membrane vesicles to study plasma membrane structure and dynamics. *Biochimica et Biophysica Acta (BBA) - Biomembranes* **1864**, 183857 (2022).

117. Zartner, L., Garni, M., Craciun, I., Einfalt, T. & Palivan, C. G. How Can Giant Plasma Membrane Vesicles Serve as a Cellular Model for Controlled Transfer of Nanoparticles? *Biomacromolecules* **22**, 106–115 (2021).

118. Lakowicz, J. R. Principles of fluorescence spectroscopy. *Principles of Fluorescence Spectroscopy* 1–954 (2006) doi:10.1007/978-0-387-46312-4/COVER.

119. Akbar, S. M. D., Sreeramulu, K. & Sharma, H. C. Tryptophan fluorescence quenching as a binding assay to monitor protein conformation changes in the membrane of intact mitochondria. *J Bioenerg Biomembr* **48**, 241–247 (2016).

120. Möller, M. & Denicola, A. Protein tryptophan accessibility studied by fluorescence quenching. *Biochemistry and Molecular Biology Education* **30**, 175–178 (2002).

121. Willem Borst, J. & Visser, A. J. W. G. Fluorescence lifetime imaging microscopy in life sciences. *Meas Sci Technol* **21**, 102002 (2010).

122. Agnello, Simonpietro. Spectroscopy for materials characterization. (2021).

123. Sanderson, M. J., Smith, I., Parker, I. & Bootman, M. D. Fluorescence Microscopy. *Cold Spring Harb Protoc* **2014**, pdb.top071795 (2014).

124. Datta, R., Heaster, T. M., Sharick, J. T., Gillette, A. A. & Skala, M. C. Fluorescence lifetime imaging microscopy: fundamentals and advances in instrumentation, analysis, and applications. *J Biomed Opt* **25**, 1 (2020).

125. Digman, M. A., Caiolfa, V. R., Zamai, M. & Gratton, E. The Phasor Approach to Fluorescence Lifetime Imaging Analysis. *Biophys J* **94**, L14–L16 (2008).

126. Phasor Analysis for FLIM (Fluorescence Lifetime Imaging Microscopy) | Science Lab | Leica Microsystems. https://www.leica-microsystems.com/science-lab/phasor-analysis-for-flim-fluorescence-lifetime-imaging-microscopy/?tx_leicacontacts_pi1%5Bcontroller%5D=Contacts&tx_leicacontacts_pi1%5Bcountry%5D=BR&cHash=0b6dac9bd58a4dce9e027539e7da41a7.

127. Rossow, M. J., Sasaki, J. M., Digman, M. A. & Gratton, E. Raster image correlation spectroscopy in live cells. *Nat Protoc* **5**, 1761 (2010).

128. Brown, C. M. *et al.* Raster image correlation spectroscopy (RICS) for measuring fast protein dynamics and concentrations with a commercial laser scanning confocal microscope. *J Microsc* **229**, 78–91 (2008).

129. Digman, M. A. & Gratton, E. Analysis of diffusion and binding in cells using the RICS approach. *Microsc Res Tech* **72**, 323 (2009).

130. Mikuni, S., Yamamoto, J., Horio, T. & Kinjo, M. Negative Correlation between the Diffusion Coefficient and Transcriptional Activity of the Glucocorticoid Receptor. *International Journal of Molecular Sciences 2017, Vol. 18, Page 1855* **18**, 1855 (2017).

131. Digman, M. A. *et al.* Measuring Fast Dynamics in Solutions and Cells with a Laser Scanning Microscope. *Biophys J* **89**, 1317–1327 (2005).

132. Hawe, A., Sutter, M. & Jiskoot, W. Extrinsic fluorescent dyes as tools for protein characterization. *Pharm Res* **25**, 1487–1499 (2008).

133. Klonis, N., Clayton, A. H. A., Voss, E. W. & Sawyer, W. H. Spectral Properties of Fluorescein in Solvent-Water Mixtures: Applications as a Probe of Hydrogen Bonding Environments in Biological Systems. *Photochem Photobiol* **67**, 500–510 (1998).

134. Arrabito, G. *et al.* Printing Life-Inspired Subcellular Scale Compartments with Autonomous Molecularly Crowded Confinement. *Adv Biosyst* **3**, 1900023 (2019).

135. Oshinbolu, S. *et al.* Evaluation of fluorescent dyes to measure protein aggregation within mammalian cell culture supernatants. *Journal of Chemical Technology and Biotechnology* **93**, 909 (2018).

136. Basu Ray, G., Chakraborty, I. & Moulik, S. P. Pyrene absorption can be a convenient method for probing critical micellar concentration (cmc) and indexing micellar polarity. *J Colloid Interface Sci* **294**, 248–254 (2006).

137. Liu, Y. & Guo, R. pH-dependent structures and properties of casein micelles. *Biophys Chem* **136**, 67–73 (2008).

138. Demchenko, A. P., Mély, Y., Duportail, G. & Klymchenko, A. S. Monitoring Biophysical Properties of Lipid Membranes by Environment-Sensitive Fluorescent Probes. *Biophys J* **96**, 3461–3470 (2009).

139. García, J. J. *et al.* Effects of trace elements on membrane fluidity. *Journal of Trace Elements in Medicine and Biology* **19**, 19–22 (2005).

140. Amaro, M., Reina, F., Hof, M., Eggeling, C. & Sezgin, E. Laurdan and Di-4-ANEPPDHQ probe different properties of the membrane. *J Phys D Appl Phys* **50**, (2017).

141. Dinic, J., Biverståhl, H., Mäler, L. & Parmryd, I. Laurdan and di-4-ANEPPDHQ do not respond to membrane-inserted peptides and are good probes for lipid packing. *Biochimica et Biophysica Acta (BBA) - Biomembranes* **1808**, 298–306 (2011).

142. Sanchez, S. A. *et al.* Laurdan Generalized Polarization: from cuvette to microscope.

143. Owen, D. M., Rentero, C., Magenau, A., Abu-Siniyeh, A. & Gaus, K. Quantitative imaging of membrane lipid order in cells and organisms. *Nat Protoc* **7**, 24–35 (2011).

144. Gunther, G., Malacrida, L., Jameson, D. M., Gratton, E. & Sánchez, S. A. LAURDAN since Weber: The Quest for Visualizing Membrane Heterogeneity. *Acc Chem Res* **54**, 976 (2021).

145. Ghoneim, N. Photophysics of Nile red in solution: Steady state spectroscopy. *Spectrochim Acta A Mol Biomol Spectrosc* **56**, 1003–1010 (2000).

146. Levitt, J. A., Chung, P.-H. & Suhling, K. Spectrally resolved fluorescence lifetime imaging of Nile red for measurements of intracellular polarity. *https://doi.org/10.1117/1.JBO.20.9.096002* **20**, 096002 (2015).

147. Anthis, N. J. & Clore, G. M. Sequence-specific determination of protein and peptide concentrations by absorbance at 205 nm. *Protein Sci* **22**, 851 (2013).

148. Greenfield, N. J. Using circular dichroism spectra to estimate protein secondary structure. *Nature Protocols 2007 1:6* **1**, 2876–2890 (2007).

149. Kelly, S. M. & Price, N. C. The application of circular dichroism to studies of protein folding and unfolding. *Biochim Biophys Acta* **1338**, 161–185 (1997).

150. Dodero, V. I., Quirolo, Z. B. & Sequeira, M. A. Biomolecular studies by circular dichroism. *Front Biosci (Landmark Ed)* **16**, 61–73 (2011).

151. Yandek, L. E. *et al.* Mechanism of the Cell-Penetrating Peptide Transportan 10 Permeation of Lipid Bilayers. *Biophys J* **92**, 2434 (2007).

152. Saar, K. *et al.* Cell-penetrating peptides: a comparative membrane toxicity study. *Anal Biochem* **345**, 55–65 (2005).

153. El-Andaloussi, S., Järver, P., Johansson, H. J. & Langel, Ü. Cargo-dependent cytotoxicity and delivery efficacy of cell-penetrating peptides: a comparative study. *Biochem J* **407**, 285 (2007).

154. Järver, P. & Langel, Ü. The use of cell-penetrating peptides as a tool for gene regulation. *Drug Discov Today* **9**, 395–402 (2004).

155. Lehto, T. *et al.* A Peptide-based Vector for Efficient Gene Transfer In Vitro and In Vivo. *Molecular Therapy* **19**, 1457 (2011).

156. Arukuusk, P. *et al.* New generation of efficient peptide-based vectors, NickFects, for the delivery of nucleic acids. *Biochimica et Biophysica Acta (BBA) - Biomembranes* **1828**, 1365–1373 (2013).

157. Moghal, M. M. R., Islam, M. Z., Hossain, F., Saha, S. K. & Yamazaki, M. Role of Membrane Potential on Entry of Cell-Penetrating Peptide Transportan 10 into Single Vesicles. *Biophys J* **118**, 57–69 (2019).

158. Kristensen, M., Birch, D. & Nielsen, H. M. Applications and challenges for use of cell-penetrating peptides as delivery vectors for peptide and protein cargos. *International Journal of Molecular Sciences* vol. 17 Preprint at https://doi.org/10.3390/ijms17020185 (2016).

159. Islam, M. Z., Ariyama, H., Alam, J. M. & Yamazaki, M. Entry of cell-penetrating peptide transportan 10 into a single vesicle by translocating across lipid membrane and its induced pores. *Biochemistry* **53**, 386–396 (2014).

160. Sani, M. A. & Separovic, F. How Membrane-Active Peptides Get into Lipid Membranes. *Acc Chem Res* **49**, 1130–1138 (2016).

161. Baxter, A. A., Lay, F. T., Poon, I. K. H., Kvansakul, M. & Hulett, M. D. Tumor cell membrane-targeting cationic antimicrobial peptides: novel insights into mechanisms of action and therapeutic prospects. *Cellular and Molecular Life Sciences 2017 74:20* **74**, 3809–3825 (2017).

162. Gagat, M., Zielińska, W. & Grzanka, A. Cell-penetrating peptides and their utility in genome function modifications (Review). *Int J Mol Med* **40**, 1615–1623 (2017).

163. Nekhotiaeva, N. *et al.* Cell entry and antimicrobial properties of eukaryotic cell-penetrating peptides. *The FASEB journal : official publication of the Federation of American Societies for Experimental Biology* **18**, 394–396 (2004).

164. Papo, N. & Shai, Y. New Lytic Peptides Based on the d,l-Amphipathic Helix Motif Preferentially Kill Tumor Cells Compared to Normal Cells†. *Biochemistry* **42**, 9346–9354 (2003).

165. Leuschner, C. & Hansel, W. Membrane Disrupting Lytic Peptides for Cancer Treatments. *Curr Pharm Des* **10**, 2299–2310 (2005).

166. Stulz, A. *et al.* Quantified Membrane Permeabilization Indicates the Lipid Selectivity of Membrane-Active Antimicrobials. *Langmuir* **35**, 16366–16376 (2019).

167. Izabela, R., Jarosław, R., Magdalena, A., Piotr, R. & Ivan, K. Transportan 10 improves the anticancer activity of cisplatin. *Naunyn Schmiedebergs Arch Pharmacol* **389**, 485–497 (2016).

168. Vale, N. *et al.* Cell-penetrating peptides in oncologic pharmacotherapy: A review. *Pharmacol Res* **162**, 105231 (2020).

169. Pooga, M., Elmquist, A. & Langel, Ü. Toxicity and side effects of cell-penetrating peptides. *Cell-Penetrating Peptides: Processes and Applications* 245–2621 (2002) doi:10.1201/9781420040777-14/TOXICITY-SIDE-EFFECTS-CELL-PENETRATING-PEPTIDES-MARGUS-POOGA-ANNA-ELMQUIST-.

170. Jana, B., Ghosh, S. & Chattopadhyay, N. Competitive binding of nile red between lipids and β-cyclodextrin. *J Photochem Photobiol B* **126**, 1–10 (2013).

171. Halder, A. *et al.* Lipid chain saturation and the cholesterol in the phospholipid membrane affect the spectroscopic properties of lipophilic dye nile red. *Spectrochim Acta A Mol Biomol Spectrosc* **191**, 104–110 (2018).

172. Bortner, C. D. & Cidlowski, J. A. Ions, the Movement of Water and the Apoptotic Volume Decrease. *Front Cell Dev Biol* **8**, 1415 (2020).

173. Parasassi, T., Krasnowska, E. K., Bagatolli, L. & Gratton, E. Laurdan and Prodan as Polarity-Sensitive Fluorescent Membrane Probes. *J Fluoresc* **8**, 365–373 (1998).

174. Fidorra, M., Duelund, L., Leidy, C., Simonsen, A. C. & Bagatolli, L. A. Absence of Fluid-Ordered/Fluid-Disordered Phase Coexistence in Ceramide/POPC Mixtures Containing Cholesterol. *Biophys J* **90**, 4437–4451 (2006).

175. Harris, F. M., Best, K. B. & Bell, J. D. Use of laurdan fluorescence intensity and polarization to distinguish between changes in membrane fluidity and phospholipid order. *Biochimica et Biophysica Acta (BBA) - Biomembranes* **1565**, 123–128 (2002).

176. Hincha, D. K. & Crowe, J. H. The lytic activity of the bee venom peptide melittin is strongly reduced by the presence of negatively charged phospholipids or chloroplast galactolipids in the membranes of phosphatidylcholine large unilamellar vesicles. *Biochim Biophys Acta* **1284**, 162–170 (1996).

177. Ruczyński, J. *et al.* Transportan 10 improves the pharmacokinetics and pharmacodynamics of vancomycin. *Scientific Reports 2019 9:1* **9**, 1–15 (2019).

178. Data Tables | Fluorescence Lifetime Standards | ISS. http://www.iss.com/resources/reference/data_tables/FL_LifetimeStandards.html.

179. Chen, R. F. & Knutson, J. R. Mechanism of fluorescence concentration quenching of carboxyfluorescein in liposomes: Energy transfer to nonfluorescent dimers. *Anal Biochem* **172**, 61–77 (1988).

180. Malacrida, L. & Gratton, E. LAURDAN fluorescence and phasor plots reveal the effects of a H2O2 bolus in NIH-3T3 fibroblast membranes dynamics and hydration. *Free Radic Biol Med* **128**, 144 (2018).

181. Malacrida, L., Jameson, D. M. & Gratton, E. A multidimensional phasor approach reveals LAURDAN photophysics in NIH-3T3 cell membranes. *Sci Rep* **7**, (2017).

182. Owen, D. M., Williamson, D. J., Magenau, A. & Gaus, K. ARTICLE Sub-resolution lipid domains exist in the plasma membrane and regulate protein diffusion and distribution. (2012) doi:10.1038/ncomms2273.

183. Eiríksdóttir, E., Konate, K., Langel, Ü., Divita, G. & Deshayes, S. Secondary structure of cell-penetrating peptides controls membrane interaction and insertion. *Biochimica et Biophysica Acta (BBA) - Biomembranes* **1798**, 1119–1128 (2010).

184. Greenfield, N. & Fasman, G. D. Computed Circular Dichroism Spectra for the Evaluation of Protein Conformation. *Biochemistry* **8**, 4108–4116 (1969).

185. Mishra, A., Gordon, V. D., Yang, L., Coridan, R. & Wong, G. C. L. HIV TAT forms pores in membranes by inducing saddle-splay curvature: Potential role of bidentate hydrogen bonding. *Angewandte Chemie - International Edition* **47**, 2986–2989 (2008).

186. Yang, T. sen *et al.* Quantifying membrane permeability of amphotericin B ion channels in single living cells. *Biochimica et Biophysica Acta (BBA) - Biomembranes* **1828**, 1794–1801 (2013).

187. Vetri, V. *et al.* Ethanol Controls the Self-Assembly and Mesoscopic Properties of Human Insulin Amyloid Spherulites. *Journal of Physical Chemistry B* **122**, 3101–3112 (2018).

188. Sato, H. & Feix, J. B. Peptide-membrane interactions and mechanisms of membrane destruction by amphipathic α-helical antimicrobial peptides. *Biochim Biophys Acta Biomembr* **1758**, 1245–1256 (2006).

189. Mukherjee, S., Raghuraman, H. & Chattopadhyay, A. Membrane localization and dynamics of Nile Red: Effect of cholesterol. *Biochimica et Biophysica Acta (BBA) - Biomembranes* **1768**, 59–66 (2007).

190. Skinkle, A. D., Levental, K. R. & Levental, I. Cell-Derived Plasma Membrane Vesicles Are Permeable to Hydrophilic Macromolecules. (2020) doi:10.1016/j.bpj.2019.12.040.

191. Fotin-Mleczek, M., Fischer, R. & Brock, R. Endocytosis and Cationic Cell-Penetrating Peptides - A Merger of Concepts and Methods. *Curr Pharm Des* **11**, 3613–3628 (2005).

192. Lundin, P. *et al.* Distinct uptake routes of cell-penetrating peptide conjugates. *Bioconjug Chem* **19**, 2535–2542 (2008).

193. Masuda, T. *et al.* An Artificial Amphiphilic Peptide Promotes Endocytic Uptake by Inducing Membrane Curvature. *Bioconjug Chem* **31**, 1611–1615 (2020).

194. Åmand, H. L., Boström, C. L., Lincoln, P., Nordén, B. & Esbjörner, E. K. Binding of cell-penetrating penetratin peptides to plasma membrane vesicles correlates directly with cellular uptake. *Biochimica et Biophysica Acta (BBA) - Biomembranes* **1808**, 1860–1867 (2011).

195. Ira & Krishnamoorthy, G. Probing the Link between Proton Transport and Water Content in Lipid Membranes. *Journal of Physical Chemistry B* **105**, 1484–1488 (2001).

196. Sengupta, P., Hammond, A., Holowka, D. & Baird, B. Structural determinants for partitioning of lipids and proteins between coexisting fluid phases in giant plasma membrane vesicles. *Biochimica et Biophysica Acta (BBA) - Biomembranes* **1778**, 20–32 (2008).

197. Johnson, S. A. *et al.* Temperature-dependent phase behavior and protein partitioning in giant plasma membrane vesicles. *Biochimica et Biophysica Acta (BBA) - Biomembranes* **1798**, 1427–1435 (2010).

198. Data Tables | Fluorescence Lifetime Standards | ISS. Preprint at http://www.iss.com/resources/reference/data_tables/FL_LifetimeStandards.html.

199. Carver, J. A. & Holt, C. Functional and dysfunctional folding, association and aggregation of caseins. *Adv Protein Chem Struct Biol* **118**, 163–216 (2019).

200. Bhat, M. Y., Dar, T. A. & Rajendrakumar Singh, L. Casein Proteins: Structural and Functional Aspects. *Milk Proteins - From Structure to Biological Properties and Health Aspects* (2016) doi:10.5772/64187.

201. Mcmahon, D. J. & Brown, R. J. Composition, Structure, and Integrity of Casein Micelles" A Review 1. *J Dairy Sci* **67**, 499–512.

202. Konrad, T., ¸b, G., Boratyn´ski, J., Boratyn´ski, B. & Boratyn´ski, J. B. Potential of Casein as a Carrier for Biologically Active Agents. *Topics in Current Chemistry 2017 375:4* **375**, 1–20 (2017).

203. Thorn, D. C. *et al.* Amyloid fibril formation by bovine milk κ-casein and its inhibition by the molecular chaperones α3- and β-casein. *Biochemistry* **44**, 17027–17036 (2005).

204. Thorn, D. C., Ecroyd, H., Sunde, M., Poon, S. & Carver, J. A. Amyloid fibril formation by bovine milk alpha s2-casein occurs under physiological conditions yet is prevented by its natural counterpart, alpha s1-casein. *Biochemistry* **47**, 3926–3936 (2008).

205. McCann, K. B. *et al.* Isolation and characterisation of a novel antibacterial peptide from bovine αS1-casein. *Int Dairy J* **16**, 316–323 (2006).

206. Recio, I. & Visser, S. Identification of two distinct antibacterial domains within the sequence of bovine alpha(s2)-casein. *Biochim Biophys Acta* **1428**, 314–326 (1999).

207. Farrel, H. M. , *et al.* Nomenclature of the Proteins of Cows' Milk-Sixth Revision | Elsevier Enhanced Reader. *J. Dairy Sci* https://reader.elsevier.com/reader/sd/pii/S0022030204733196?token=45F9FA55A5B81F3C7332721B575E97A9926E96176D8B370B8FCD207E73C8B3F6182470288CABBF6E06F3983BE2DDFCE1&originRegion=eu-west-1&originCreation=20220210121153 (2004).

208. Sinaga, H., Bansal, N. & Bhandari, B. Effects of milk pH alteration on casein micelle size and gelation properties of milk. *http://dx.doi.org/10.1080/10942912.2016.1152480* **20**, 179–197 (2016).

209. Chakraborty, A. & Basak, S. pH-induced structural transitions of caseins. *J Photochem Photobiol B* **87**, 191–199 (2007).

210. le Parc, A. *et al.* The Membrane-Associated Form of αs1-Casein Interacts with Cholesterol-Rich Detergent-Resistant Microdomains. *PLoS One* **9**, e115903 (2014).

211. Chanat, E., Martin, P. & Ollivier-Bousquet, M. Alpha(S1)-casein is required for the efficient transport of beta- and kappa-casein from the endoplasmic reticulum to the Golgi apparatus of mammary epithelial cells. *J Cell Sci* **112**, 3399–3412 (1999).

212. Wu, M. M. *et al.* Organelle pH studies using targeted avidin and fluorescein–biotin. *Chem Biol* **7**, 197–209 (2000).

213. le Parc, A., Leonil, J. & Chanat, E. αS1-casein, which is essential for efficient ER-to-Golgi casein transport, is also present in a tightly membrane-associated form. *BMC Cell Biol* **11**, 65 (2010).

214. McMahon, D. J. & Oommen, B. S. Casein Micelle Structure, Functions, and Interactions. *Advanced Dairy Chemistry: Volume 1A: Proteins: Basic Aspects, 4th Edition* 185–209 (2013) doi:10.1007/978-1-4614-4714-6_6.

215. Holt, C. & Carver, J. A. Quantitative multivalent binding model of the structure, size distribution and composition of the casein micelles of cow milk. *Int Dairy J* **126**, 105292 (2022).

216. Vaia, B., Smiddy, M. A., Kelly, A. L. & Huppertz, T. Solvent-Mediated Disruption of Bovine Casein Micelles at Alkaline pH. *J Agric Food Chem* **54**, 8288–8293 (2006).

217. Huppertz, T., Vaia, B. & Smiddy, M. A. Reformation of casein particles from alkaline-disrupted casein micelles. *J Dairy Res* **75**, 44–47 (2008).

218. Madadlou, A., Mousavi, M. E., Emam-Djomeh, Z., Sheehan, D. & Ehsani, M. Alkaline pH does not disrupt re-assembled casein micelles. *Food Chem* **116**, 929–932 (2009).

219. Rehan, F., Ahemad, N. & Gupta, M. Casein nanomicelle as an emerging biomaterial—A comprehensive review. *Colloids Surf B Biointerfaces* **179**, 280–292 (2019).

220. Gandhi, S. & Roy, I. Doxorubicin-loaded casein nanoparticles for drug delivery: Preparation, characterization and in vitro evaluation. *Int J Biol Macromol* **121**, 6–12 (2019).

221. Sahu, A., Kasoju, N. & Bora, U. Fluorescence Study of the Curcumin−Casein Micelle Complexation and Its Application as a Drug Nanocarrier to Cancer Cells. *Biomacromolecules* **9**, 2905–2912 (2008).

222. Semo, E., Kesselman, E., Danino, D. & Livney, Y. D. Casein micelle as a natural nano-capsular vehicle for nutraceuticals. *Food Hydrocolloids 21* 936–942 (2007) doi:10.1016/j.foodhyd.2006.09.006.

223. de Luca, G. *et al.* Probing ensemble polymorphism and single aggregate structural heterogeneity in insulin amyloid self-assembly. *J Colloid Interface Sci* **574**, 229–240 (2020).

224. Pelton, J. T. & McLean, L. R. Spectroscopic methods for analysis of protein secondary structure. *Anal Biochem* **277**, 167–176 (2000).

225. Lee, S., Chul Choi, M., al Adem, K., Lukman, S. & Kim, Y. Aggregation and cellular toxicity of pathogenic or non-pathogenic proteins. doi:10.1038/s41598-020-62062-3.

226. Klaips, C. L., Gropp, M. H. M., Hipp, M. S. & Hartl, F. U. Sis1 potentiates the stress response to protein aggregation and elevated temperature. doi:10.1038/s41467-020-20000-x.

227. Liu, D. Z., Weeks, M. G., Dunstan, D. E. & Martin, G. J. O. Temperature-dependent dynamics of bovine casein micelles in the range 10–40 °C. *Food Chem* **141**, 4081–4086 (2013).

228. Zhang, G., Babenko, V., Dzwolak, W. & Keiderling, T. A. Dimethyl Sulfoxide Induced Destabilization and Disassembly of Various Structural Variants of Insulin Fibrils Monitored by Vibrational Circular Dichroism. *Biochemistry* **54**, 7193–7202 (2015).

229. Hirota-Nakaoka, N., Hasegawa, K., Naiki, H. & Goto, Y. Dissolution of beta2-microglobulin amyloid fibrils by dimethylsulfoxide. *J Biochem* **134**, 159–164 (2003).

230. Vetri, V. *et al.* Ethanol Controls the Self-Assembly and Mesoscopic Properties of Human Insulin Amyloid Spherulites. *Journal of Physical Chemistry B* **122**, 3101–3112 (2018).

231. Jordens, S., Adamcik, J., Amar-Yuli, I. & Mezzenga, R. Disassembly and reassembly of amyloid fibrils in water-ethanol mixtures. *Biomacromolecules* **12**, 187–193 (2011).

232. Nespovitaya, N. *et al.* Dynamic Assembly and Disassembly of Functional β-Endorphin Amyloid Fibrils. *J Am Chem Soc* **138**, 846–856 (2016).

233. di Russo, N. v., Estrin, D. A., Martí, M. A. & Roitberg, A. E. pH-Dependent Conformational Changes in Proteins and Their Effect on Experimental pKas: The Case of Nitrophorin 4. *PLoS Comput Biol* **8**, 1002761 (2012).

234. Yang, A. S. & Honig, B. On the pH dependence of protein stability. *J Mol Biol* **231**, 459–474 (1993).

235. Sadiq, U., Gill, H. & Chandrapala, J. Casein Micelles as an Emerging Delivery System for Bioactive Food Components. *Foods 2021, Vol. 10, Page 1965* **10**, 1965 (2021).

236. Digman, M. A. *et al.* Fluctuation Correlation Spectroscopy with a Laser-Scanning Microscope: Exploiting the Hidden Time Structure. *Biophys J* **88**, L33 (2005).

237. Semisotnov, G. v. *et al.* Study of the 'molten globule' intermediate state in protein folding by a hydrophobic fluorescent probe. *Biopolymers* **31**, 119–128 (1991).

238. Paroutis, P., Touret, N. & Grinstein, S. The pH of the secretory pathway: measurement, determinants, and regulation. *Physiology (Bethesda)* **19**, 207–215 (2004).

239. Crespo-Villanueva, A. *et al.* Casein interaction with lipid membranes: Are the phase state or charge density of the phospholipids affecting protein adsorption? *Biochimica et Biophysica Acta (BBA) - Biomembranes* **1860**, 2588–2598 (2018).

240. Yan, Y. bin, Wang, Q., He, H. W. & Zhou, H. M. Protein Thermal Aggregation Involves Distinct Regions: Sequential Events in the Heat-Induced Unfolding and Aggregation of Hemoglobin. *Biophys J* **86**, 1682 (2004).

241. Beliciu, C. M. & Moraru, C. I. Effect of solvent and temperature on the size distribution of casein micelles measured by dynamic light scattering. *J Dairy Sci* **92**, 1829–1839 (2009).

242. Fennema Galparsoro, D. *et al.* Conformational Transitions upon Maturation Rule Surface and pH-Responsiveness of α-Lactalbumin Microparticulates. *ACS Appl Bio Mater* **4**, 1876–1887 (2021).

243. Nakashima, K., Anzai, T. & Fujimoto, Y. Fluorescence Studies on the Properties of a Pluronic F68 Micelle. *Langmuir* **10**, 658–661 (1994).

244. Nivaggioli, T., Tsao, B., Alexandridis, P. & Hatton, T. A. Microviscosity in Pluronic and Tetronic Poly(ethylene oxide)-PolyCpropylene oxide) Block Copolymer Micelles. *Langmuir* **11**, 119–126 (1995).

245. Dobson, C. M., Swoboda, B. E. P., Joniau, M. & Weissman, C. The structural basis of protein folding and its links with human disease. *Philos Trans R Soc Lond B Biol Sci* **356**, 133–145 (2001).

246. Stefani, M. Generic cell dysfunction in neurodegenerative disorders: Role of surfaces in early protein misfolding, aggregation, and aggregate cytotoxicity. *Neuroscientist* **13**, 519–531 (2007).

247. Sokolovski, M., Sheynis, T., Kolusheva, S. & Jelinek, R. Membrane interactions and lipid binding of casein oligomers and early aggregates. *Biochimica et Biophysica Acta (BBA) - Biomembranes* **1778**, 2341–2349 (2008).

248. Pae, J. *et al.* Translocation of cell-penetrating peptides across the plasma membrane is controlled by cholesterol and microenvironment created by membranous proteins. *Journal of Controlled Release* **192**, 103–113 (2014).

249. Säälik, P. *et al.* Penetration without cells: Membrane translocation of cell-penetrating peptides in the model giant plasma membrane vesicles. *Journal of Controlled Release* **153**, 117–125 (2011).

250. Kalluri, R. The biology and function of fibroblasts in cancer. *Nat Rev Cancer* **16**, 582–598 (2016).

251. Biffi, G. & Tuveson, D. A. Diversity and biology of cancerassociated fibroblasts. *Physiol Rev* **101**, 147–176 (2021).

252. Wei, K., Nguyen, H. N. & Brenner, M. B. Fibroblast pathology in inflammatory diseases. *J Clin Invest* **131**, (2021).

253. Zughaier, S. M., Svoboda, P., Pohl, J., Stephens, D. S. & Shafer, W. M. The human host defense peptide LL-37 interacts with Neisseria meningitidis capsular polysaccharides and inhibits inflammatory mediators release. *PLoS One* **5**, (2010).

254. Bowdish, D. M. E., Davidson, D. J., Scott, M. G. & Hancock, R. E. W. Immunomodulatory activities of small host defense peptides. *Antimicrob Agents Chemother* **49**, 1727–1732 (2005).

255. Eriksson, O. S. *et al.* Identification of Cell-penetrating peptides that are bactericidal to neisseria meningitidis and prevent inflammatory responses upon infection. *Antimicrob Agents Chemother* **57**, 3704–3712 (2013).

256. Snell, A. A. *et al.* Cell-derived vesicles for in vitro and in vivo targeted therapeutic delivery. *ACS Omega* **4**, 12657–12664 (2019).

257. van Dommelen, S. M. *et al.* Microvesicles and exosomes: Opportunities for cell-derived membrane vesicles in drug delivery. *Journal of Controlled Release* **161**, 635–644 (2012).

258. Lösche, W., Scholz, T., Temmler, U., Oberle, V. & Claus, R. A. Platelet-derived microvesicles transfer tissue factor to monocytes but not to neutrophils. *Platelets* **15**, 109–115 (2004).

259. Mittelbrunn, M. *et al.* Unidirectional transfer of microRNA-loaded exosomes from T cells to antigen-presenting cells. *Nat Commun* **2**, (2011).